

Transiting Planets near the Snow Line from *Kepler*. I. Catalog*

HAJIME KAWAHARA^{1,2} AND KENTO MASUDA^{3,†}

¹*Department of Earth and Planetary Science, The University of Tokyo, Tokyo 113-0033, Japan*

²*Research Center for the Early Universe, School of Science, The University of Tokyo, Tokyo 113-0033, Japan*

³*Department of Astrophysical Sciences, Princeton University, Princeton, NJ 08544, USA*

ABSTRACT

We present a comprehensive catalog of cool (period $P \gtrsim 2$ yr) transiting planet candidates in the four-year light curves from the prime *Kepler* mission. Most of the candidates show only one or two transits and have largely been missed in the original *Kepler* Object of Interest catalog. Our catalog is based on all known such candidates in the literature as well as new candidates from the search in this paper, and provides a resource to explore the planet population near the snow line of Sun-like stars. We homogeneously performed pixel-level vetting, stellar characterization with *Gaia* parallax and archival/Subaru spectroscopy, and light-curve modeling to derive planet parameters and to eliminate stellar binaries. The resulting clean sample consists of 67 planet candidates whose radii are typically constrained to 5%, in which 23 are newly reported. The number of Jupiter-sized candidates (29 with $r > 8 R_{\oplus}$) in the sample is consistent with the Doppler occurrence. The smaller candidates are more prevalent (23 with $4 < r/R_{\oplus} < 8$, 15 with $r/R_{\oplus} < 4$) and suggest that long-period Neptune-sized planets are at least as common as the Jupiter-sized ones, although our sample is yet to be corrected for detection completeness. If the sample is assumed to be complete, these numbers imply the occurrence rate of 0.39 ± 0.07 planets with $4 < r/R_{\oplus} < 14$ and $2 < P/\text{yr} < 20$ per FGK dwarf. The stars hosting candidates with $r > 4 R_{\oplus}$ have systematically higher [Fe/H] than the *Kepler* field stars, providing evidence that giant planet–metallicity correlation extends to $P > 2$ yr.

Keywords: planets and satellites: detection — planets and satellites: individual — techniques: photometric

1. INTRODUCTION

Planets near the snow line, the freezing point of water, are expected to provide critical information on the core accretion theory. The expected location of the snow line around a Sun-like star is about 3 au (or 5 yr) in the traditional planet formation theory (Hayashi 1981) and may vary by a factor of a few depending on the stellar type, mass accretion rate, dust opacity, and evolutionary stage of the disk (e.g. Oka et al. 2011; Martin & Livio 2012; Mulders et al. 2015). Those distant planets may also dynamically affect the architecture of their inner planetary systems (Huang et al. 2017; Lai & Pu 2017; Hansen 2017; Becker & Adams 2017; Mustill et al. 2017; Pu &

Lai 2018), which almost always exist when the outer planet is Jupiter-sized (Zhu & Wu 2018; Bryan et al. 2019). While the population of long-period ($>$ a few yr) planets has been probed with the Doppler method for Jupiter-mass ones around Sun-like stars (Cumming et al. 2008; Mayor et al. 2011) and with microlensing for planets mainly around late-type dwarfs (e.g. Gould et al. 2010; Cassan et al. 2012; Suzuki et al. 2016), the transit search has been less complete. The *Kepler* mission (Borucki et al. 2011) provided a detailed view of planets within 1 au of Sun-like stars, but those with periods longer than two years were originally missed.

Several recent works have demonstrated the potential of *Kepler* to probe the population of long-period giant planets by identifying single and double transiting events (STEs and DTEs) in the four-year data. These events were out of the scope of the original *Kepler* pipeline that required three transits, and so dedicated searches have been performed via visual inspection (Wang et al. 2015; Uehara et al. 2016) and automated

Corresponding author: Hajime Kawahara
kawahara@eps.s.u-tokyo.ac.jp

* Based in part on data collected at Subaru Telescope, which is operated by the National Astronomical Observatory of Japan.

† NASA Sagan Fellow

pipelines (Osborn et al. 2016; Foreman-Mackey et al. 2016; Schmitt et al. 2017; Giles et al. 2018), both in the *Kepler* and *K2* (Howell et al. 2014) data sets. These searches have revealed long-period transiting planets more than anticipated before the launch (Yee & Gaudi 2008), some of which have been successfully followed-up (Dalba & Muirhead 2016; Dalba & Tamburo 2019), and even provided a quantitative occurrence rate of such planets around Sun-like stars (Foreman-Mackey et al. 2016). It is particularly noteworthy that the sensitivity of the *Kepler* data goes down to Neptune-sized planets around Sun-like stars in this period range, which are currently out of the scope of the Doppler (in terms of mass) and microlensing (in terms of host stars) methods.

In this work, we present a comprehensive catalog of long-period transiting planets from the prime *Kepler* mission, the *Kepler* long-period planet (KeLP) catalog, as a resource complementary to the *Kepler* object of interest (KOI) catalog (Twicken et al. 2016). This paper improves upon the previous works in the following three aspects. In terms of targets, we compile all the known events and add new targets from our additional search (Section 2); we independently vet all of them based on the centroid analysis and visual inspection of the pixel data, matching epochs, and detector positions of the events, and remove obvious false positives (Section 3). For stars, we perform precise characterization combining *Gaia* astrometry, archival spectroscopy, and our follow-up spectroscopy using the Subaru 8.2 m telescope (Section 4). For planets, we perform homogeneous light-curve modeling to derive precise planet parameters and to remove stellar binaries as possible on the basis of the inferred parameters (Section 5).

The properties of the promising candidates are discussed in Section 6. Their properties are used to evaluate the detectability of long-period planets as in this catalog with future direct imaging instruments in Section 7.

2. INPUT CATALOG

We first created an input catalog of long-period planet candidates by compiling known events from the literature (Section 2.1) and by performing a new dedicated search (Sections 2.2 and 2.3). Table 1 summarizes the sources of the input catalog, as well as the outputs after vetting processes in Sections 3–5. The “clean sample” column corresponds to the final product in the KeLP catalog.

2.1. Previously Reported Candidates

We collected long-period planet candidates from the following literature.¹

- Those from visual inspection by citizen scientists, namely *the Planet Hunters*, are described in Schmitt et al. (2014) and Wang et al. (2015). We included one DTE from the former, and 27 STEs and DTEs from the latter in the input catalog. We decided to include three triple transit events (TTEs) in Wang et al. (2015) as well, because two (KIC 10024862 and KIC 9413313) are not in the KOI catalog and one (KIC 8012732, KOI-8151) is classified as a false positive presumably due to transit timing variation of the second event.
- Uehara et al. (2016) also performed a visual search for STEs/DTEs around KOI stars. We included 19 targets from this work.
- Schmitt et al. (2017) found a DTE in KIC 5351520, which was overlooked by Uehara et al. (2016) due to the “Swiss-cheesing” effect of the light curve caused by inner transiting planets. This target was added.
- Foreman-Mackey et al. (2016) performed an automated search focusing on $\sim 40,000$ bright and quiet Sun-like stars. Seven new STEs/DTEs from this search were added.
- We realized that some targets detected in Section 2.2 have already been reported by Kipping et al. (2016) and in the *Kepler* Eclipsing Binary (KEB) catalog by Kirk et al. (2016). We classify them as inputs from the literature, rather than new candidates from our search.

2.2. Sigma Clipping and Visual Inspection

As the first simple search for deep transit events, we performed a search based on sigma-clipping and subsequent visual inspection. We identified dips as $> 2\sigma$ flux deviation lasting longer than 2.5h, where σ is the standard deviation of the light curve detrended with the second-order spline interpolation. Each candidate was visually inspected and the obvious stellar eclipses were removed; they are listed in Table 4. We applied this procedure to all the long-cadence (29.4 min), pre-search

¹ During the preparation of this manuscript, Herman et al. (2019) was posted on arXiv, who reported 12 long-period planet candidates using the code of Foreman-Mackey et al. (2016), refined stellar radii from *Gaia* DR2, and their own light-curve detrending. The two new events reported in their paper (KIC 6186417 and 7906827) were also detected in our analysis in Section 2.2, and so do not affect the present paper.

Table 1. Breakdown of the sources in the the KeLP catalog. S/D/T stand for single/double/triple transit events.

method	input	after FP test in Section 3 (S/D/T)	clean sample (S/D/T)	reference
Planet Hunter	1	1 (0/1/0)	1 (0/1/0)	Schmitt et al. (2014)
Planet Hunter	30	27 (13/11/3)	24 (11/10/3)	Wang et al. (2015)
-	1	1 (0/1/0)	1 (0/1/0)	Kipping et al. (2016)
<i>Kepler</i> eclipsing binary	3	2 (1/1/0)	0	Kirk et al. (2016)
VI of KOI (Jun 4, 2015)	19	15 (14/1/0)	13 (12/1/0)	Uehara et al. (2016)
automated search	7	5 (4/1/0)	2 (1/1/0)	Foreman-Mackey et al. (2016)
Swiss cheese effect	1	1 (0/1/0)	1 (0/1/0)	Schmitt et al. (2017)
clipping+VI	43	28 (24/4/0)	16 (13/3/0)	this paper
trapezoid least square+VI	16	13 (10/3/0)	9 (7/2/0)	this paper
total	121	93 (66/24/3)	67 (44/19/3)	

data conditioning (PDC) light curves. As a result, we found 43 new STEs and DTEs, which are listed as “clipping+VI” in Table 1. We found no new TTE by this method. The sample of 102 STEs and DTEs both from this search and the previous literature (Section 2.1) was used to calibrate a systematic search by the trapezoid fitting in Section 2.3.

2.3. Trapezoid Least Square

We then performed a systematic search by matching a trapezoid template to the long-cadence PDC light curves (trapezoid least square; TLS). As shown in Figure 1, the fitting parameters are the central time t_0 , height H , gradient H/L , and total width W . For each $t = t_0$, we

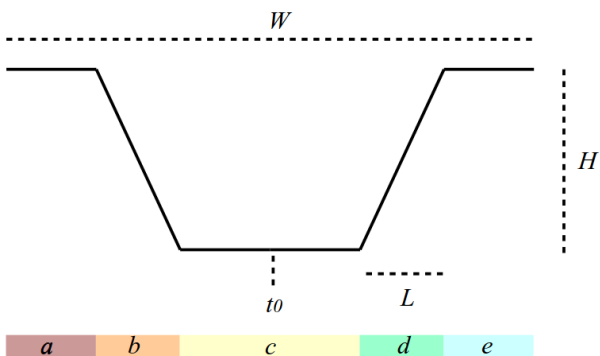


Figure 1. Parameters of the trapezoid model. The central time, width, and height of the template are given by t_0 , W , and H , respectively. L is the length of b and d , and c is twice as long as a and e ; so $c/2 = a = e = W/2 - L$.

minimize the χ^2 defined by

$$\chi^2 = \sum_{t_i \in a, e} \frac{(x_i + H/2)^2}{\sigma_i^2} + \sum_{t_i \in b} \frac{[x_i - HL^{-1}(t_i + W/4)]^2}{\sigma_i^2} + \sum_{t_i \in c} \frac{(x_i - H/2)^2}{\sigma_i^2} + \sum_{t_i \in d} \frac{[x_i + HL^{-1}(t_i - W/4)]^2}{\sigma_i^2}, \quad (1)$$

where a to e are the regions shown in Figure 1 and $x_i = x(t_i)$ is the light curve normalized to zero within the fitting region. Because minimization of equation (1) is time consuming, we implement the process using the graphics processing unit (GPU) and pycuda (Klöckner et al. 2012), as described in Appendix A. Before the trapezoid fitting, we detrended the light curve using a median filter with a timescale of 64 h. Because the median filter with a larger window size is also time consuming, we also implemented a GPU-based median filter, the kernel_MedianV_sh algorithm proposed by Couturier (2013). We executed the code using GeForce Titan X and GTX 1080Ti. The resulting computing time for a full long cadence time series is less than a second. To increase the precision of the best-fit parameters, we refit the trapezoid model with higher precision using CPU.

Figure 2 shows an example of an STE in KIC 8313257 detected by the TLS algorithm. We compute the signal to noise ratio for each t_0 by

$$s(t_0) \equiv \frac{\tilde{H}}{\sqrt{\text{res} \cdot (n - 3)}}, \quad (2)$$

where \tilde{H} is the maximum value of H among the grids of L and W for a given t_0 , res is the squared norm of the residual of the trapezoid fit, n is the number of data points in the fitting region, and $n - 3$ is the degrees of freedom of the fit. We call $s(t_0)$ the TLS series (the top panel in Figure 2). We pick up the dip at $t_0 = \hat{t}_0$ that maximizes $s(t_0)$ as an STE candidate, and the value of $s(\hat{t}_0)$ is defined as the S/N of the candidate dip.

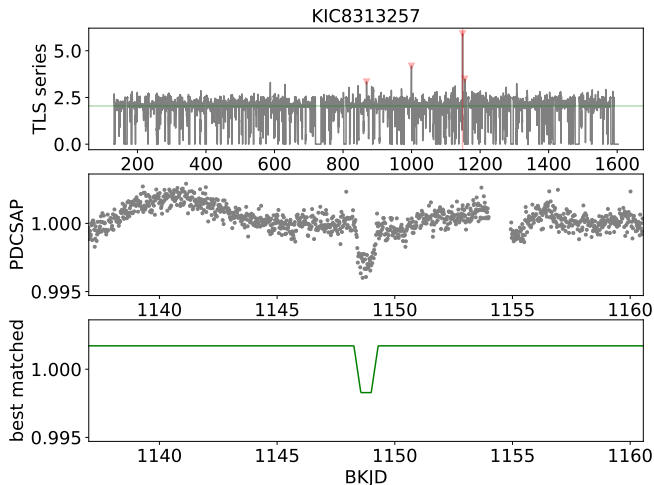


Figure 2. One of the STE detected by the trapezoid least square (TLS) algorithm (Section 2.3). The top panel shows the TLS time series for the four-year data defined by Equation (2). The strongest peak is located at the Barycentric *Kepler* Julian Day (BKJD) ~ 1149 . The PDC flux and the best-match trapezoid of the corresponding STE candidate are shown in the middle and bottom panels, respectively.

The fitting procedure described above always yields one dip candidate in each light curve. However, many of the dip candidates, even with high S/N values, are false positives. Most of the false dips turned out to be due to stellar variability producing many peaks and valleys in the light curve. The trapezoid fitting detects one of those valleys, and the resulting TLS series exhibits a series of false peaks with comparable S/N to $s(\tilde{t}_0)$. Similarly, short-period transiting planets exhibit multiple high peaks in the TLS series. In contrast, typical STEs/DTEs exhibit only one or two high peaks in the TLS series, as shown in the top panel in Figure 2.

To characterize the difference between these two cases, we introduce another empirical metric to describe the significance of the fourth peak in the TLS series:

$$\Delta \equiv \frac{s(t_{0,4}) - \overline{s(t_0)}}{\sigma_s}, \quad (3)$$

where $t_{0,4}$ is the time at the fourth highest peak in the TLS series, and $\overline{s(t_0)}$ and σ_s are the median and standard deviation of the TLS series, respectively. The false positive cases with multiple high peaks are expected to have higher Δ compared to true STEs/DTEs with a small number of high peaks. The choice of the fourth peak is motivated by the fact that the second or third highest peaks occasionally become high due to a gap in the light curve, rather than stellar variability or short-period transiting planets; the choice of the fourth peak thus helps to suppress the rate of true negatives caused by the gap.

Figure 3 shows Δ and $(S/N)/\sqrt{\Delta}$ of all the events detected by the TLS algorithm (orange dots). The choice of the x -axis is motivated by the empirically-found scaling $S/N \propto \sqrt{\Delta}$ for small S/N; this normalization aligns the orange dots vertically and makes the following classification simpler. We also ran the TLS algorithm for the systems known to have STEs/DTEs in Sections 2.1 and 2.2, and recovered 61 of them; their positions are marked by red stars in Figure 3. As expected, these events are clustered in the region with high S/N and low Δ . Based on these training set results, we chose the region defined by $\Delta < 7$ and $S/N > 2.5\sqrt{\Delta}$ (green square region in Figure 3) and one of us (KH) visually inspected all 20816 events in this region. From this search, we identified 10 STEs and 3 DTEs that have not been reported in the literature. We added these 13 systems into our input catalog. We also found three TTEs; one of them, KIC 6681473 (KOI-5312) was a KOI false positive and included in the input list for further vetting. The other two were not included, because they were either a KOI candidate (KIC 3634051, KOI-6103) or already in the input catalog (KIC 8012732). We also found four obvious stellar primary and secondary (flat-bottomed) eclipses. These events are listed in Table 4.

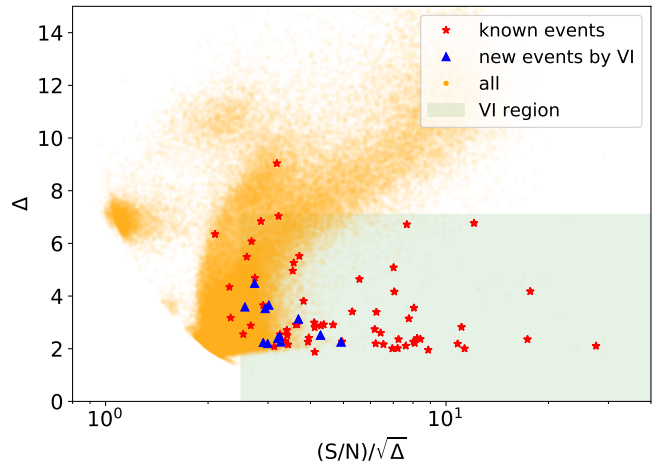


Figure 3. Classification of the STE candidates from the TLS algorithm on the $(S/N)/\sqrt{\Delta}$ - Δ plane. Orange dots are all the candidates. The known events from the literature (Section 2.1) and our search in Section 2.2 are shown with red stars; they were used as the training set to determine the region for visual inspection ($\Delta < 7$ and $S/N > 2.5\sqrt{\Delta}$; green square). From the visual inspection of the orange candidates in this region, we found additional 13 candidates that passed the vetting in Section 3, shown by blue triangles.

3. ELIMINATING SUSPICIOUS SIGNALS

3.1. First Screening of the Targets

From the STEs/DTEs in Wang et al. (2015), we excluded the following two targets. For KIC 5522786, candidate transits are reported at BKJD = 283 and 1040 in the PDC light curve (Schmitt et al. 2014; Wang et al. 2015), but the latter is not seen in the simple aperture photometry (SAP) light curve. Moreover, there are other suspicious dips at BKJD = 268.5 and 872.5 in the SAP light curve. Thus the reliability of the reported signal appears to be low. KIC 8540376 exhibits DTEs, but the separation is 31.8 days because only two quarters are available. The period is too short for our purpose. Similarly, we removed the STE in KIC 8489948 (the sigma clipping+VI in Section 2.2) from the list, because only two quarters (Q16 and 17) are available. These three objects are listed as “SC” in Table 4 in Appendix B.

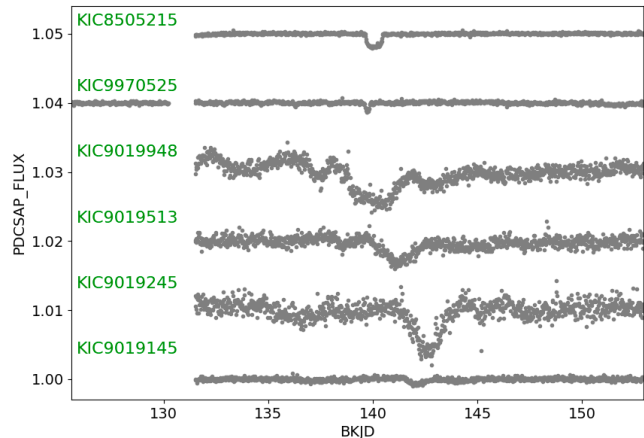


Figure 4. Suspicious dips around BKJD = 140 identified from the similar transit times. The bottom four events with similar non-transit-like shapes were excluded, and KIC 8505215 and KIC 9970525 were kept in the candidate list.

In addition to KIC 8505215 and KIC 9970525, several other STEs were found to be separated by less than a day. To check if this is a statistically natural outcome, we compared the distribution of the time intervals of the nearest STEs/DTEs against that of a completely random realization of the transit events (Figure 5). The resulting distributions are consistent with each other, with the Kolmogorov-Smirnov (KS) p -value of 0.98.

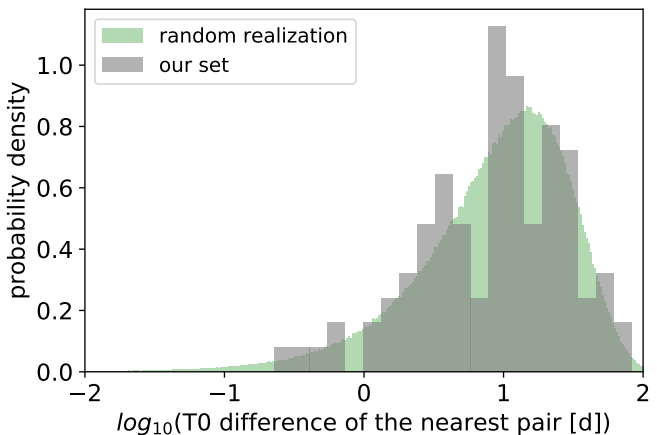


Figure 5. The distribution of the time intervals between the two nearest STE pairs. The gray histogram is the distribution from the input catalog, and the green histogram is a simulated probability density function for a random realization.

3.2. Events Sharing Similar Epochs

Matching ephemerides in two different targets is known to be a strong indicator of false positives². Although the period is not precisely constrained for most of our sample by construction, signals originating from contamination may still share similar transit times, which may be used to flag spurious signals. We therefore checked the events with similar central times among all the input candidates. We found that STEs in KIC 8505215, 9970525, 9019948, 9019513, 9019245, and 9019145 occurred within a few days (Figure 4), and some of them do have spurious shapes. We excluded the latter four (listed as “SE” in Table 4), but decided to keep the events in KIC 8505215 and KIC 9970525 (top two rows) in the list because they have distinct transit-like shapes unlike the removed four.

² As an example for long-period signals, the transit times of the triple dips with an interval of ~ 375 d in KIC 8622875 (KOI-5551) matches those of pulse-like signals in KIC 8557406 and KIC 8622134, therefore, those are considered as false positives (Kawahara et al. 2018).

3.3. Visual Inspection of the Pixel Data

Here and in Section 3.4, we describe the pixel-level vetting of the signals. We first visually checked the pixel-level light curves around the detected events. We

excluded the events that exhibit either one of the following two features:

- The signal originates from a single pixel. This is likely due to a sudden drop in the pixel sensitivity and produces a box-shaped false positive. The “transit depth” in the single pixel is deeper than that seen in the SAP flux, because the contribution comes from that one pixel. For example, dips in KIC 7190443 at BKJD = 1201 and KIC 5621767 at BKJD = 839 belong to this category.
- The signal is apparently from outside the aperture. In this case, the signal depths significantly vary over the pixels in the aperture because the amount of contamination depends on the distance from the nearby source. One obvious such case is KIC 5480825 at BKJD = 363.

The automated centroid analysis in Section 3.4 will anyway remove the latter class of false positives, but visual inspection is important for the former class that does not necessarily produce centroid shifts. The false positives identified here are listed in Table 4 as “VIP” (visual inspection of pixel data).

3.4. Pixel-level Difference Imaging

The centroid shift of the pixel-level difference image between in- and out-of-transit data is an excellent indicator of the contamination from a nearby star (Bryson et al. 2013). We define the difference image by

$$\delta I(X, Y) \equiv \langle I(X, Y, t) \rangle_{\text{out}} - \langle I(X, Y, t) \rangle_{\text{in}}, \quad (4)$$

where X and Y are the column and row positions of the pixel on image, $I(X, Y, t)$ is the flux in the pixel (X, Y) at time t , and $\langle I(X, Y, t) \rangle_{\text{in}}$ and $\langle I(X, Y, t) \rangle_{\text{out}}$ are the time-medians of the flux inside (i.e. between ingress and egress) and outside (i.e. both sides of) the dip.

Figure 6 shows a clear example of contamination from a nearby star in KIC 1717722. The top panel shows the in- and out-of-transit data. The lower left panel shows the mean pixel image of the quarter that includes the detected dip. Pixels labeled with “-” are outside the aperture used for SAP and PDC light curves. The difference image computed by Equation (4) is shown in the bottom right panel, along with the position of KIC 1717722 (red star symbol) and nearby stars (orange star symbols) taken from the KIC stellar list provided by the *Kepler* team. During the dip, the center of the flux moves toward nearby stars in the upper left of the target star, suggesting that the dip originates from one of those nearby stars, and not on KIC 1717722. Two other targets were found to exhibit such a significant centroid shift greater than a pixel.

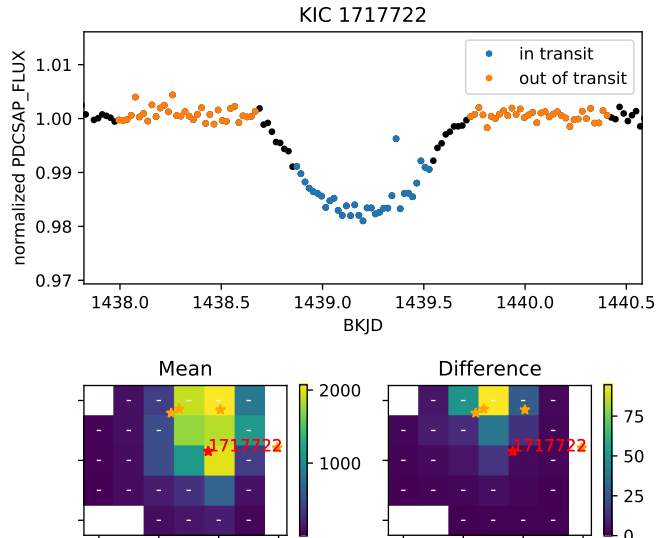


Figure 6. An example of a contaminated signal detected by the pixel-level difference imaging. The top panel shows the dip of KIC 1717722 and the in-transit (blue) and out-of-transit (orange) ranges we adopted. The bottom panels represent the mean image for the quarter in which the dip exists (left), and the difference image defined by Equation (4) (right). The minus symbol (-) indicates the pixels outside the aperture used in the SAP/PDC light curves. The unit for pixel images is e^-/s .

To systematically identify such shifts including the smaller ones, we evaluated the centroid shift of the difference image:

$$\delta \mathbf{X} = \mathbf{X}_{\text{PRF}}[\delta I(X, Y)] - \mathbf{X}_{\text{PRF}}[\langle I(X, Y, t) \rangle_{\text{out}}], \quad (5)$$

where $\mathbf{X}_{\text{PRF}}[I(X, Y)]$ is the center of the best-fit pixel-response function (PRF) image to $I(X, Y)$. The PRF fitting in this paper was performed using the `lightkurve` package (Vincius et al. 2018). The PRF fitting did not work well and returned unstable centroid positions when the total electron number of the difference image is below 30. We decided to just keep 19 such low-S/N targets in our list.

Bryson et al. (2013) proposed to use the mean and variance of the centroid shifts from all repeating transits to quantify the significance of the shift. In our case, however, there are only one or two dips in the light curve and this method is not applicable. Instead, we follow a method similar to the one proposed by Kawahara et al. (2018), who checked the centroid shift in double or triple pulses due to gravitational microlensing by a white-dwarf (WD) companion. First, we injected 1,000 simulated dips with the same depth as the detected one, at randomly selected times in the light curves from the same season. The images within each injected dip were

given by

$$I^*(X, Y, t) = I(X, Y, t) - \alpha I_{\text{sim}}(X, Y), \quad (6)$$

where $I_{\text{sim}}(X, Y)$ is the best-fit PRF model for the median of $I(X, Y, t)$ in this range, and the scaling factor α is chosen so that the injected dip has the same depth as the original one. Second, the difference image of the injected signal,

$$\delta I^*(X, Y) \equiv \langle I(X, Y, t) \rangle_{\text{out}} - \langle I^*(X, Y, t) \rangle_{\text{in}}, \quad (7)$$

was used to compute its centroid shift $\delta \mathbf{X}^*$ in the same way as for the detected signal:

$$\delta \mathbf{X}^* = \mathbf{X}_{\text{PRF}}[\delta I^*(X, Y)] - \mathbf{X}_{\text{PRF}}[\langle I(X, Y, t) \rangle_{\text{out}}]. \quad (8)$$

Finally, the distribution of $\delta \mathbf{X}^*$ was used to estimate statistical uncertainty of the centroid shift determination. We computed ellipses that include 95.5%/99.7% of $\delta \mathbf{X}^*$ (dashed/dotted lines in Figure 7), which we conventionally call $2\sigma/3\sigma$ ellipses.³ We flagged 10 events outside the 3σ ellipse and discuss them further below. We decided to keep six events between 2σ and 3σ ellipses, considering that the number ($6/93 \sim 6\%$) is consistent with what we expect from statistical fluctuation.

³ The ellipses were computed as follows. We performed the principle component analysis (PCA) whitening of the dataset of $\delta \mathbf{X}^*$ and determine the center and the radius that surround 95.5% of the distribution. The radius that encircles 99.7% was estimated by multiplying the 95.5% radius by 1.38, assuming the two-dimensional normal distribution. Then we performed the inverse PCA transform whitening of those radii.

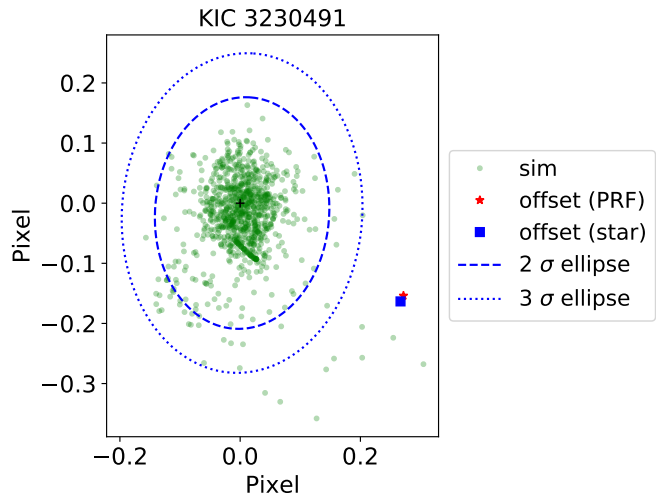


Figure 7. An example of a false positive showing a significant centroid shift (KIC 3230491). The red star is the shift of the difference image centroid from the out-of-transit one, $\delta \mathbf{X}$ (Equation 5). The green dots show the distribution of the centroid shifts computed for injected dipoles $\delta \mathbf{X}^*$ (Equation 8). The dashed and dotted lines are the 95.5% and 99.7% ellipses computed from the green dots. The blue square is the shift of the difference image centroid from the catalog position of the target (Equation 9). Both the red star and blue square show significant shifts, and so this case is a false positive.

We further examined the 10 flagged events, because a true signal can still cause a large centroid shift as defined by Equation (5) due to a nearby unrelated star (Bryson et al. 2013). In this case, the out-of-transit centroid is shifted toward the nearby star, while the in-transit one remains close to the original target star. To avoid erroneous identification of this case as a false positive, Bryson et al. (2013) proposed another centroid test using the difference image and the catalog position of a star \mathbf{X}_{cat} :

$$\delta \mathbf{X}_{\text{cat}} = \mathbf{X}_{\text{PRF}}[\delta I(X, Y)] - \mathbf{X}_{\text{cat}}. \quad (9)$$

Again, Bryson et al. (2013) estimated the significance of the shift from quarter-to-quarter variations but this is not possible in our case, and so we adopted the same 3σ ellipse constructed from injected signals. Among the 10 flagged events, $\delta \mathbf{X}_{\text{cat}}$ for the event in KIC 11709124 was found to be within 3σ , and so this target was moved back to the list. In addition to the nearby star, a true signal can exhibit a larger centroid shift when the signal is located near the gap and the out-of-transit data are partially unavailable (Kawahara et al. 2018). This was the case for KIC 6191521, both of whose DTEs are located near data gaps. One shows the centroid shift beyond the 3σ ellipse, the other is between the 2σ and 3σ ones, and their values are all near the outliers of the

shifts from simulated dips. These imply that the large offset is due to the data gaps, and we decided to keep KIC 6191521 in our list as well.

Figure 8 summarizes the pixel-data examination described in this subsection. Here eight targets were classified as false positives and eliminated from the list (“CS” in Table 4).

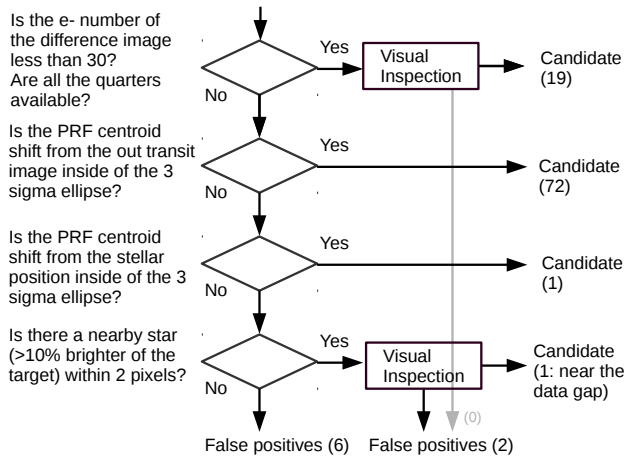


Figure 8. Flow chart of the centroid test using the pixel-level difference image.

3.5. Detector Positions of the Transit Events

Mullally et al. (2015) pointed out two types of instrumental effects causing false positives. One is the edge effect around a data gap; we already excluded suspicious dips around the gaps during the visual inspection in Sections 2.2 and 2.3. The other is an artifact with the period close to the orbital period of the *Kepler* spacecraft (372 days), which may contaminate long-period candidates discussed here. As shown in Figure 9, such artifacts are clustered around the orbital period of *Kepler* and have durations typically longer than 0.3 days.

To identify the nature of the artifact, we checked the CCD positions of the KOI false positives with a period between 350–390 d and a duration longer than 0.3 d, which we define as an “FP bump,” taking into account the rotation of the spacecraft every three months. As shown in the left panel of Figure 10, the transits in the FP bump are clustered around the CCD chip 58 and the left edge of the chip 62. This clustering strongly indicates the instrumental origin; the FP bump appears to be produced by repeating signals from the same CCD chips. On the other hand, we did not find any such clustering for long-period planet candidates in our list (right panel of Figure 10). Thus we find no evidence

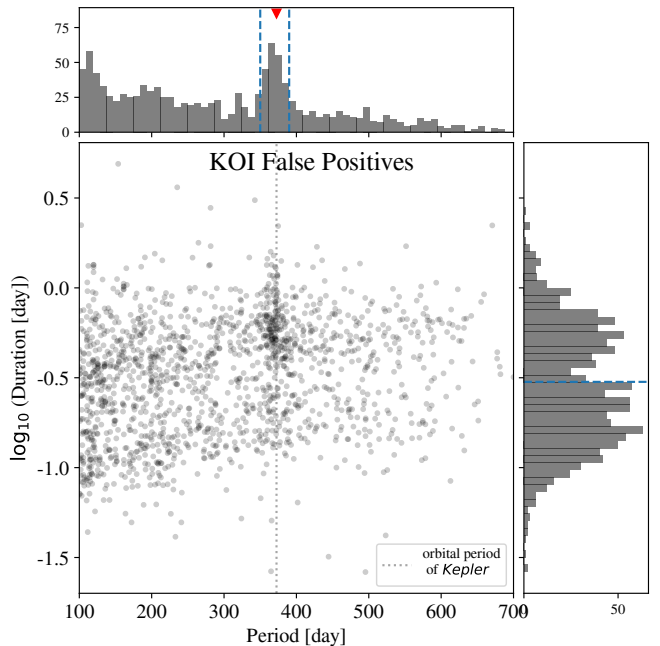


Figure 9. KOI false positives on the orbital period–transit duration plane. The dashed line and red triangle indicate the orbital period of *Kepler* (372 d). The top and left panels are the histograms of the period and duration. The clustering around $P = 372$ d and duration of 0.6 d is due to instrumental artifacts. We call the region with periods 350–390 d (blue dashed lines in the histograms) and duration longer than 0.3 d as an “FP bump.”

that a majority of these events originate from similar artifacts as producing the FP bump.

4. THE STARS

Precise stellar parameters, especially radii, are important for characterization and vetting of the detected planet candidates. Here we characterize the host stars in the input catalog by fitting stellar evolutionary models to spectroscopic atmospheric parameters or broad-band photometry, and parallax from *Gaia* DR2. The stars analyzed here include not only those hosting candidates that passed the FP test in Section 3, but also some that failed.

4.1. Spectroscopy

First, we collected archival spectroscopic parameters from the California *Kepler* Survey (CKS, Petigura et al. 2017), the Spectral Properties of Cool Stars (SPOCS) catalog by Brewer et al. (2016), the Large Sky Area Multi-Object Fiber Spectroscopic Telescope (LAMOST; Cui et al. 2012; Luo et al. 2015)/LASP stellar parameters (Wu et al. 2014) from DR4, *The Payne* (Ting et al. 2018) parameters based on APOGEE DR14 (Majewski et al. 2017), and the *Kepler* input catalog DR25 (Mathur

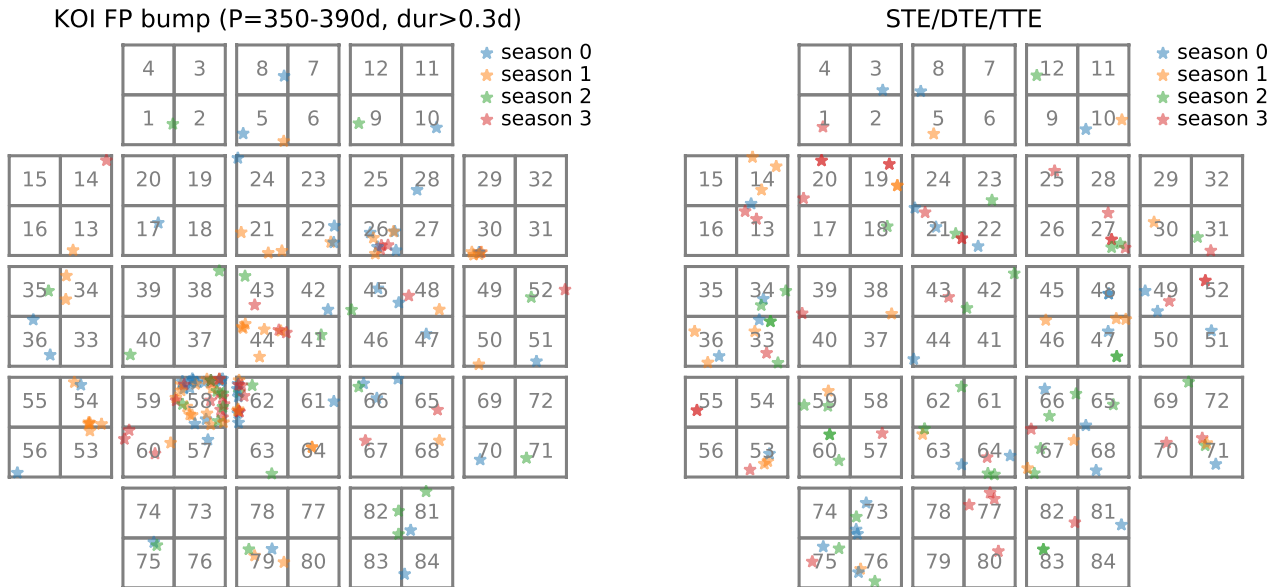


Figure 10. The CCD positions of the events (chips 1–84). The left panel shows the distribution for those in the KOI FP bump, defined by $P = 350\text{--}390$ d and duration longer than 0.3 d (Figure 9). The color indicates the season in which the events are observed: blue, yellow, green, and red stars correspond to seasons 0, 1, 2, and 3, respectively. Only the first transit event for each target is plotted, because the other transits occur mostly in the same season by construction of the FP bump (i.e. period close to one year). The right panel shows the same distribution for all the long-period planet candidates in our list.

et al. 2017) with spectroscopic provenance (KIC 6191521 alone, originally from Furlan et al. 2017). For these stars, we adopted the literature values of effective temperature T_{eff} , surface gravity $\log g$, and iron abundance $[\text{Fe}/\text{H}]$ with preferences given in this order. Note that 14 of the stars analyzed here are in the CKS sample and have known inner transiting planets and planet candidates (see also Tables 3 and 5, and Section 6.5).

For stars without available archival spectra, we obtained high-resolution spectra using the high dispersion spectrograph (HDS; Noguchi et al. 2002) installed on the Subaru 8.2 m telescope. We mainly observed targets brighter than $r\text{-mag} = 15$ and without V-shaped dips. The observations were performed on UT July 28, August 5, and September 6 in 2018 (proposal IDs S18A-044 and S18B-062, PI: Kawahara) with the standard I2a setup and 2×1 binning without an image rotator. Image slicer #2 (Tajitsu et al. 2012) was used for targets with $r\text{-mag} \lesssim 14.5$ to increase the signal-to-noise ratio. The resulting spectral resolution was typically 60,000–87,000. We then fit the spectra around the Mg triplet using the `Specmatch-Emp` code (Yee et al. 2017) to derive T_{eff} , $\log g$, and $[\text{Fe}/\text{H}]$ via empirical matching to the spectra of the touchstone stars with well-determined parameters. Figure 11 shows the observed spectra (black) along with the best matches from the code (green) for FGK stars. We cross-checked our estimates for KIC 8505215 ($T_{\text{eff}} = 4954 \pm 110$ K,

$\log g = 4.54 \pm 0.12$, $[\text{Fe}/\text{H}] = -0.45 \pm 0.09$) against the CKS values ($T_{\text{eff}} = 4935 \pm 116$ K, $\log g = 4.42 \pm 0.10$, $[\text{Fe}/\text{H}] = -0.28 \pm 0.07$, including systematic uncertainties), and found a reasonable agreement.

The atmospheric parameters directly derived from spectroscopy are summarized in the last three columns of Table 2 with the source in the fourth column from the last. These parameters are collected from multiple sources including the present paper, and their accuracy and precision are not uniform. For the following isochrone modeling, we adopt the same uncertainties of 110 K for T_{eff} , 0.12 for $\log g$, and 0.1 for $[\text{Fe}/\text{H}]$ for all stars, considering the typical accuracy of these parameters (cf. Petigura et al. 2017). In practice, the stellar radius is mainly determined by T_{eff} and *Gaia* parallax, and the other parameters play minor roles.

4.2. Photometry

We also collected *JHK* photometry from the Two Micron All Sky Survey (2MASS; Skrutskie et al. 2006) for all the stars in the sample. For those without spectroscopic observations, the colors are used to estimate T_{eff} ; otherwise only the *K*-band magnitude was used so that the extinction does not introduce systematic bias on T_{eff} . We decided not to use *griz* colors considering the systematic trend reported in Pinsonneault et al. (2012).

4.3. Isochrone Modeling

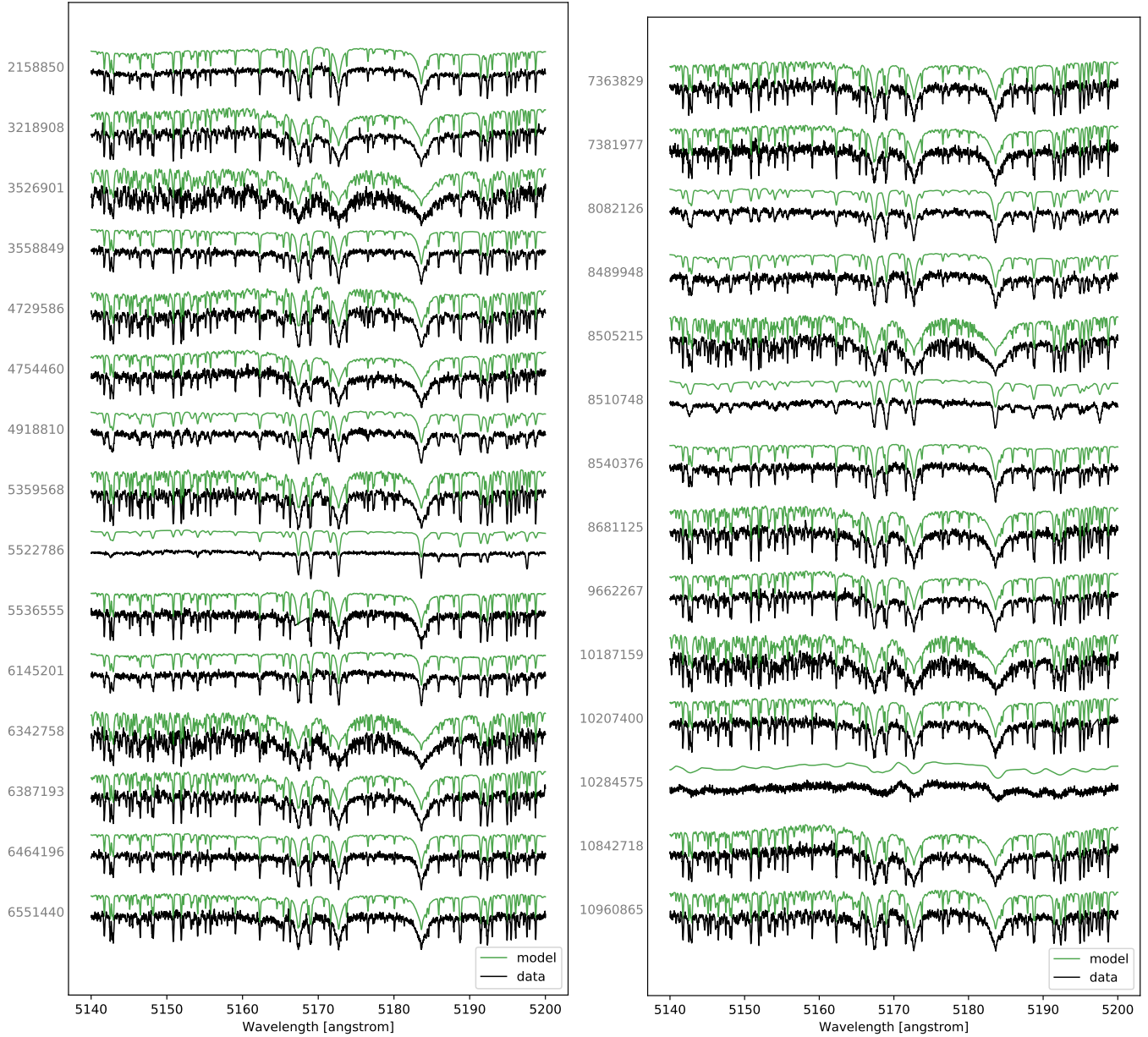


Figure 11. Subaru/HDS high resolution spectra near the Mg triplet (black). KIC numbers are shown at the left of the corresponding spectrum. Green curves are the best-match model returned by the `Specmatch-Emp` code (Yee et al. 2017).

For the stars with spectroscopic parameters, we fitted stellar evolutionary models to the spectroscopic T_{eff} , $\log g$, and $[\text{Fe}/\text{H}]$, along with the *Gaia* DR2 parallax (Gaia Collaboration et al. 2018; Bailer-Jones et al. 2018) and the 2MASS K -magnitude. The K -magnitude was corrected for the extinction A_K using the value of $E(B - V)$ and extinction vectors from the dust map (Bayestar17; Green et al. 2018). The 30% fractional uncertainty was assumed for A_K following Fulton & Petigura (2018). The stellar-evolutionary models were from the Dartmouth Stellar Evolution Database (Dot-

ter et al. 2008) and were compared to the data using the `isochrones` package by Morton (2015).

For the stars without available spectroscopy, we fitted stellar models to the 2MASS JHK colors instead of T_{eff} , $\log g$, and $[\text{Fe}/\text{H}]$. We also floated A_V as a free parameter rather than using a value from the extinction map. This is because the model sometimes failed to fit the JHK colors corrected for the map-based extinction and yielded unreasonably small formal uncertainties for T_{eff} when combined with the precise *Gaia* parallax. Here A_V is introduced to mitigate such incompleteness of the model.

4.4. Results

The results of the isochrone modeling for all the stars are summarized in Table 2. Here the second to seventh columns report constraints from the isochrone model (median and 68% credible interval of the marginal posterior), and the remaining columns show the values from raw spectroscopy when available. We cross-checked the resulting stellar radii against the values in Berger et al. (2018) and found a good agreement without any apparent systematic trend, although the radius precision was improved to a few percent for the sample with spectroscopic information added. Figure 12 shows the radii and

effective temperatures of the spectroscopic (orange circles) and photometric (blue squares) samples along with all the *Kepler* field stars (gray dots) from Berger et al. (2018).

The distribution of [Fe/H] from the final isochrone fit has the mean of 0.00 and the standard deviation of 0.15. These values agree with the typical metallicity of the *Kepler* field stars (Dong et al. 2014; Guo et al. 2017). That said, the [Fe/H] distribution of our sample is skewed toward higher values (see Section 6.3). This explains the lack of smaller stars along the main-sequence in our sample (Figure 12).

Table 2. Parameters of the Host Stars.

KIC	T_{eff} (K)	$\log g$ (cgs)	[Fe/H]	M_{\star} (M_{\odot})	R_{\star} (R_{\odot})	$\log_{10}(\text{age/yr})$	Source [†]	T_{eff} (K)	$\log g$ (cgs)	[Fe/H]
1717722	4689 ⁺⁸⁰ ₋₇₅	4.63 ^{+0.02} _{-0.02}	-0.28 ^{+0.08} _{-0.08}	0.68 ^{+0.02} _{-0.02}	0.66 ^{+0.01} _{-0.01}	9.9 ^{+0.2} _{-0.4}	APOGEE	4669	4.48	-0.38
2158850	5980 ⁺⁹⁶ ₋₉₈	4.34 ^{+0.02} _{-0.03}	-0.04 ^{+0.08} _{-0.08}	1.05 ^{+0.05} _{-0.04}	1.15 ^{+0.02} _{-0.02}	9.7 ^{+0.1} _{-0.2}	HDS	5976	4.28	-0.06
2162635	4964 ⁺⁷³ ₋₆₀	3.62 ^{+0.03} _{-0.03}	0.05 ^{+0.09} _{-0.04}	1.03 ^{+0.06} _{-0.04}	2.61 ^{+0.05} _{-0.05}	10.02 ^{+0.07} _{-0.09}	CKS	4921	3.62	0.08
3111510	6230 ⁺²⁶⁰ ₋₂₆₅	4.24 ^{+0.05} _{-0.05}	0.1 ^{+0.1} _{-0.2}	1.19 ^{+0.08} _{-0.08}	1.36 ^{+0.06} _{-0.05}	9.5 ^{+0.2} _{-0.3}
3218908 ^b	5578 ⁺⁹¹ ₋₇₇	4.31 ^{+0.03} _{-0.03}	0.18 ^{+0.08} _{-0.08}	0.96 ^{+0.04} _{-0.03}	1.13 ^{+0.03} _{-0.03}	10.01 ^{+0.08} _{-0.12}	HDS	5561	4.25	0.24
3230491	5406 ⁺⁸⁶ ₋₉₀	4.53 ^{+0.03} _{-0.03}	-0.21 ^{+0.08} _{-0.08}	0.83 ^{+0.04} _{-0.04}	0.82 ^{+0.02} _{-0.02}	9.8 ^{+0.2} _{-0.3}	LAMOST	5405	4.51	-0.28
3239945	4851 ⁺⁶³ ₋₆₄	4.59 ^{+0.02} _{-0.02}	0.02 ^{+0.08} _{-0.08}	0.78 ^{+0.03} _{-0.03}	0.745 ^{+0.008} _{-0.008}	9.8 ^{+0.2} _{-0.4}	CKS	4868	4.57	0.03
3241604	6358 ⁺³⁵³ ₋₂₅₀	4.03 ^{+0.06} _{-0.06}	0.1 ^{+0.1} _{-0.1}	1.42 ^{+0.08} _{-0.06}	1.9 ^{+0.1} _{-0.1}	9.4 ^{+0.1} _{-0.1}
3346436	5882 ⁺¹⁰⁰ ₋₁₀₄	3.80 ^{+0.06} _{-0.04}	-0.03 ^{+0.08} _{-0.01}	1.23 ^{+0.16} _{-0.06}	2.33 ^{+0.07} _{-0.07}	9.66 ^{+0.07} _{-0.11}	LAMOST	5887	3.92	0.00
3351971	5539 ⁺¹⁷² ₋₁₅₅	4.49 ^{+0.03} _{-0.04}	-0.0 ^{+0.2} _{-0.2}	0.92 ^{+0.05} _{-0.06}	0.90 ^{+0.02} _{-0.02}	9.7 ^{+0.3} _{-0.5}
3526901	5082 ⁺⁸⁵ ₋₆₈	3.85 ^{+0.05} _{-0.05}	0.01 ^{+0.02} _{-0.01}	0.98 ^{+0.04} _{-0.02}	2.0 ^{+0.1} _{-0.1}	10.08 ^{+0.03} _{-0.06}	HDS	4881	4.49	-0.17
3558849	6026 ⁺¹¹¹ ₋₁₀₄	4.14 ^{+0.03} _{-0.03}	0.01 ^{+0.06} _{-0.08}	1.14 ^{+0.05} _{-0.04}	1.51 ^{+0.05} _{-0.04}	9.72 ^{+0.09} _{-0.10}	HDS	5976	4.25	-0.06
3756801	5857 ⁺⁹¹ ₋₈₇	3.68 ^{+0.07} _{-0.04}	-0.04 ^{+0.15} _{-0.01}	1.3 ^{+0.2} _{-0.1}	2.77 ^{+0.08} _{-0.08}	9.5 ^{+0.1} _{-0.1}	CKS	5834	3.82	0.12
3962440	6453 ⁺¹⁰⁴ ₋₁₀₁	3.90 ^{+0.06} _{-0.05}	0.03 ^{+0.06} _{-0.04}	1.55 ^{+0.07} _{-0.07}	2.3 ^{+0.2} _{-0.2}	9.33 ^{+0.06} _{-0.05}	CKS	6417	4.16	-0.07
4042088	6463 ⁺¹⁰⁰ ₋₁₀₉	4.23 ^{+0.02} _{-0.03}	-0.04 ^{+0.08} _{-0.08}	1.25 ^{+0.04} _{-0.05}	1.43 ^{+0.03} _{-0.03}	9.4 ^{+0.1} _{-0.1}	LAMOST	6473	4.09	-0.05
4729586	4966 ⁺³⁶ ₋₄₃	2.71 ^{+0.04} _{-0.04}	0.02 ^{+0.08} _{-0.04}	2.65 ^{+0.08} _{-0.04}	12.0 ^{+0.6} _{-0.6}	8.76 ^{+0.02} _{-0.03}	HDS	4812	2.96	-0.06
4754460	5637 ⁺⁹¹ ₋₈₅	4.30 ^{+0.03} _{-0.03}	-0.22 ^{+0.08} _{-0.07}	0.87 ^{+0.03} _{-0.02}	1.10 ^{+0.03} _{-0.03}	10.07 ^{+0.04} _{-0.07}	HDS	5514	4.56	-0.35
4754691 ^b	5303 ⁺⁷¹ ₋₉₆	4.421 ^{+0.012} _{-0.009}	0.2 ^{+0.1} _{-0.2}	0.88 ^{+0.02} _{-0.02}	0.95 ^{+0.01} _{-0.01}	10.10 ^{+0.02} _{-0.05}
4772953	9431 ⁺⁶⁸¹ ₋₅₅₄	4.16 ^{+0.05} _{-0.06}	-0.0 ^{+0.2} _{-0.2}	2.2 ^{+0.1} _{-0.1}	2.04 ^{+0.10} _{-0.09}	8.6 ^{+0.2} _{-0.1}
4918810	6144 ⁺⁸⁰ ₋₈₇	4.05 ^{+0.02} _{-0.02}	0.09 ^{+0.08} _{-0.06}	1.31 ^{+0.03} _{-0.07}	1.78 ^{+0.04} _{-0.03}	9.56 ^{+0.07} _{-0.05}	HDS	6106	4.12	0.12
5010054	5940 ⁺¹⁰⁰ ₋₉₃	4.03 ^{+0.02} _{-0.02}	0.00 ^{+0.06} _{-0.13}	1.16 ^{+0.03} _{-0.03}	1.72 ^{+0.04} _{-0.04}	9.72 ^{+0.08} _{-0.09}	LAMOST	5898	4.01	-0.11
5184479	5953 ⁺¹¹⁰ ₋₉₄	4.17 ^{+0.03} _{-0.03}	0.10 ^{+0.07} _{-0.07}	1.13 ^{+0.05} _{-0.05}	1.46 ^{+0.04} _{-0.04}	9.8 ^{+0.1} _{-0.1}	LAMOST	5954	4.15	0.11
5351250	5534 ⁺⁷⁵ ₋₈₂	4.52 ^{+0.02} _{-0.03}	0.07 ^{+0.07} _{-0.08}	0.96 ^{+0.03} _{-0.04}	0.89 ^{+0.02} _{-0.02}	9.4 ^{+0.3} _{-0.4}	CKS	5588	4.58	0.12
5359568	4858 ⁺¹⁰⁸ ₋₉₈	2.96 ^{+0.05} _{-0.07}	-0.12 ^{+0.04} _{-0.04}	1.2 ^{+0.1} _{-0.2}	5.9 ^{+0.2} _{-0.2}	9.8 ^{+0.2} _{-0.2}	HDS	4841	3.16	0.08
5536555	5984 ⁺⁹¹ ₋₁₀₁	4.41 ^{+0.03} _{-0.03}	-0.02 ^{+0.08} _{-0.08}	1.06 ^{+0.05} _{-0.05}	1.06 ^{+0.02} _{-0.02}	9.5 ^{+0.2} _{-0.3}	HDS	5992	4.40	-0.03
5623581	6228 ⁺²⁹⁷ ₋₃₁₆	4.21 ^{+0.06} _{-0.06}	0.1 ^{+0.1} _{-0.1}	1.21 ^{+0.08} _{-0.10}	1.43 ^{+0.07} _{-0.07}	9.6 ^{+0.2} _{-0.3}
5732155	6395 ⁺²²² ₋₁₈₃	3.90 ^{+0.05} _{-0.04}	0.11 ^{+0.13} _{-0.08}	1.57 ^{+0.06} _{-0.06}	2.3 ^{+0.1} _{-0.1}	9.33 ^{+0.08} _{-0.08}
5871088	4675 ⁺¹⁶⁷ ₋₁₄₈	4.63 ^{+0.02} _{-0.02}	-0.2 ^{+0.2} _{-0.2}	0.71 ^{+0.04} _{-0.04}	0.67 ^{+0.03} _{-0.03}	9.7 ^{+0.3} _{-0.6}

Table 2 continued

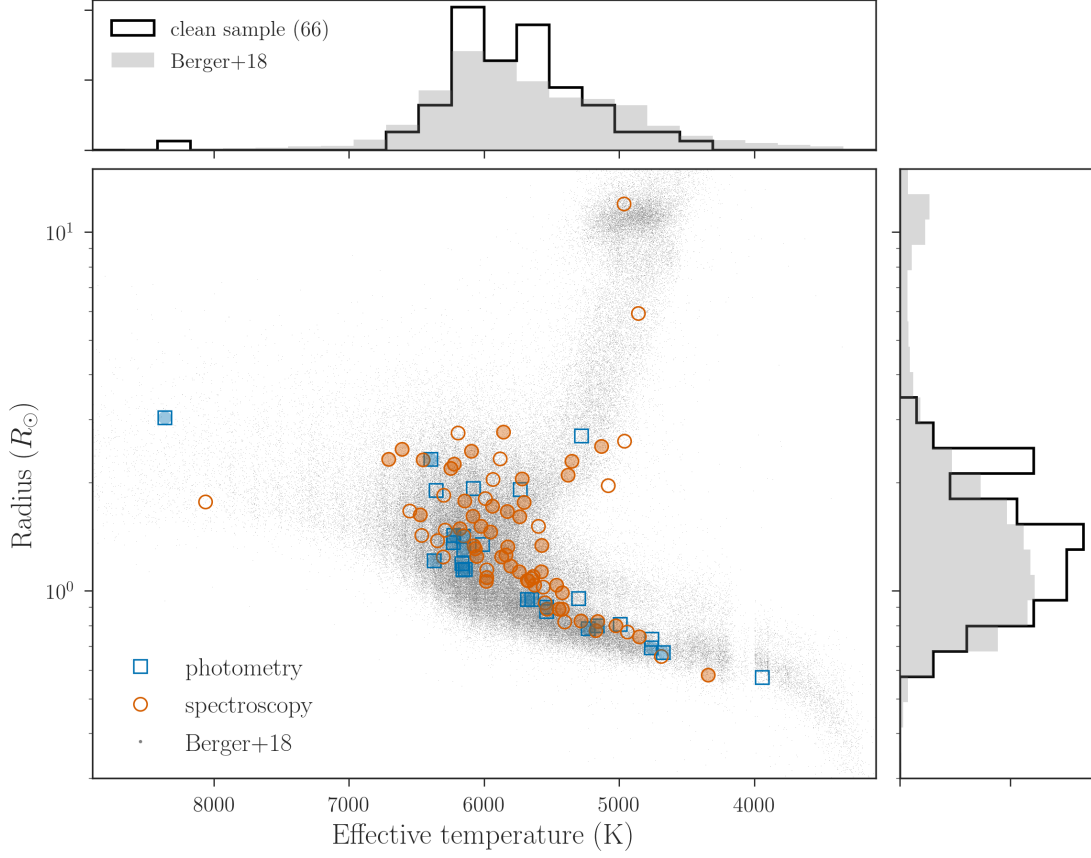


Figure 12. The host stars in the HR diagram (open circles/squares) and the *Kepler* stars from Berger et al. (2018) (gray dots). The filled circles/squares correspond to the host stars in the clean sample (Section 6), whose corresponding histograms are shown with the thick black lines in the top and right panels. The gray histograms are for the *Kepler* field stars. There are 66 stars in the clean sample (compared to 67 candidates) because KIC 10024862 has two long-period transiting planet candidates.

Table 2 (continued)

KIC	T_{eff} (K)	$\log g$ (cgs)	[Fe/H]	M_* (M_{\odot})	R_* (R_{\odot})	$\log_{10}(\text{age}/\text{yr})$	Source [†]	T_{eff} (K)	$\log g$ (cgs)	[Fe/H]
5942949	4765^{+169}_{-136}	$4.62^{+0.02}_{-0.02}$	$-0.2^{+0.2}_{-0.2}$	$0.73^{+0.04}_{-0.03}$	$0.69^{+0.02}_{-0.02}$	$9.7^{+0.3}_{-0.6}$
5951458	5993^{+99}_{-88}	$4.00^{+0.02}_{-0.02}$	$-0.05^{+0.09}_{-0.09}$	$1.20^{+0.05}_{-0.03}$	$1.81^{+0.03}_{-0.04}$	$9.65^{+0.09}_{-0.04}$	LAMOST	5948	4.02	-0.11
6145201	6302^{+133}_{-119}	$4.01^{+0.03}_{-0.03}$	$-0.19^{+0.14}_{-0.07}$	$1.26^{+0.08}_{-0.06}$	$1.85^{+0.05}_{-0.05}$	$9.52^{+0.09}_{-0.06}$	HDS	6302	4.05	-0.24
6186417	6151^{+270}_{-280}	$4.26^{+0.06}_{-0.06}$	$0.0^{+0.1}_{-0.2}$	$1.15^{+0.08}_{-0.09}$	$1.31^{+0.09}_{-0.07}$	$9.6^{+0.2}_{-0.3}$
6191521	5574^{+97}_{-75}	$4.18^{+0.04}_{-0.04}$	$0.16^{+0.09}_{-0.08}$	$0.98^{+0.04}_{-0.03}$	$1.34^{+0.06}_{-0.06}$	$10.06^{+0.05}_{-0.08}$	M17	5512	4.22	0.20
6203563	6370^{+205}_{-185}	$4.35^{+0.03}_{-0.04}$	$-0.1^{+0.2}_{-0.2}$	$1.19^{+0.06}_{-0.07}$	$1.21^{+0.03}_{-0.02}$	$9.3^{+0.3}_{-0.4}$
6342758	4942^{+67}_{-64}	$4.57^{+0.02}_{-0.02}$	$0.07^{+0.08}_{-0.08}$	$0.81^{+0.03}_{-0.03}$	$0.769^{+0.010}_{-0.009}$	$9.8^{+0.2}_{-0.4}$	HDS	4974	4.51	0.11
6387193	5566^{+97}_{-93}	$4.40^{+0.04}_{-0.03}$	$0.18^{+0.08}_{-0.08}$	$0.96^{+0.05}_{-0.04}$	$1.03^{+0.02}_{-0.02}$	$9.9^{+0.1}_{-0.2}$	HDS	5581	4.28	0.26
6464196	5870^{+106}_{-113}	$4.25^{+0.03}_{-0.03}$	$-0.07^{+0.09}_{-0.10}$	$1.01^{+0.04}_{-0.05}$	$1.24^{+0.04}_{-0.03}$	$9.86^{+0.08}_{-0.08}$	HDS	5836	4.27	-0.14
6510758	5422^{+75}_{-59}	$4.41^{+0.02}_{-0.02}$	$0.17^{+0.08}_{-0.08}$	$0.91^{+0.04}_{-0.02}$	$0.99^{+0.01}_{-0.01}$	$10.04^{+0.07}_{-0.13}$	LAMOST	5354	4.35	0.21
6551440	5804^{+102}_{-101}	$4.31^{+0.03}_{-0.03}$	$0.07^{+0.08}_{-0.06}$	$1.02^{+0.04}_{-0.04}$	$1.17^{+0.02}_{-0.02}$	$9.9^{+0.1}_{-0.1}$	HDS	5795	4.29	0.07
6690896	6181^{+96}_{-99}	$4.09^{+0.03}_{-0.02}$	$-0.41^{+0.09}_{-0.07}$	$1.01^{+0.05}_{-0.04}$	$1.49^{+0.03}_{-0.03}$	$9.83^{+0.06}_{-0.08}$	LAMOST	6132	4.25	-0.50
6804821	8366^{+1344}_{-796}	$3.83^{+0.10}_{-0.07}$	$0.1^{+0.1}_{-0.1}$	$2.3^{+0.3}_{-0.2}$	$3.0^{+0.1}_{-0.2}$	$8.8^{+0.1}_{-0.2}$
7040629	6055^{+105}_{-110}	$4.29^{+0.03}_{-0.02}$	$0.03^{+0.07}_{-0.08}$	$1.11^{+0.04}_{-0.04}$	$1.25^{+0.02}_{-0.02}$	$9.7^{+0.1}_{-0.1}$	CKS	6053	4.24	0.02

Table 2 continued

Table 2 (continued)

KIC	T_{eff} (K)	$\log g$ (cgs)	[Fe/H]	M_* (M_{\odot})	R_* (R_{\odot})	$\log_{10}(\text{age/yr})$	Source [†]	T_{eff} (K)	$\log g$ (cgs)	[Fe/H]
7176219	5280 ⁺⁹³ ₋₇₉	3.70 ^{+0.02} _{-0.02}	0.04 ^{+0.06} _{-0.03}	1.34 ^{+0.03} _{-0.03}	2.70 ^{+0.05} _{-0.06}	9.61 ^{+0.03} _{-0.03}
7363829	5705 ⁺¹¹⁰ ₋₁₀₉	4.01 ^{+0.04} _{-0.04}	0.17 ^{+0.08} _{-0.08}	1.15 ^{+0.09} _{-0.05}	1.76 ^{+0.08} _{-0.08}	9.82 ^{+0.07} _{-0.11}	HDS	5668	4.06	0.21
7381977	5551 ⁺⁹⁶ ₋₉₅	4.46 ^{+0.04} _{-0.04}	-0.05 ^{+0.08} _{-0.08}	0.91 ^{+0.05} _{-0.04}	0.93 ^{+0.02} _{-0.02}	9.9 ^{+0.2} _{-0.3}	HDS	5557	4.40	-0.08
7447005	5649 ⁺¹⁸⁰ ₋₁₆₈	4.47 ^{+0.04} _{-0.04}	0.0 ^{+0.1} _{-0.2}	0.95 ^{+0.06} _{-0.06}	0.95 ^{+0.03} _{-0.03}	9.7 ^{+0.3} _{-0.5}
7672940	6553 ⁺¹⁰¹ ₋₁₀₇	4.13 ^{+0.03} _{-0.03}	0.01 ^{+0.07} _{-0.08}	1.36 ^{+0.04} _{-0.04}	1.67 ^{+0.06} _{-0.06}	9.39 ^{+0.05} _{-0.06}	CKS	6532	4.19	-0.04
7875441	6082 ⁺²⁶⁷ ₋₃₂₆	3.99 ^{+0.06} _{-0.05}	0.10 ^{+0.12} _{-0.08}	1.35 ^{+0.08} _{-0.14}	1.9 ^{+0.1} _{-0.1}	9.5 ^{+0.2} _{-0.1}
7906827	6157 ⁺²³¹ ₋₂₀₂	4.37 ^{+0.04} _{-0.05}	-0.0 ^{+0.2} _{-0.2}	1.12 ^{+0.07} _{-0.08}	1.14 ^{+0.06} _{-0.06}	9.4 ^{+0.3} _{-0.5}
7947784	6012 ⁺³²⁵ ₋₂₇₉	4.23 ^{+0.07} _{-0.07}	0.1 ^{+0.1} _{-0.1}	1.12 ^{+0.10} _{-0.09}	1.35 ^{+0.08} _{-0.07}	9.7 ^{+0.2} _{-0.3}
8012732	5841 ⁺⁹⁸ ₋₁₀₁	4.26 ^{+0.03} _{-0.03}	0.09 ^{+0.07} _{-0.07}	1.05 ^{+0.04} _{-0.04}	1.26 ^{+0.03} _{-0.03}	9.8 ^{+0.1} _{-0.1}	SPOCS	5846	4.21	0.11
8082126	6289 ⁺⁹⁶ ₋₁₁₀	4.18 ^{+0.03} _{-0.03}	-0.08 ^{+0.08} _{-0.09}	1.20 ^{+0.04} _{-0.05}	1.48 ^{+0.03} _{-0.03}	9.57 ^{+0.08} _{-0.07}	HDS	6274	4.12	-0.14
8168680	6347 ⁺¹⁰⁴ ₋₁₀₂	4.17 ^{+0.03} _{-0.03}	-0.41 ^{+0.09} _{-0.08}	1.03 ^{+0.05} _{-0.05}	1.38 ^{+0.02} _{-0.02}	9.76 ^{+0.08} _{-0.09}	LAMOST	6338	4.17	-0.49
8313257	5164 ⁺¹⁵⁰ ₋₁₃₁	4.56 ^{+0.03} _{-0.03}	-0.0 ^{+0.2} _{-0.2}	0.84 ^{+0.04} _{-0.04}	0.80 ^{+0.02} _{-0.02}	9.8 ^{+0.2} _{-0.5}
8410697	5648 ⁺⁹⁸ ₋₈₅	4.33 ^{+0.03} _{-0.02}	-0.07 ^{+0.10} _{-0.09}	0.93 ^{+0.04} _{-0.04}	1.08 ^{+0.01} _{-0.01}	10.00 ^{+0.07} _{-0.09}	LAMOST	5617	4.26	-0.11
8426957	5936 ⁺¹⁰² ₋₉₉	3.94 ^{+0.03} _{-0.03}	0.11 ^{+0.10} _{-0.07}	1.33 ^{+0.06} _{-0.07}	2.05 ^{+0.04} _{-0.04}	9.59 ^{+0.05} _{-0.05}	LAMOST	5922	3.79	0.15
8489948	6152 ⁺⁹⁴ ₋₉₄	4.20 ^{+0.03} _{-0.03}	0.00 ^{+0.06} _{-0.07}	1.17 ^{+0.04} _{-0.04}	1.42 ^{+0.05} _{-0.05}	9.63 ^{+0.09} _{-0.08}	HDS	6123	4.28	-0.05
8505215 ^{ab}	5176 ⁺⁷³ ₋₆₆	4.536 ^{+0.015} _{-0.009}	-0.25 ^{+0.07} _{-0.07}	0.75 ^{+0.02} _{-0.01}	0.775 ^{+0.007} _{-0.007}	10.07 ^{+0.05} _{-0.11}	HDS	4954	4.54	-0.49
8510748	6608 ⁺¹⁰⁵ ₋₁₀₂	3.87 ^{+0.03} _{-0.03}	0.10 ^{+0.08} _{-0.07}	1.66 ^{+0.04} _{-0.04}	2.48 ^{+0.10} _{-0.09}	9.23 ^{+0.04} _{-0.04}	HDS	6604	3.96	0.11
8636333	6166 ⁺²⁵⁰ ₋₂₃₄	4.34 ^{+0.05} _{-0.05}	-0.0 ^{+0.2} _{-0.2}	1.13 ^{+0.08} _{-0.08}	1.19 ^{+0.06} _{-0.05}	9.5 ^{+0.3} _{-0.4}
8648356	8062 ⁺¹⁰⁷ ₋₁₀₈	4.17 ^{+0.02} _{-0.02}	-0.13 ^{+0.08} _{-0.09}	1.70 ^{+0.05} _{-0.05}	1.77 ^{+0.03} _{-0.03}	8.93 ^{+0.08} _{-0.09}	LAMOST	8080	3.98	-0.17
8681125	5466 ⁺⁷⁹ ₋₆₈	4.37 ^{+0.03} _{-0.03}	0.20 ^{+0.08} _{-0.08}	0.93 ^{+0.04} _{-0.02}	1.04 ^{+0.03} _{-0.03}	10.04 ^{+0.06} _{-0.12}	HDS	5435	4.16	0.26
8738735	6085 ⁺⁸⁹ ₋₁₀₈	4.10 ^{+0.03} _{-0.03}	0.02 ^{+0.06} _{-0.07}	1.19 ^{+0.06} _{-0.04}	1.61 ^{+0.04} _{-0.04}	9.67 ^{+0.09} _{-0.08}	CKS	6052	4.12	-0.02
8800954 ^{ab}	5285 ⁺⁸¹ ₋₇₄	4.52 ^{+0.03} _{-0.02}	-0.13 ^{+0.08} _{-0.08}	0.82 ^{+0.04} _{-0.03}	0.82 ^{+0.01} _{-0.01}	10.0 ^{+0.1} _{-0.2}	CKS	5223	4.57	-0.23
9388752	6195 ⁺¹¹⁸ ₋₉₄	3.74 ^{+0.03} _{-0.02}	-0.03 ^{+0.03} _{-0.02}	1.51 ^{+0.09} _{-0.05}	2.75 ^{+0.04} _{-0.05}	9.37 ^{+0.05} _{-0.07}	LAMOST	6146	3.88	-0.24
9413313	5160 ⁺⁷³ ₋₇₄	4.54 ^{+0.03} _{-0.03}	0.11 ^{+0.08} _{-0.08}	0.86 ^{+0.04} _{-0.03}	0.82 ^{+0.01} _{-0.01}	9.8 ^{+0.2} _{-0.4}	SPOCS	5196	4.49	0.16
9419047	5721 ⁺⁹⁹ ₋₉₉	3.92 ^{+0.03} _{-0.02}	0.10 ^{+0.06} _{-0.05}	1.27 ^{+0.05} _{-0.05}	2.05 ^{+0.04} _{-0.04}	9.66 ^{+0.07} _{-0.05}	LAMOST	5691	3.99	0.14
9581498	6155 ⁺²²⁰ ₋₂₆₄	4.20 ^{+0.07} _{-0.06}	0.1 ^{+0.1} _{-0.1}	1.20 ^{+0.08} _{-0.11}	1.4 ^{+0.1} _{-0.1}	9.6 ^{+0.2} _{-0.2}
9662267	5742 ⁺¹⁰³ ₋₁₀₀	4.33 ^{+0.03} _{-0.03}	0.07 ^{+0.08} _{-0.07}	0.99 ^{+0.04} _{-0.04}	1.13 ^{+0.03} _{-0.03}	9.9 ^{+0.1} _{-0.1}	HDS	5747	4.25	0.08
9663113	6247 ⁺⁹⁹ ₋₉₉	3.93 ^{+0.02} _{-0.02}	0.19 ^{+0.08} _{-0.08}	1.51 ^{+0.04} _{-0.04}	2.20 ^{+0.07} _{-0.07}	9.40 ^{+0.04} _{-0.04}	CKS	6217	4.07	0.25
9704149	5679 ⁺¹⁷⁸ ₋₁₆₈	4.47 ^{+0.03} _{-0.04}	-0.0 ^{+0.1} _{-0.2}	0.96 ^{+0.06} _{-0.07}	0.94 ^{+0.03} _{-0.03}	9.7 ^{+0.3} _{-0.5}
9822143	5379 ⁺¹⁰⁰ ₋₈₀	3.75 ^{+0.03} _{-0.02}	-0.47 ^{+0.04} _{-0.02}	0.91 ^{+0.04} _{-0.03}	2.10 ^{+0.04} _{-0.04}	10.04 ^{+0.06} _{-0.08}	LAMOST	5392	3.63	-0.67
9838291	6094 ⁺¹⁰² ₋₁₀₉	3.84 ^{+0.02} _{-0.03}	0.10 ^{+0.07} _{-0.06}	1.51 ^{+0.04} _{-0.04}	2.45 ^{+0.06} _{-0.05}	9.44 ^{+0.04} _{-0.04}	LAMOST	6024	3.83	0.10
9970525	6305 ⁺¹⁰³ ₋₁₀₃	4.27 ^{+0.03} _{-0.03}	-0.3 ^{+0.1} _{-0.1}	1.04 ^{+0.05} _{-0.05}	1.24 ^{+0.02} _{-0.02}	9.7 ^{+0.1} _{-0.1}	LAMOST	6301	4.23	-0.39
10024862	5983 ⁺¹⁰⁶ ₋₁₀₃	4.38 ^{+0.06} _{-0.06}	-0.08 ^{+0.08} _{-0.09}	1.04 ^{+0.05} _{-0.05}	1.09 ^{+0.07} _{-0.07}	9.7 ^{+0.2} _{-0.3}	SPOCS	5979	4.38	-0.12
10058021	4761 ⁺¹¹³ ₋₁₀₂	4.59 ^{+0.02} _{-0.02}	0.0 ^{+0.1} _{-0.1}	0.76 ^{+0.03} _{-0.03}	0.73 ^{+0.01} _{-0.01}	9.9 ^{+0.2} _{-0.4}
10187159	5026 ⁺⁷² ₋₆₂	4.55 ^{+0.03} _{-0.02}	0.10 ^{+0.08} _{-0.08}	0.82 ^{+0.04} _{-0.03}	0.80 ^{+0.01} _{-0.01}	9.9 ^{+0.2} _{-0.3}	HDS	5000	4.48	0.13
10190048 ^b	4995 ⁺⁸⁴ ₋₈₉	4.53 ^{+0.02} _{-0.01}	0.1 ^{+0.1} _{-0.1}	0.81 ^{+0.03} _{-0.02}	0.81 ^{+0.02} _{-0.02}	10.04 ^{+0.06} _{-0.16}
10207400	5679 ⁺¹⁰³ ₋₉₈	4.37 ^{+0.04} _{-0.04}	0.07 ^{+0.08} _{-0.07}	0.97 ^{+0.05} _{-0.04}	1.07 ^{+0.04} _{-0.03}	9.9 ^{+0.1} _{-0.1}	HDS	5693	4.28	0.10
10255705	5133 ⁺¹⁰³ ₋₉₉	3.69 ^{+0.04} _{-0.04}	0.01 ^{+0.03} _{-0.02}	1.11 ^{+0.16} _{-0.06}	2.5 ^{+0.1} _{-0.1}	9.89 ^{+0.09} _{-0.22}	APOGEE	5110	3.71	-0.14
10284575	6473 ⁺¹⁰⁶ ₋₁₁₄	4.15 ^{+0.02} _{-0.02}	0.09 ^{+0.08} _{-0.07}	1.35 ^{+0.03} _{-0.03}	1.63 ^{+0.03} _{-0.03}	9.40 ^{+0.06} _{-0.07}	HDS	6506	3.83	0.13
10287723	4343 ⁺⁴⁹ ₋₄₆	4.68 ^{+0.01} _{-0.01}	-0.43 ^{+0.09} _{-0.08}	0.59 ^{+0.02} _{-0.01}	0.582 ^{+0.006} _{-0.006}	9.9 ^{+0.2} _{-0.4}	APOGEE	4227	4.60	-0.56
10321319	5598 ⁺¹⁰¹ ₋₉₂	4.08 ^{+0.02} _{-0.02}	0.02 ^{+0.05} _{-0.04}	1.00 ^{+0.03} _{-0.03}	1.51 ^{+0.02} _{-0.03}	10.02 ^{+0.05} _{-0.07}	LAMOST	5595	3.93	-0.10

Table 2 continued

Table 2 (continued)

KIC	T_{eff} (K)	$\log g$ (cgs)	[Fe/H]	M_* (M_{\odot})	R_* (R_{\odot})	$\log_{10}(\text{age/yr})$	Source [†]	T_{eff} (K)	$\log g$ (cgs)	[Fe/H]
10384911	6065 ⁺¹⁰⁰ ₋₁₀₆	4.20 ^{+0.03} _{-0.03}	-0.30 ^{+0.09} _{-0.10}	0.98 ^{+0.05} _{-0.05}	1.31 ^{+0.03} _{-0.03}	9.86 ^{+0.08} _{-0.10}	LAMOST	6031	4.24	-0.37
10403228	3942 ⁺⁸¹ ₋₅₅	4.69 ^{+0.01} _{-0.01}	0.0 ^{+0.1} _{-0.2}	0.59 ^{+0.01} _{-0.01}	0.574 ^{+0.009} _{-0.010}	9.9 ^{+0.2} _{-0.4}
10460629	6222 ⁺⁸⁰ ₋₇₄	3.90 ^{+0.02} _{-0.02}	0.08 ^{+0.08} _{-0.06}	1.49 ^{+0.03} _{-0.04}	2.26 ^{+0.06} _{-0.06}	9.43 ^{+0.04} _{-0.03}	CKS	6140	4.12	0.06
10525077	6140 ⁺²⁰⁷ ₋₂₃₅	4.37 ^{+0.04} _{-0.05}	-0.0 ^{+0.2} _{-0.2}	1.11 ^{+0.07} _{-0.09}	1.15 ^{+0.05} _{-0.04}	9.5 ^{+0.3} _{-0.5}
10602068	5540 ⁺¹⁵⁸ ₋₁₃₃	4.52 ^{+0.03} _{-0.04}	-0.0 ^{+0.2} _{-0.2}	0.92 ^{+0.04} _{-0.06}	0.87 ^{+0.02} _{-0.02}	9.6 ^{+0.3} _{-0.5}
10683701	5736 ⁺⁹⁹ ₋₉₃	3.98 ^{+0.02} _{-0.02}	-0.46 ^{+0.05} _{-0.03}	0.90 ^{+0.03} _{-0.02}	1.61 ^{+0.03} _{-0.03}	10.03 ^{+0.05} _{-0.06}	LAMOST	5708	4.00	-0.63
10724544	5735 ⁺²¹⁰ ₋₂₀₈	3.95 ^{+0.05} _{-0.04}	0.10 ^{+0.11} _{-0.07}	1.21 ^{+0.11} _{-0.07}	1.92 ^{+0.08} _{-0.08}	9.7 ^{+0.1} _{-0.1}
10842718	5446 ⁺⁸⁹ ₋₈₆	4.49 ^{+0.03} _{-0.03}	0.01 ^{+0.08} _{-0.08}	0.90 ^{+0.04} _{-0.04}	0.89 ^{+0.02} _{-0.02}	9.8 ^{+0.2} _{-0.3}	HDS	5463	4.45	0.02
10960865	5350 ⁺¹⁰⁰ ₋₈₇	3.80 ^{+0.03} _{-0.03}	0.18 ^{+0.07} _{-0.07}	1.22 ^{+0.07} _{-0.05}	2.30 ^{+0.06} _{-0.06}	9.76 ^{+0.06} _{-0.08}	HDS	5322	3.93	0.26
10976409	6708 ⁺¹⁰³ ₋₁₀₄	3.93 ^{+0.03} _{-0.03}	0.17 ^{+0.08} _{-0.08}	1.66 ^{+0.04} _{-0.04}	2.33 ^{+0.08} _{-0.08}	9.21 ^{+0.04} _{-0.05}	LAMOST	6717	3.95	0.24
11342550	5628 ⁺⁹⁹ ₋₉₅	4.38 ^{+0.04} _{-0.04}	0.04 ^{+0.08} _{-0.08}	0.95 ^{+0.04} _{-0.04}	1.04 ^{+0.04} _{-0.04}	9.9 ^{+0.1} _{-0.2}	CKS	5623	4.33	0.04
11558724	6079 ⁺¹⁰² ₋₁₁₇	4.24 ^{+0.03} _{-0.03}	0.06 ^{+0.07} _{-0.07}	1.14 ^{+0.04} _{-0.04}	1.34 ^{+0.04} _{-0.04}	9.7 ^{+0.1} _{-0.1}	LAMOST	6065	4.26	0.07
11709124	5675 ⁺⁹⁷ ₋₁₀₀	4.36 ^{+0.03} _{-0.03}	0.04 ^{+0.07} _{-0.08}	0.96 ^{+0.04} _{-0.04}	1.07 ^{+0.03} _{-0.03}	9.9 ^{+0.1} _{-0.1}	CKS	5666	4.35	0.02
12066509	5826 ⁺⁹³ ₋₉₉	4.22 ^{+0.04} _{-0.04}	0.13 ^{+0.08} _{-0.08}	1.06 ^{+0.05} _{-0.04}	1.33 ^{+0.05} _{-0.05}	9.86 ^{+0.09} _{-0.12}	LAMOST	5844	4.10	0.18
12266600	5231 ⁺¹⁷⁹ ₋₁₃₉	4.57 ^{+0.02} _{-0.03}	-0.1 ^{+0.2} _{-0.2}	0.83 ^{+0.04} _{-0.04}	0.78 ^{+0.02} _{-0.02}	9.6 ^{+0.3} _{-0.5}
12356617	5829 ⁺⁸⁴ ₋₁₀₄	4.06 ^{+0.03} _{-0.02}	0.17 ^{+0.07} _{-0.08}	1.15 ^{+0.09} _{-0.04}	1.66 ^{+0.03} _{-0.03}	9.80 ^{+0.06} _{-0.12}	CKS	5804	4.03	0.21
12454613	5424 ⁺⁸⁰ ₋₈₉	4.51 ^{+0.02} _{-0.03}	0.16 ^{+0.08} _{-0.08}	0.94 ^{+0.04} _{-0.04}	0.89 ^{+0.01} _{-0.01}	9.6 ^{+0.3} _{-0.4}	LAMOST	5448	4.53	0.24

[†] Sources of spectroscopic parameters: HDS — this paper, CKS — Petigura et al. (2017), SPOCS — Brewer et al. (2016), LAMOST — LAMOST DR4 (Wu et al. 2014), APOGEE — Ting et al. (2018), M17 — Mathur et al. (2017).

^b Flagged as photometric binary by Berger et al. (2018).

^{ab} Flagged as AO binary by Berger et al. (2018).

NOTE—The reported values and errors are medians and 15.87th/84.13th percentiles of the marginal posterior.

5. THE PLANET CANDIDATES

Here we model the light curves of 93 candidates that passed the vetting in Section 3. We derive the parameters of the transiting objects including the radius and orbital period based on the stellar parameters determined in Section 4. The results are then used to further filter out potential stellar binaries to obtain the clean sample of planet candidates.

5.1. Modeling of the Light Curves

We used the pre-search data conditioning (PDC) light curves downloaded from the Mikulski Archive for Space Telescopes.⁴ For KIC 6804821 and KIC 10284575, the coherent pulsations were removed as described in Appendix D. For each candidate, we extracted the data within $\max(2\text{days}, W)$ of the detected events (see Figure 1 for the definition of W), and removed 3σ outliers using a median filter. When any other shorter-period

planet in the KOI catalog is transiting inside the extracted time window, that part was removed.

We modeled the light curves of each candidate as the sum of the mean model and the noise. The mean model \mathbf{m} is a product of the transit model assuming a quadratic limb-darkening law (Mandel & Agol 2002) computed with `batman` (Kreidberg 2015) and a second-order polynomial function of time to account for the longer-term trend. The noise was modeled as a Gaussian process whose covariance K consists of a Matérn-3/2 covariance and a white-noise term. The log-likelihood of the model $\ln \mathcal{L}$,

$$\ln \mathcal{L} = -\frac{1}{2}(\mathbf{f} - \mathbf{m})^T K^{-1}(\mathbf{f} - \mathbf{m}) - \frac{1}{2} \ln \det K, \quad (10)$$

was computed using `celerite` (Foreman-Mackey et al. 2017). Here \mathbf{f} represents the observed PDC flux values and the covariance matrix K is given by

$$K_{ij} = (\sigma_i^2 + \sigma_{\text{jit}}^2)\delta_{ij} + \alpha^2 \left(1 + \frac{|t_i - t_j|}{3\rho}\right) \exp\left(-\frac{|t_i - t_j|}{3\rho}\right), \quad (11)$$

where δ_{ij} is the Kronecker delta, σ_i is the PDC error of the i th measurement, and σ_{jit} models an additional

⁴ <https://archive.stsci.edu>

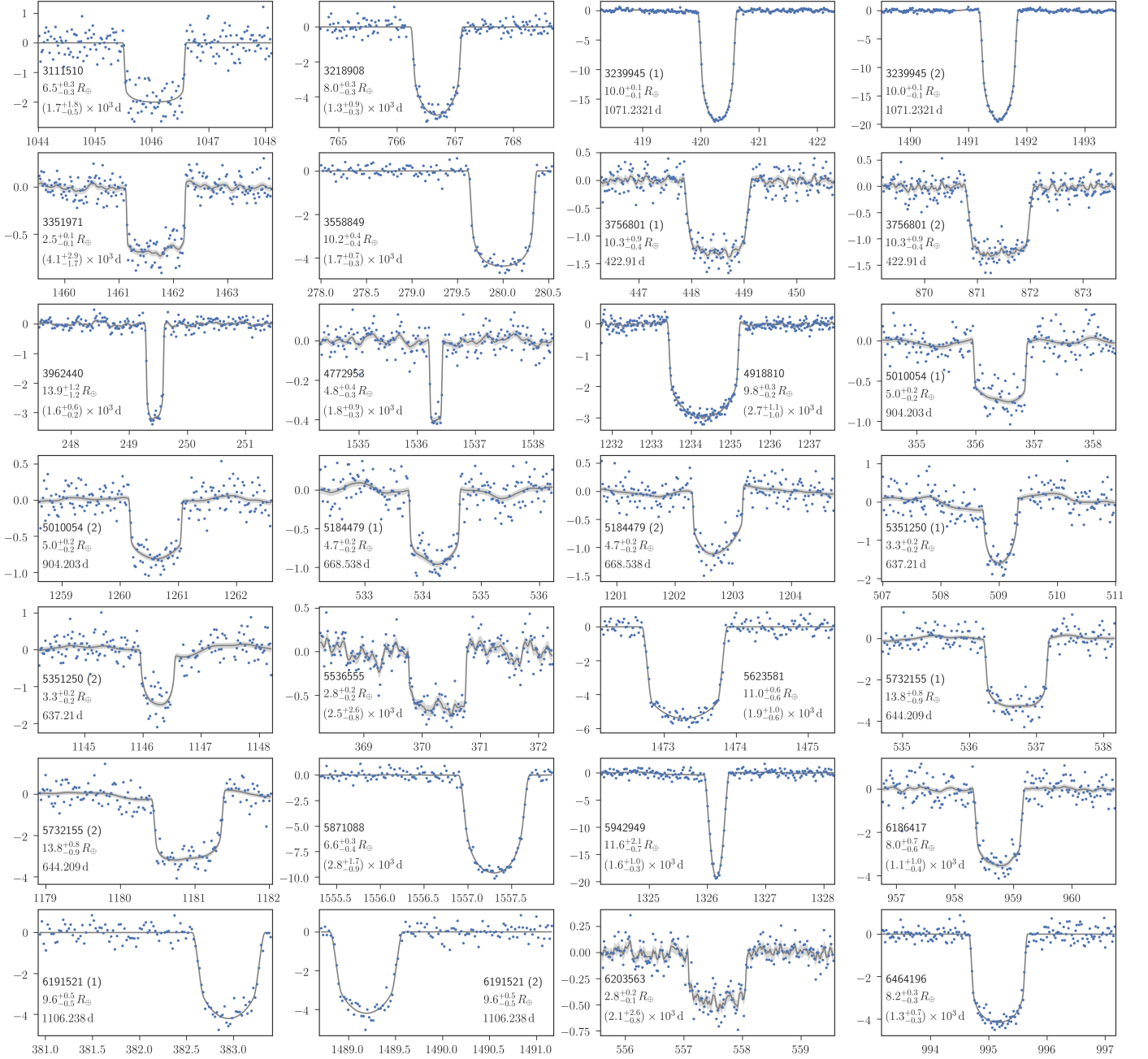


Figure 13. Transit light curves of the candidates in the clean sample (1/4). The vertical axis shows the relative flux deviation from unity, in units of 10^{-3} . The horizontal axis shows the time BJD_{TDB} - 2454833. The blue dots are the PDC data, the gray solid line shows the maximum a posteriori model, and the gray shaded region shows the 1σ prediction. The best-fit polynomial trend (see Section 5.1) is removed here. When two transits are observed, the transit number is shown in the parentheses following the KIC names; here “3” means that there is a gap in the middle of the two observed transits and that the second observed transit was assumed to be the third one. Shown below the KIC names are the radius and period estimated from the light curve modeling.

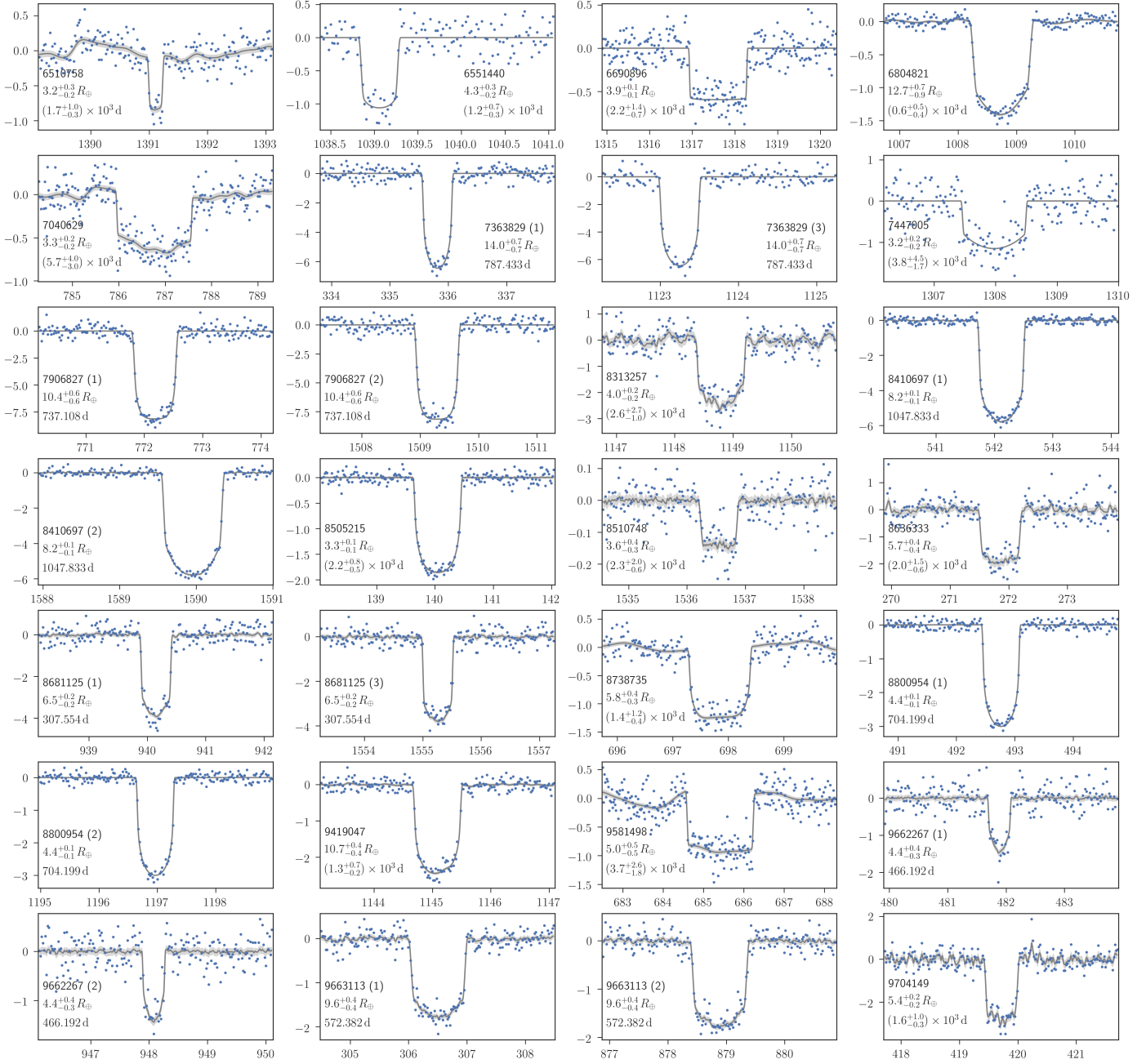


Figure 14. Transit light curves of the candidates in the clean sample (2/4). Same as Figure 13.

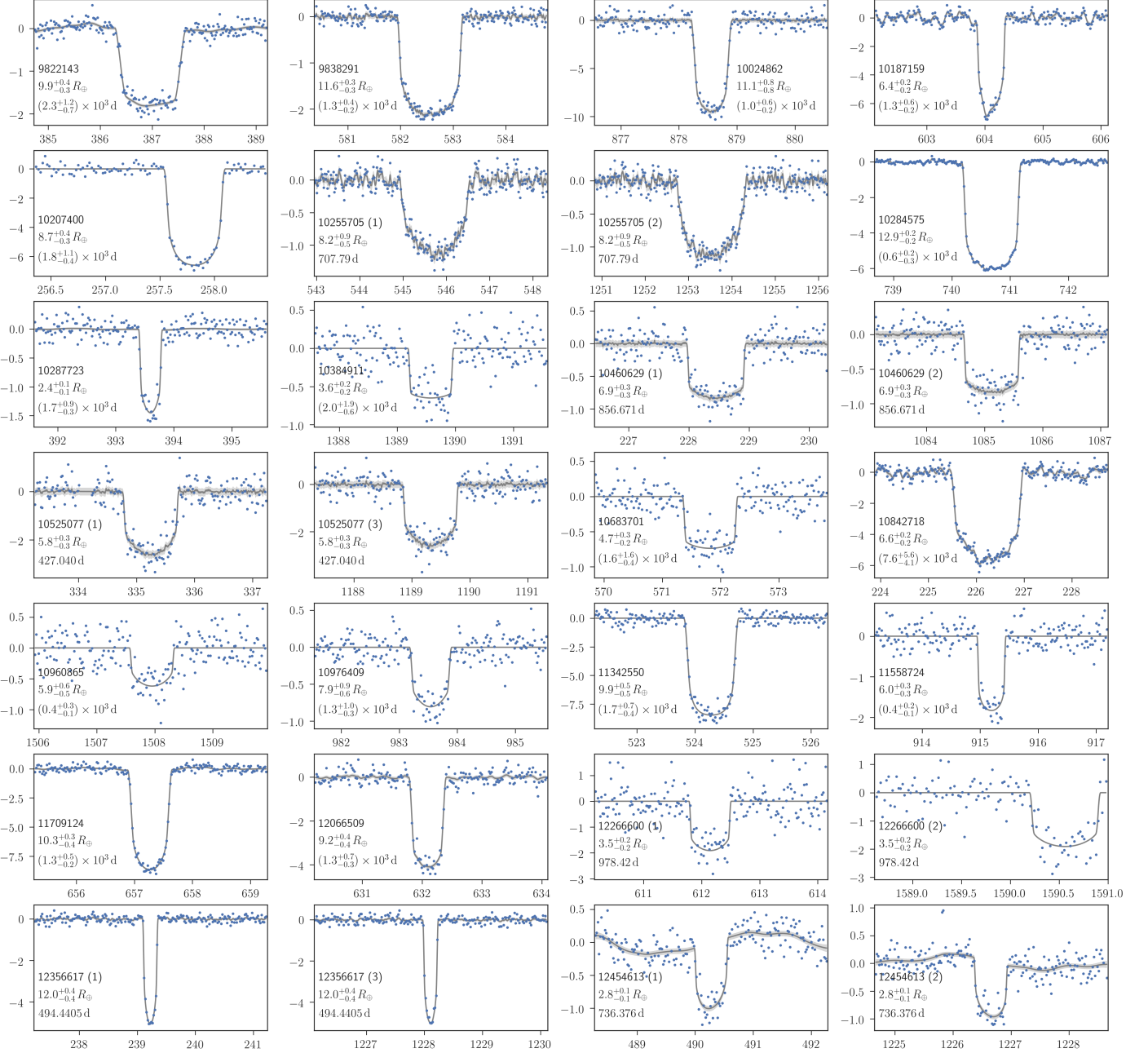


Figure 15. Transit light curves of the candidates in the clean sample (3/4). Same as Figure 13.

white noise component that is not taken into account in σ_i .

The mean transit model has the following parameters: limb-darkening coefficients q_1 and q_2 as parametrized in [Kipping \(2013a\)](#), logarithm of planet-to-star radius ratio $\ln(r/R_*)$, logarithm of mean stellar density $\ln \rho_*$, transit impact parameter b , time of inferior conjunction t_0 , logarithm of orbital period $\ln P$, eccentricity and argument of periastron $\sqrt{e} \cos \omega$ and $\sqrt{e} \sin \omega$, and the coefficients for the polynomial.

We adopted uniform priors for the above parameters, except for the eccentricity (for which we adopted the beta distribution prior with $a = 1.12$ and $b = 3.09$; [Kipping 2013b](#)), mean stellar density (for which we adopted a Gaussian prior based on the constraint in Section 4), and log orbital period (for which we adopted $-2 \ln P/3$ so that the prior on P is $\propto P^{-5/3}$).⁵ When only one

⁵ The choice of $P^{-5/3}$ is motivated by the transit probability $\propto P^{-2/3}$ and the probability for a transit to occur within a finite baseline $\propto P^{-1}$ (cf. [Kipping 2018](#)). So this analysis assumes the

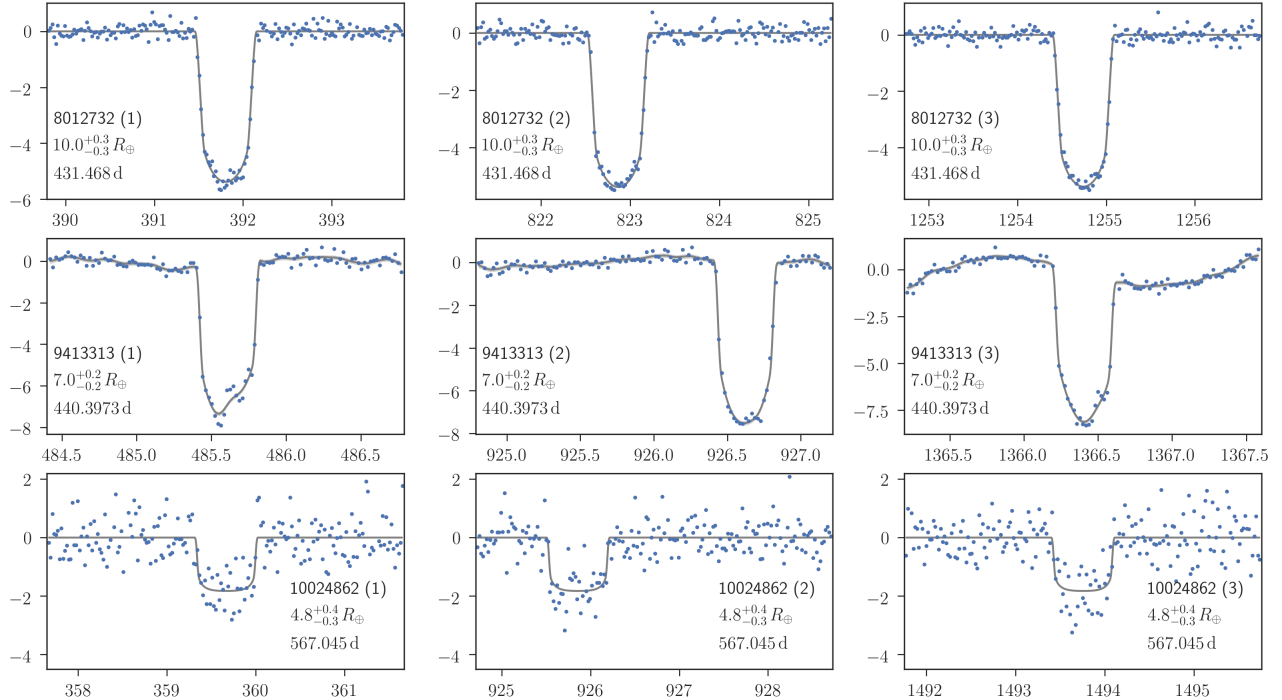


Figure 16. Transit light curves of the candidates in the clean sample (4/4). Same as Figure 13, but here the candidates with three transits are shown. The second transits are all shifted from the center of the panels because of transit timing variations. The light curves of KIC 9413313 exhibits signatures of spot-induced modulations and spot crossing.

transit is observed, the lower and upper bounds for the log period were set to be $\ln P_{\min}$ and $\ln(30000 \text{ days})$, respectively, where P_{\min} is the longer time interval between the observed event time and the two edges of the data. When two transits are observed, the limit was chosen to be ± 0.5 days from the interval of the two transits, and we also fit additional three polynomial coefficients for the second event. If the data in the middle of the two transits are missing, we assumed that the true period is half the interval, because that case is a priori more likely. For TTEs, we fit yet another three polynomial coefficients, and floated the central time of the second transit to take into account transit timing variations, which turned out to be significant for all the TTEs analyzed here. The orbital period in this case corresponds to half the interval between the first and third observed transits.

The posterior samples for the transit and noise parameters ($\ln \alpha$, $\ln \rho$, $\ln \sigma_{\text{jit}}$) were obtained simultaneously using a Markov chain Monte Carlo algorithm, as implemented in `emcee` (Foreman-Mackey et al. 2013). The resulting constraints are summarized in Tables 3 and 5 separately for the clean and flagged candidates (see Section 5.2), respectively. We use the median and

intrinsic prior uniform in P , and is not conditioned on the information that some of the candidates have inner transiting planets.

15.87th/84.13th percentiles of marginal posteriors as the summary. The light curves and the models are shown in Figures 13–16 (for the clean sample) and Figures 24–25 (for the flagged targets), after removing the polynomial trends.

In this analysis, we excluded STEs in KIC 2158850 and 6145201 and the second of the DTEs in KIC 8636333, based on the comparison of the models with and without a transit. For all the candidate events, we computed the Bayesian information criterion (BIC)

$$\text{BIC} = -2 \ln \mathcal{L}_{\max} + k \ln N, \quad (12)$$

where k and N are the numbers of free parameters and data points, respectively, for the maximum likelihood models with and without a transit. We found that the polynomial model has smaller BIC values than the transit model for the above three events, and so they were excluded as insignificant events.

5.2. Pruning the Sample

The combination of the stellar radius derived in Section 4 and the modeling above revealed some candidates whose inferred radii are too large to be planets; these are obvious stellar binaries. In addition, our sample may be contaminated by secondary eclipses with depths similar to that of a planetary transit. Here we flag these events to obtain the cleaner sample of planet candidates, as

described below in detail. The discussion in Section 6 focuses only on this sample (Table 3), although the parameters of the flagged systems are also reported in the catalog (Table 5).

To flag secondary eclipses with depths similar to that of a planetary transit, we use the relation between the ingress/egress duration and eclipse depth. Considering that the luminosity L_\star of main-sequence stars roughly scales as $L_\star \sim R_\star^4$, the secondary eclipses with depths 0.01–1% roughly correspond to binaries with radius ratios of 0.1–0.3. These ratios are larger than the corresponding radius ratios in the transit case (0.01–0.1), and so these events would have longer ingress/egress than expected for a planetary transit. We pick up such events as follows:

1. We fit the light curves of each system using a model for secondary eclipses, where the limb-darkening coefficients are set to be zero and the depth δ_{sec} is an additional free parameter. We also fixed the impact parameter to be zero to obtain an upper limit on the radius ratio allowed from ingress/egress duration, r_{sec} . We then computed the BIC difference from the transit model, $\Delta\text{BIC}_{\text{sec}}$, for the maximum likelihood model. We picked up “flat-bottomed” events as those with $\Delta\text{BIC}_{\text{sec}} < -6$.
2. A part of the “flat-bottomed” events thus selected showed a distinct clustering in the $\delta_{\text{sec}}-r_{\text{sec}}$ plane (Figure 17, upper panel). We removed all the events with $\delta_{\text{sec}} > r_{\text{sec}}^4/(1 + r_{\text{sec}}^4)$ in the lower right region. Because r_{sec} is an upper limit on the secondary radius, this is a conservative thresholding, and the other events are consistent with the planetary transit. As exceptions, we did not flag the candidates with inner confirmed KOIs (KIC 5351250, KOI-408, Kepler-150; Schmitt et al. 2017) or with inner candidate KOIs with false-positive probabilities less than 10% (KIC 5942949, KOI-2525), because these events in multis are less likely to be false positives (Lissauer et al. 2012).

This cut removed 15 systems. As shown in the bottom panel of Figure 17, the cut turned out to be almost equivalent to excluding candidates with both large radii and impact parameters. This feature is consistent with what we expect for stellar eclipses.

As the second cut, we removed additional eight systems whose inferred radii based on the transit model exceed $20 R_\oplus$, but whose light curves were not considered to be flat-bottomed in the first cut. These two cuts leaves us with 67 “clean” candidates in Table 3. Although the second cut on the radius is not so strict, other

large candidates have already been removed in the first cut, and the largest object remaining in the clean sample has $r \approx 14 R_\oplus \approx 1.25 R_{\text{Jup}}$. This value agrees well with the maximum radius of known planets with insolation flux lower than $10^7 \text{ erg cm}^{-2} \text{ s}^{-1}$ and radii measured to better than 10%.

The light curves of KIC 3526901, 4042088, 4754460, and 7947784 exhibit deeper, stellar eclipses in addition to the STEs in the input catalog, suggesting that the latter events are secondary eclipses. All of these systems, which are shown with star symbols in Figure 17, have been successfully removed from the clean sample by the above criteria.

5.2.1. How Clean is the Clean Sample?

Our precise stellar radii allowed us to remove stellar eclipses caused by objects $> 20 R_\oplus$ reliably. We also attempted to flag possible secondary eclipses that produce shallower eclipses. Are the remaining candidates all likely to be planets?

First we examine the number of events flagged as potential secondary eclipses above. Considering that $L_\star \sim M_\star^4$ for main-sequence stars, companions with mass ratios $q \sim 0.1-0.3$ can produce secondary eclipses with 0.01–1%. Assuming the log-normal period distribution in Raghavan et al. (2010), binary fraction of 0.5, and $1.3 R_\star$ primary (median of KIC stars), EB occurrence in our search range is $\approx 2 \times 10^{-4}$. Thus the expected number of EBs with mass ratio < 0.3 in the whole *Kepler* sample would be $\sim 2 \times 10^{-4} \times 0.3 \times 2 \times 10^5 \sim 10$ assuming flat mass-ratio distribution. This is comparable to the number of objects (15) flagged as potential secondary eclipses, serving as a sanity check of our procedure.

Primary eclipses due to companions later than M7 ($\lesssim 0.1 M_\odot$) or brown-dwarfs can also be confused as Jupiter-sized planets, and they are basically indistinguishable based on the light curve alone. However, binaries with corresponding mass ratios ($\lesssim 0.1$) or brown dwarfs (Grether & Lineweaver 2006) are even rarer than the above estimate. Thus the contaminations from these objects are likely $\mathcal{O}(1)$, if any.

Another potential source of confusion is a secondary eclipse of a WD companion. Although the host stars in our sample are typically older than a few Gyr, some WD companions, if any, may still have luminosities of $\sim 10^{-3} L_\odot$ and contaminate our sample. Since their physical radii are small, these cases should be at the leftward of the transit line in the upper panel of Figure 17. Murphy et al. (2018) estimated the occurrence of WD companions around A/F dwarfs to be $\sim 3\%$ for the relevant period range, which is about one fourth of the occurrence of main-sequence companions estimated above.

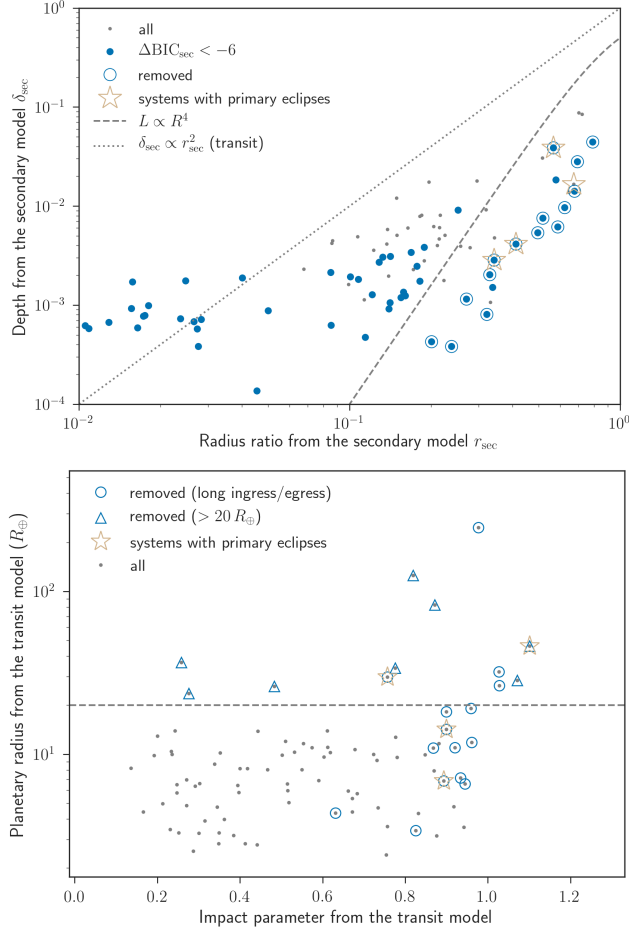


Figure 17. Two cuts to flag potential stellar binaries; see Section 5.2 for details. *Upper panel* — The depth δ_{sec} and radius ratio r_{sec} from the secondary eclipse model. The gray dots show all the candidates and blue filled circles are the ones with $\Delta\text{BIC}_{\text{sec}} < -6$ (i.e. secondary model is at least as good as the transit model). The dashed line is the $\delta_{\text{sec}}-r_{\text{sec}}$ relation assuming $L_{\star} \sim R_{\star}^4$. The dotted line corresponds to $\delta_{\text{sec}} = r_{\text{sec}}^2$, which is expected for the transit case. The flagged systems are shown with outer circles, and the candidates with additional primary eclipses are marked by star symbols. *Bottom panel* — Planetary radii and impact parameters based on the transit model and stellar radii derived in Section 4. The meaning of the gray dots, blue open circles, and stars are the same as in the upper panel. The triangles show the candidates that were not flagged in the upper panel but have radii greater than $20 R_{\oplus}$ (i.e. stellar size).

Thus, considering the luminosity function of WDs, some objects in the leftmost part of the upper panel of Figure 17 may be WDs. The objects in this area are marked with squares in Table 3, although they were not removed from the clean sample.

In summary, it is difficult to completely rule out planetary-depth eclipses caused by red-dwarf/WD companions, but we argue that their contamination is at most $\sim 10\%$ in the clean sample.

Table 3. Parameters of the Systems in the Clean Sample.

KIC	KOI	Kp	$M_{\star} (M_{\odot})$	$R_{\star} (R_{\odot})$	$r (R_{\oplus})$	t_0 (BKJD)	P (days)	b	e
3111510	...	14.8	$1.19^{+0.08}_{-0.08}$	$1.36^{+0.06}_{-0.05}$	$6.5^{+0.3}_{-0.3}$	$1046.048^{+0.006}_{-0.005}$	$(1.7^{+1.8}_{-0.5}) \times 10^3$	$0.4^{+0.3}_{-0.3}$	$0.2^{+0.2}_{-0.1}$

Table 3 continued

Table 3 (continued)

KIC	KOI	Kp	$M_\star (M_\odot)$	$R_\star (R_\odot)$	$r (R_\oplus)$	t_0 (BKJD)	P (days)	b	e
3218908 ^{†b}	1108 (770)	14.6	0.96 ^{+0.04} _{-0.03}	1.13 ^{+0.03} _{-0.03}	8.0 ^{+0.3} _{-0.3}	766.683 ^{+0.003} _{-0.003}	$(1.3^{+0.9}) \times 10^3$	0.5 ^{+0.1} _{-0.3}	0.1 ^{+0.2} _{-0.1}
3239945 [†]	490 (167)	14.0	0.78 ^{+0.03} _{-0.03}	0.745 ^{+0.008} _{-0.008}	10.0 ^{+0.1} _{-0.1}	420.2869 ^{+0.0007} _{-0.0007}	1071.2321 ^{+0.0010} _{-0.0009}	0.24 ^{+0.06} _{-0.09}	0.06 ^{+0.13} _{-0.04}
3351971 [□]	...	12.7	0.92 ^{+0.05} _{-0.06}	0.90 ^{+0.02} _{-0.02}	2.55 ^{+0.10} _{-0.08}	1461.676 ^{+0.003} _{-0.004}	$(4^{+3}) \times 10^3$	0.3 ^{+0.2} _{-0.2}	0.2 ^{+0.2} _{-0.1}
3558849 [†]	4307	14.2	1.14 ^{+0.05} _{-0.04}	1.51 ^{+0.05} _{-0.04}	10.2 ^{+0.4} _{-0.4}	279.994 ^{+0.002} _{-0.002}	$(1.7^{+0.7}) \times 10^3$	0.4 ^{+0.2} _{-0.2}	0.54 ^{+0.09} _{-0.08}
3756801 [†]	1206*	13.6	1.3 ^{+0.2} _{-0.1}	2.77 ^{+0.08} _{-0.08}	10.3 ^{+0.9} _{-0.4}	448.495 ^{+0.007} _{-0.007}	422.91 ^{+0.01} _{-0.01}	0.5 ^{+0.3} _{-0.3}	0.2 ^{+0.2} _{-0.1}
3962440 [†]	1208*	13.6	1.55 ^{+0.07} _{-0.07}	2.3 ^{+0.2} _{-0.2}	14 ⁺¹ ₋₁	249.442 ^{+0.001} _{-0.002}	$(1.6^{+0.6}) \times 10^3$	0.6 ^{+0.1} _{-0.2}	0.92 ^{+0.02} _{-0.03}
4772953	...	11.5	2.2 ^{+0.1} _{-0.1}	2.04 ^{+0.10} _{-0.09}	4.8 ^{+0.4} _{-0.3}	1536.321 ^{+0.003} _{-0.003}	$(1.8^{+0.9}) \times 10^3$	0.92 ^{+0.03} _{-0.06}	0.79 ^{+0.08} _{-0.10}
4918810 [†]	...	13.4	1.31 ^{+0.03} _{-0.07}	1.78 ^{+0.04} _{-0.03}	9.8 ^{+0.3} _{-0.2}	1234.314 ^{+0.003} _{-0.003}	$(3^{+1}) \times 10^3$	0.2 ^{+0.1} _{-0.1}	0.2 ^{+0.2} _{-0.1}
5010054 [†]	...	14.0	1.16 ^{+0.03} _{-0.03}	1.72 ^{+0.04} _{-0.04}	5.0 ^{+0.2} _{-0.2}	356.411 ^{+0.006} _{-0.005}	904.203 ^{+0.008} _{-0.009}	0.5 ^{+0.2} _{-0.3}	0.2 ^{+0.1} _{-0.1}
5184479 [†]	...	14.2	1.13 ^{+0.05} _{-0.05}	1.46 ^{+0.04} _{-0.04}	4.7 ^{+0.2} _{-0.2}	534.199 ^{+0.005} _{-0.005}	668.538 ^{+0.008} _{-0.008}	0.3 ^{+0.2} _{-0.2}	0.11 ^{+0.15} _{-0.07}
5351250 [†]	408 (150)	15.0	0.96 ^{+0.03} _{-0.04}	0.89 ^{+0.02} _{-0.02}	3.3 ^{+0.2} _{-0.2}	509.03 ^{+0.01} _{-0.01}	637.21 ^{+0.02} _{-0.02}	0.3 ^{+0.3} _{-0.2}	0.1 ^{+0.2} _{-0.1}
5536555 ^{†□}	...	13.5	1.06 ^{+0.05} _{-0.05}	1.06 ^{+0.02} _{-0.02}	2.8 ^{+0.2} _{-0.2}	370.270 ^{+0.014} _{-0.008}	$(2.5^{+2.6}) \times 10^3$	0.3 ^{+0.3} _{-0.2}	0.2 ^{+0.2} _{-0.1}
5623581	...	15.1	1.21 ^{+0.08} _{-0.10}	1.43 ^{+0.07} _{-0.07}	11.0 ^{+0.6} _{-0.6}	1473.287 ^{+0.003} _{-0.003}	$(1.9^{+1.0}) \times 10^3$	0.57 ^{+0.08} _{-0.17}	0.14 ^{+0.14} _{-0.09}
5732155	...	15.2	1.57 ^{+0.06} _{-0.06}	2.3 ^{+0.1} _{-0.1}	13.8 ^{+0.8} _{-0.9}	536.704 ^{+0.005} _{-0.005}	644.209 ^{+0.008} _{-0.008}	0.4 ^{+0.2} _{-0.3}	0.3 ^{+0.1} _{-0.1}
5871088	...	15.6	0.71 ^{+0.04} _{-0.04}	0.67 ^{+0.03} _{-0.03}	6.6 ^{+0.3} _{-0.4}	1557.302 ^{+0.002} _{-0.002}	$(2.8^{+1.7}) \times 10^3$	0.5 ^{+0.1} _{-0.2}	0.2 ^{+0.1} _{-0.1}
5942949	2525	15.7	0.73 ^{+0.04} _{-0.03}	0.69 ^{+0.02} _{-0.02}	11.6 ^{+2.1} _{-0.7}	1326.160 ^{+0.001} _{-0.001}	$(1.6^{+1.0}) \times 10^3$	0.88 ^{+0.07} _{-0.04}	0.3 ^{+0.2} _{-0.1}
6186417	...	15.4	1.15 ^{+0.08} _{-0.09}	1.31 ^{+0.09} _{-0.07}	8.0 ^{+0.7} _{-0.6}	958.751 ^{+0.006} _{-0.005}	$(1.1^{+1.0}) \times 10^3$	0.5 ^{+0.2} _{-0.3}	0.2 ^{+0.2} _{-0.1}
6191521 [†]	847 (700)	15.2	0.98 ^{+0.04} _{-0.03}	1.34 ^{+0.06} _{-0.06}	9.6 ^{+0.5} _{-0.5}	382.951 ^{+0.004} _{-0.004}	1106.238 ^{+0.006} _{-0.006}	0.78 ^{+0.03} _{-0.04}	0.10 ^{+0.15} _{-0.07}
6203563	...	13.2	1.19 ^{+0.06} _{-0.07}	1.21 ^{+0.03} _{-0.02}	2.8 ^{+0.2} _{-0.1}	557.58 ^{+0.01} _{-0.01}	$(2.1^{+2.6}) \times 10^3$	0.4 ^{+0.3} _{-0.3}	0.2 ^{+0.2} _{-0.1}
6464196 [†]	...	14.5	1.01 ^{+0.04} _{-0.05}	1.24 ^{+0.04} _{-0.03}	8.2 ^{+0.3} _{-0.3}	995.163 ^{+0.003} _{-0.003}	$(1.3^{+0.7}) \times 10^3$	0.4 ^{+0.2} _{-0.2}	0.1 ^{+0.1} _{-0.1}
6510758 ^{†□}	...	13.8	0.91 ^{+0.04} _{-0.02}	0.99 ^{+0.01} _{-0.01}	3.2 ^{+0.3} _{-0.2}	1391.113 ^{+0.005} _{-0.005}	$(1.7^{+1.0}) \times 10^3$	0.88 ^{+0.05} _{-0.09}	0.6 ^{+0.1} _{-0.2}
6551440 [†]	...	13.6	1.02 ^{+0.04} _{-0.04}	1.17 ^{+0.02} _{-0.02}	4.3 ^{+0.3} _{-0.2}	1039.059 ^{+0.005} _{-0.005}	$(1.2^{+0.7}) \times 10^3$	0.83 ^{+0.05} _{-0.11}	0.3 ^{+0.2} _{-0.2}
6690896 ^{†□}	...	13.7	1.01 ^{+0.05} _{-0.04}	1.49 ^{+0.03} _{-0.03}	3.9 ^{+0.1} _{-0.1}	1317.612 ^{+0.007} _{-0.007}	$(2.2^{+1.4}) \times 10^3$	0.3 ^{+0.3} _{-0.2}	0.2 ^{+0.2} _{-0.1}
6804821	...	10.6	2.3 ^{+0.3} _{-0.2}	3.0 ^{+0.1} _{-0.2}	12.7 ^{+0.7} _{-0.9}	1008.747 ^{+0.003} _{-0.004}	$(0.6^{+0.5}) \times 10^3$	0.78 ^{+0.03} _{-0.04}	0.2 ^{+0.3} _{-0.2}
7040629 ^{†□}	671 (208)	13.7	1.11 ^{+0.04} _{-0.04}	1.25 ^{+0.02} _{-0.02}	3.3 ^{+0.2} _{-0.2}	786.763 ^{+0.008} _{-0.007}	$(6^{+4}) \times 10^3$	0.3 ^{+0.2} _{-0.2}	0.2 ^{+0.2} _{-0.1}
7363829 [†]	1356*	15.2	1.15 ^{+0.09} _{-0.05}	1.76 ^{+0.08} _{-0.08}	14.0 ^{+0.7} _{-0.7}	335.817 ^{+0.002} _{-0.002}	787.433 ^{+0.003} _{-0.003}	0.2 ^{+0.2} _{-0.2}	0.68 ^{+0.03} _{-0.04}
7447005 [□]	...	15.1	0.95 ^{+0.06} _{-0.06}	0.95 ^{+0.03} _{-0.03}	3.2 ^{+0.2} _{-0.2}	1307.98 ^{+0.01} _{-0.02}	$(4^{+2}) \times 10^3$	0.4 ^{+0.3} _{-0.3}	0.2 ^{+0.2} _{-0.1}
7906827	...	15.7	1.12 ^{+0.07} _{-0.08}	1.14 ^{+0.06} _{-0.06}	10.4 ^{+0.6} _{-0.6}	772.185 ^{+0.002} _{-0.002}	737.108 ^{+0.003} _{-0.003}	0.2 ^{+0.2} _{-0.2}	0.09 ^{+0.16} _{-0.06}
8012732 [†]	8151 (FP)	13.9	1.05 ^{+0.04} _{-0.04}	1.26 ^{+0.03} _{-0.03}	10.0 ^{+0.3} _{-0.3}	391.807 ^{+0.002} _{-0.002}	431.468 ^{+0.001} _{-0.001}	0.72 ^{+0.02} _{-0.03}	0.24 ^{+0.14} _{-0.06}
8313257	...	15.4	0.84 ^{+0.04} _{-0.04}	0.80 ^{+0.02} _{-0.02}	4.0 ^{+0.2} _{-0.2}	1148.793 ^{+0.008} _{-0.008}	$(3^{+3}) \times 10^3$	0.4 ^{+0.3} _{-0.2}	0.2 ^{+0.2} _{-0.1}
8410697 [†]	...	13.4	0.93 ^{+0.04} _{-0.04}	1.08 ^{+0.01} _{-0.01}	8.2 ^{+0.1} _{-0.1}	542.123 ^{+0.001} _{-0.001}	1047.833 ^{+0.002} _{-0.002}	0.14 ^{+0.12} _{-0.09}	0.12 ^{+0.09} _{-0.04}
8505215 ^{†ab}	99	13.0	0.75 ^{+0.02} _{-0.01}	0.775 ^{+0.007} _{-0.007}	3.28 ^{+0.09} _{-0.06}	140.049 ^{+0.002} _{-0.002}	$(2.2^{+0.8}) \times 10^3$	0.3 ^{+0.2} _{-0.2}	0.11 ^{+0.12} _{-0.08}
8510748 [†]	...	11.6	1.66 ^{+0.04} _{-0.04}	2.48 ^{+0.10} _{-0.09}	3.6 ^{+0.4} _{-0.3}	1536.55 ^{+0.01} _{-0.01}	$(2.3^{+2.0}) \times 10^3$	0.94 ^{+0.02} _{-0.04}	0.2 ^{+0.3} _{-0.2}
8636333 [□]	3349 (1475)	15.3	1.13 ^{+0.08} _{-0.08}	1.19 ^{+0.06} _{-0.05}	5.7 ^{+0.4} _{-0.4}	271.87 ^{+0.01} _{-0.01}	$(2.0^{+1.5}) \times 10^3$	0.7 ^{+0.1} _{-0.4}	0.3 ^{+0.2} _{-0.2}
8681125 [†]	...	15.0	0.93 ^{+0.04} _{-0.02}	1.04 ^{+0.03} _{-0.03}	6.5 ^{+0.2} _{-0.2}	940.149 ^{+0.003} _{-0.003}	307.554 ^{+0.002} _{-0.002}	0.2 ^{+0.2} _{-0.2}	0.10 ^{+0.16} _{-0.06}
8738735 [†]	693 (214)	13.9	1.19 ^{+0.06} _{-0.04}	1.61 ^{+0.04} _{-0.04}	5.8 ^{+0.4} _{-0.3}	697.856 ^{+0.006} _{-0.006}	$(1.4^{+1.2}) \times 10^3$	0.4 ^{+0.3} _{-0.3}	0.2 ^{+0.2} _{-0.1}
8800954 ^{†ab}	1274 (421)*	13.4	0.82 ^{+0.04} _{-0.03}	0.82 ^{+0.01} _{-0.01}	4.42 ^{+0.08} _{-0.07}	492.767 ^{+0.001} _{-0.001}	704.199 ^{+0.002} _{-0.002}	0.2 ^{+0.2} _{-0.1}	0.13 ^{+0.13} _{-0.07}
9413313 [†]	...	14.1	0.86 ^{+0.04} _{-0.03}	0.82 ^{+0.01} _{-0.01}	7.0 ^{+0.2} _{-0.2}	485.611 ^{+0.001} _{-0.001}	440.3973 ^{+0.0008} _{-0.0008}	0.3 ^{+0.2} _{-0.2}	0.25 ^{+0.07} _{-0.07}
9419047 [†]	...	13.6	1.27 ^{+0.05} _{-0.05}	2.05 ^{+0.04} _{-0.04}	10.7 ^{+0.4} _{-0.4}	1145.086 ^{+0.003} _{-0.004}	$(1.3^{+0.7}) \times 10^3$	0.68 ^{+0.09} _{-0.12}	0.4 ^{+0.1} _{-0.1}
9581498 [□]	7194 (FP)	14.2	1.20 ^{+0.08} _{-0.11}	1.4 ^{+0.1} _{-0.1}	5.0 ^{+0.5} _{-0.5}	685.417 ^{+0.005} _{-0.005}	$(4^{+3}) \times 10^3$	0.2 ^{+0.2} _{-0.1}	0.2 ^{+0.2} _{-0.1}
9662267 [†]	...	14.9	0.99 ^{+0.04} _{-0.04}	1.13 ^{+0.03} _{-0.03}	4.4 ^{+0.4} _{-0.3}	481.886 ^{+0.006} _{-0.006}	466.192 ^{+0.007} _{-0.008}	0.7 ^{+0.1} _{-0.4}	0.3 ^{+0.2} _{-0.2}

Table 3 continued

Table 3 (continued)

KIC	KOI	Kp	$M_\star (M_\odot)$	$R_\star (R_\odot)$	$r (R_\oplus)$	t_0 (BKJD)	P (days)	b	e
9663113 [†]	179 (458)	14.0	$1.51^{+0.04}_{-0.04}$	$2.20^{+0.07}_{-0.07}$	$9.6^{+0.4}_{-0.4}$	$306.507^{+0.004}_{-0.004}$	$572.382^{+0.006}_{-0.006}$	$0.60^{+0.08}_{-0.15}$	$0.1^{+0.2}_{-0.1}$
9704149	...	15.1	$0.96^{+0.06}_{-0.07}$	$0.94^{+0.03}_{-0.03}$	$5.4^{+0.2}_{-0.2}$	$419.720^{+0.004}_{-0.004}$	$(1.6^{+1.0}_{-0.3}) \times 10^3$	$0.67^{+0.09}_{-0.16}$	$0.2^{+0.2}_{-0.2}$
9822143 [†]	...	13.8	$0.91^{+0.04}_{-0.03}$	$2.10^{+0.04}_{-0.04}$	$9.9^{+0.4}_{-0.3}$	$386.963^{+0.005}_{-0.005}$	$(2.3^{+1.2}_{-0.7}) \times 10^3$	$0.85^{+0.02}_{-0.02}$	$0.2^{+0.2}_{-0.1}$
9838291 [†]	...	12.9	$1.51^{+0.04}_{-0.04}$	$2.45^{+0.06}_{-0.05}$	$11.6^{+0.3}_{-0.3}$	$582.562^{+0.002}_{-0.002}$	$(1.3^{+0.4}_{-0.2}) \times 10^3$	$0.55^{+0.08}_{-0.12}$	$0.3^{+0.1}_{-0.1}$
10024862 [†]	...	15.9	$1.04^{+0.05}_{-0.05}$	$1.09^{+0.07}_{-0.07}$	$11.1^{+0.8}_{-0.8}$	$878.561^{+0.003}_{-0.003}$	$(1.0^{+0.6}_{-0.2}) \times 10^3$	$0.61^{+0.08}_{-0.12}$	$0.2^{+0.2}_{-0.1}$
10187159 [†]	1870 (989)	14.4	$0.82^{+0.04}_{-0.03}$	$0.80^{+0.01}_{-0.01}$	$6.4^{+0.2}_{-0.2}$	$604.108^{+0.002}_{-0.002}$	$(1.3^{+0.6}_{-0.2}) \times 10^3$	$0.3^{+0.2}_{-0.2}$	$0.4^{+0.1}_{-0.1}$
10207400 [†]	...	15.0	$0.97^{+0.05}_{-0.04}$	$1.07^{+0.04}_{-0.03}$	$8.7^{+0.4}_{-0.3}$	$257.817^{+0.001}_{-0.001}$	$(1.8^{+1.1}_{-0.4}) \times 10^3$	$0.3^{+0.2}_{-0.2}$	$0.56^{+0.09}_{-0.08}$
10255705 [†]	...	12.9	$1.11^{+0.16}_{-0.06}$	$2.5^{+0.1}_{-0.1}$	$8.2^{+0.9}_{-0.5}$	$545.736^{+0.009}_{-0.008}$	$707.79^{+0.01}_{-0.01}$	$0.4^{+0.3}_{-0.2}$	$0.2^{+0.2}_{-0.1}$
10284575 [†]	3210 (FP)	11.9	$1.35^{+0.03}_{-0.03}$	$1.63^{+0.03}_{-0.03}$	$12.9^{+0.2}_{-0.2}$	$740.6801^{+0.0007}_{-0.0007}$	$(0.6^{+0.2}_{-0.3}) \times 10^3$	$0.2^{+0.1}_{-0.1}$	$0.2^{+0.2}_{-0.1}$
10287723 [†]	1174*	13.4	$0.59^{+0.02}_{-0.01}$	$0.582^{+0.006}_{-0.006}$	$2.4^{+0.1}_{-0.1}$	$393.598^{+0.003}_{-0.003}$	$(1.7^{+0.9}_{-0.3}) \times 10^3$	$0.75^{+0.07}_{-0.13}$	$0.2^{+0.2}_{-0.2}$
10384911 [†]	...	14.0	$0.98^{+0.05}_{-0.05}$	$1.31^{+0.03}_{-0.03}$	$3.6^{+0.2}_{-0.2}$	$1389.577^{+0.010}_{-0.009}$	$(2.0^{+1.9}_{-0.6}) \times 10^3$	$0.8^{+0.1}_{-0.3}$	$0.3^{+0.2}_{-0.2}$
10460629 [□]	1168*	14.0	$1.49^{+0.03}_{-0.04}$	$2.26^{+0.06}_{-0.06}$	$6.9^{+0.3}_{-0.3}$	$228.454^{+0.006}_{-0.006}$	$856.671^{+0.008}_{-0.009}$	$0.6^{+0.1}_{-0.2}$	$0.3^{+0.1}_{-0.2}$
10525077	5800	15.4	$1.11^{+0.07}_{-0.09}$	$1.15^{+0.05}_{-0.04}$	$5.8^{+0.3}_{-0.3}$	$335.240^{+0.007}_{-0.008}$	$427.040^{+0.005}_{-0.004}$	$0.2^{+0.2}_{-0.2}$	$0.46^{+0.14}_{-0.09}$
10683701 [†]	...	13.7	$0.90^{+0.03}_{-0.02}$	$1.61^{+0.03}_{-0.03}$	$4.7^{+0.3}_{-0.2}$	$571.824^{+0.008}_{-0.007}$	$(1.6^{+1.6}_{-0.4}) \times 10^3$	$0.7^{+0.1}_{-0.3}$	$0.3^{+0.2}_{-0.2}$
10842718 [†]	...	14.6	$0.90^{+0.04}_{-0.04}$	$0.89^{+0.02}_{-0.02}$	$6.6^{+0.2}_{-0.2}$	$226.231^{+0.005}_{-0.005}$	$(8^{+6}_{-4}) \times 10^3$	$0.3^{+0.2}_{-0.2}$	$0.2^{+0.2}_{-0.2}$
10960865 [†]	...	14.2	$1.22^{+0.07}_{-0.05}$	$2.30^{+0.06}_{-0.06}$	$5.9^{+0.6}_{-0.5}$	$1507.95^{+0.02}_{-0.02}$	$(0.35^{+0.29}_{-0.09}) \times 10^3$	$0.7^{+0.2}_{-0.4}$	$0.3^{+0.2}_{-0.2}$
10976409 [□]	...	13.9	$1.66^{+0.04}_{-0.04}$	$2.33^{+0.08}_{-0.08}$	$7.9^{+0.9}_{-0.6}$	$983.539^{+0.008}_{-0.008}$	$(1.3^{+1.0}_{-0.3}) \times 10^3$	$0.87^{+0.05}_{-0.08}$	$0.3^{+0.2}_{-0.2}$
11342550 [†]	1421*	15.3	$0.95^{+0.04}_{-0.04}$	$1.04^{+0.04}_{-0.04}$	$9.9^{+0.5}_{-0.5}$	$524.281^{+0.002}_{-0.002}$	$(1.7^{+0.7}_{-0.4}) \times 10^3$	$0.5^{+0.1}_{-0.2}$	$0.12^{+0.13}_{-0.08}$
11558724 [□]	...	14.7	$1.14^{+0.04}_{-0.04}$	$1.34^{+0.04}_{-0.04}$	$6.0^{+0.3}_{-0.3}$	$915.196^{+0.003}_{-0.003}$	$(0.37^{+0.22}_{-0.08}) \times 10^3$	$0.5^{+0.2}_{-0.3}$	$0.3^{+0.2}_{-0.2}$
11709124 [†]	435 (154)	14.5	$0.96^{+0.04}_{-0.04}$	$1.07^{+0.03}_{-0.03}$	$10.3^{+0.3}_{-0.4}$	$657.268^{+0.001}_{-0.001}$	$(1.3^{+0.5}_{-0.2}) \times 10^3$	$0.62^{+0.04}_{-0.07}$	$0.2^{+0.2}_{-0.1}$
12066509 [†]	...	14.7	$1.06^{+0.05}_{-0.04}$	$1.33^{+0.05}_{-0.05}$	$9.2^{+0.4}_{-0.4}$	$632.092^{+0.002}_{-0.003}$	$(1.3^{+0.7}_{-0.3}) \times 10^3$	$0.73^{+0.06}_{-0.09}$	$0.4^{+0.2}_{-0.1}$
12266600 [□]	...	15.4	$0.83^{+0.04}_{-0.04}$	$0.78^{+0.02}_{-0.02}$	$3.5^{+0.2}_{-0.2}$	$612.145^{+0.008}_{-0.009}$	$978.42^{+0.01}_{-0.01}$	$0.2^{+0.2}_{-0.2}$	$0.20^{+0.17}_{-0.09}$
12356617 [†]	375*	13.3	$1.15^{+0.09}_{-0.04}$	$1.66^{+0.03}_{-0.03}$	$12.0^{+0.4}_{-0.4}$	$239.2243^{+0.0007}_{-0.0007}$	$494.4405^{+0.0005}_{-0.0005}$	$0.5^{+0.1}_{-0.2}$	$0.85^{+0.02}_{-0.02}$
12454613 [†]	...	13.5	$0.94^{+0.04}_{-0.04}$	$0.89^{+0.01}_{-0.01}$	$2.8^{+0.1}_{-0.1}$	$490.272^{+0.007}_{-0.007}$	$736.376^{+0.008}_{-0.009}$	$0.4^{+0.2}_{-0.3}$	$0.2^{+0.2}_{-0.1}$
10024862 [†]	...	15.9	$1.04^{+0.05}_{-0.05}$	$1.09^{+0.07}_{-0.07}$	$4.8^{+0.4}_{-0.3}$	$359.67^{+0.01}_{-0.01}$	$567.045^{+0.007}_{-0.008}$	$0.3^{+0.2}_{-0.2}$	$0.13^{+0.21}_{-0.09}$

(triple)

*These stars have KOI numbers because of the STEs/DTEs analyzed here; they are the only transiting planet candidates.

[†] Stars with spectra.[□] Flat-bottomed transits with short ingress/egress; see Section 5.2.^b Flagged as photometric binary by Berger et al. (2018).^{ab} Flagged as AO binary by Berger et al. (2018).

NOTE—The reported values and errors are medians and 15.87th/84.13th percentiles of the marginal posterior.

6. PROPERTIES OF THE CLEAN SAMPLE

Figure 18 shows our clean sample in the radius–period plane, along with the “clean KOI” sample constructed from confirmed planets and planet candidates with false positive probabilities calculated by Morton et al. (2016) less than 10%. For those without calculated values in Morton et al. (2016), we adopted the values in the table

available at the NASA exoplanet archive.⁶ The current KOI catalog includes some of the STEs/DTEs in our clean sample, and they were excluded to avoid overlap. We updated the planetary radii in this clean KOI sample using the revised stellar radii in Berger et al. (2018).

⁶ <https://exoplanetarchive.ipac.caltech.edu/cgi-bin/TblView/nph-tblView?app=ExoTbls&config=koifpp>

Among the 67 candidates in our clean sample, 23 are newly reported in this paper (cf. Table 1).⁷ In terms of planet size, 29 have $r > 8R_{\oplus}$, 23 have $4R_{\oplus} < r < 8R_{\oplus}$, and 15 have $r < 4R_{\oplus}$. The number of Jupiter-sized planets with $r > 8R_{\oplus}$ is found to be consistent with the Doppler occurrence (see Section 6.1). This implies that the catalog may have a high completeness for Jupiter-sized planets, although the result does not rule out the possibility that the occurrences of giant planets in the two samples are intrinsically different. Although we have not yet quantified the search completeness, we found a similar number of smaller planets, suggesting that they are at least as common as Jupiter-sized ones in the searched period range over 2–20 yr. If the sample is complete, our sample implies the occurrence of ≈ 0.4 planets larger than Neptune per FKG star (Section 6.4). The radius distribution of planets $> 4R_{\oplus}$ turned out to be indistinguishable from that of the KOIs with 100 days $\lesssim P \lesssim 700$ days (Section 6.2). We also found, based on the spectroscopic sample, that the host stars of the planets larger than $4R_{\oplus}$ have systematically higher [Fe/H] than the other *Kepler* field stars, while this is not the case for smaller candidates (Section 6.3).

6.1. Comparison with the Doppler Sample

Jupiter-sized planets in the period range of our interest have already been detected in long-term Doppler surveys (e.g. Cumming et al. 2008; Mayor et al. 2011). Here we compare the number of Jupiter-sized planets in our sample against the number expected from the Doppler occurrence.

We use the occurrence rate density modeled as a double power-law function of orbital period and planetary mass by Fernandes et al. (2018), based on the combined sample of HARPS and CORALIE surveys (Mayor et al. 2011). Specifically, we reproduced the analysis in Fernandes et al. (2018) for periods 3–10,000 days and mass 30–6,000 M_{\oplus} and obtained the posterior sample for the rate density parameters using the *epos* code (GijsMulders 2019). Using this function, we assigned planets (i.e., occurrence, mass, and period) to a subset of *Kepler* stars, which we call \mathcal{S}_{H} , in the same region of the HR diagram as spanned by the stars in the HARPS volume-limited sample (Sousa et al. 2011). This ensures that the comparison can be made for *Kepler* stars with similar properties as those in the HARPS sample. We have not corrected for possible difference in the stellar binarity between the volume-limited HARPS sample and the *Kepler* stars, but this effect is likely minor as long as we

focus on giant planets (Bouma et al. 2018). The planetary masses are converted to radii using a broken power-law fit to the known planets with a break at 100 M_{\oplus} , and the transit duration was computed assuming the Beta distribution for eccentricities (Kipping 2013b) and random distributions for the argument of periastron and cosine of the orbital inclination. We then computed the transit signal-to-noise ratio and the corresponding detectability following Fulton et al. (2017) using Combined Differential Photometric Precision (CDPP; Koch et al. 2010), and counted the expected number of transit detection for planets larger than $8R_{\oplus}$ as a function of period. Although the process is not totally justified for planets with less than three transits, the detection efficiency curve likely plays a minor role for planets larger than $8R_{\oplus}$ because of large signals. The whole simulation was repeated 1,000 times for the occurrence density parameters randomly sampled from the *epos* posterior.

Figure 19 compares the result against the subsets of the clean KOIs and our clean sample that are also part of \mathcal{S}_{H} . The thick black line shows the mean of the 1,000 simulations, and thin lines show 20 random posteriors (i.e., 2σ samples). Since the mean [Fe/H] of the HARPS sample (-0.1 ; Sousa et al. 2011) is lower than the mean of the *Kepler* field stars (Dong et al. 2014; Guo et al. 2017), we also show the mean occurrence corrected for this difference assuming $10^{2[\text{Fe}/\text{H}]}$ dependence derived for giant planets out to 4-yr orbits (Fischer & Valenti 2005). We find a generally good agreement except for the region around 10 days and 1–2 yr. The former is likely the gap in the occurrence (e.g. Santerne et al. 2016) that is not taken into account in the adopted power-law model. The origin of the latter tension is unclear; it may indicate that a few planets with three transits are missed in the KOI catalog, and were missed in our search as well.

6.2. Radius Distribution

Let us have a closer look at the radius distribution using the combined clean KOI sample and our long-period sample. Here we focus on giant planets $> 4R_{\oplus}$, for which completeness of the KOI sample is likely high at least for $P \lesssim 1$ yr (e.g. Petigura et al. 2018).

Figure 20 shows the normalized histogram and cumulative distribution for the planetary radius. The radius distribution for $P > 700$ days is roughly log-flat down to $4R_{\oplus}$ (bottom panel), suggesting that Neptune-sized planets are at least as common as Jupiter-sized ones in this period range. In addition, we found very similar distributions for $P > 700$ days and 100 days $< P < 700$ days (top panel) with the KS p -value of 0.9. In other words, we did not find any significant change in the radius distribution around the snow line. Given that we

⁷ Two candidates reported in Herman et al. (2019) are excluded in this counting.

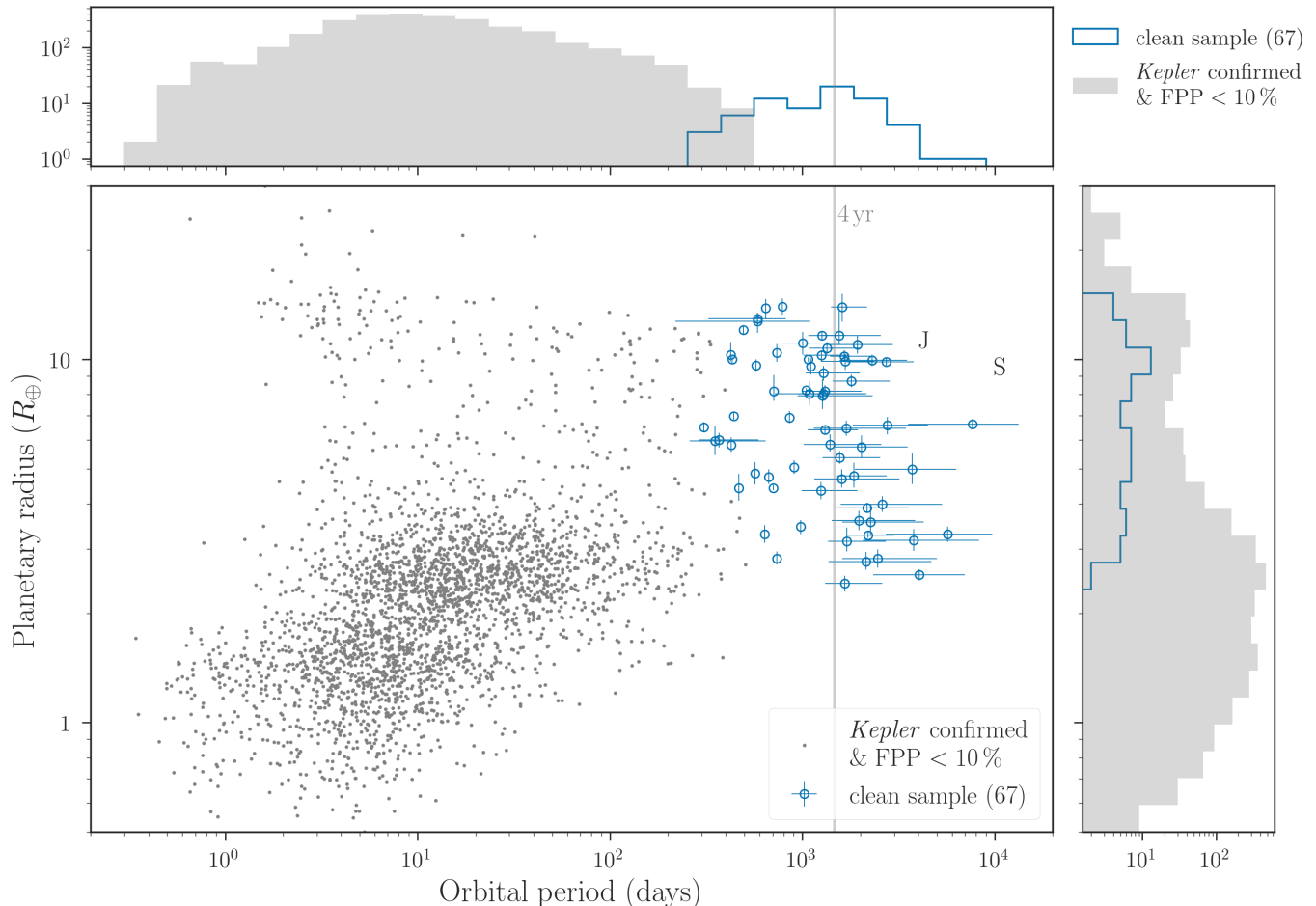


Figure 18. Radii and orbital periods of our clean sample defined in Section 5 (open blue circles), along with confirmed *Kepler* planets and candidates with false positive probabilities (Morton et al. 2016) less than 10%. The locations of Jupiter and Saturn are shown by “J” and “S,” respectively.

have not corrected for completeness, two interpretations are possible: the radius distributions do remain to be the same and our search completeness is high for planets down to $4 R_{\oplus}$; or there actually exist more small planets in $P > 700$ days range than in $100 \text{ days} < P < 700$ days.

Figure 20 also shows the radius distributions for planets with $P < 100$ days. Here the bin edges roughly correspond to the radius values across which the radius distribution was found to show significant changes based on the KS p -value. The bin with $P < 3$ days is dominated by inflated hot Jupiters larger than $11 R_{\oplus}$ and lack smaller planets in the sub-Saturn desert (Szabó & Kiss 2011; Lundkvist et al. 2016). For longer periods, Jupiter-sized planets become less inflated and smaller planets start to dominate. The origin of the difference across $P \sim 100$ days is not clear; this might be related to the prevalence of lower-density sub-Saturns at longer orbital periods as hinted by systematic analysis of transit timing variations (Hadden & Lithwick 2017).

6.3. $[Fe/H]$ of the Host Stars

Figure 21 shows stellar $[Fe/H]$ and planetary radius for a subset of the clean sample with spectroscopic parameters. Here we use $[Fe/H]$ values from raw spectroscopy (rightmost column of Table 2), although the following arguments qualitatively remain to be the same for the values from the isochrone fit.

The planets larger than $4 R_{\oplus}$ are found mostly around stars with $[Fe/H] > -0.15$, while the hosts of smaller planets have a wider range of $[Fe/H]$ (upper panel). The host stars of planets larger than $4 R_{\oplus}$ are also systematically more metal rich than the FGK dwarfs ($T_{\text{eff}} = 4700\text{--}6500$ K, $\log g = 3.9\text{--}5.0$) in the *Kepler* field from LAMOST DR4 (lower panel), with the KS p -value of 0.8%. This indicates that the giant planet–metallicity correlation confirmed for the shorter-period sample (Petigura et al. 2018) also holds for planets with periods longer than two years.

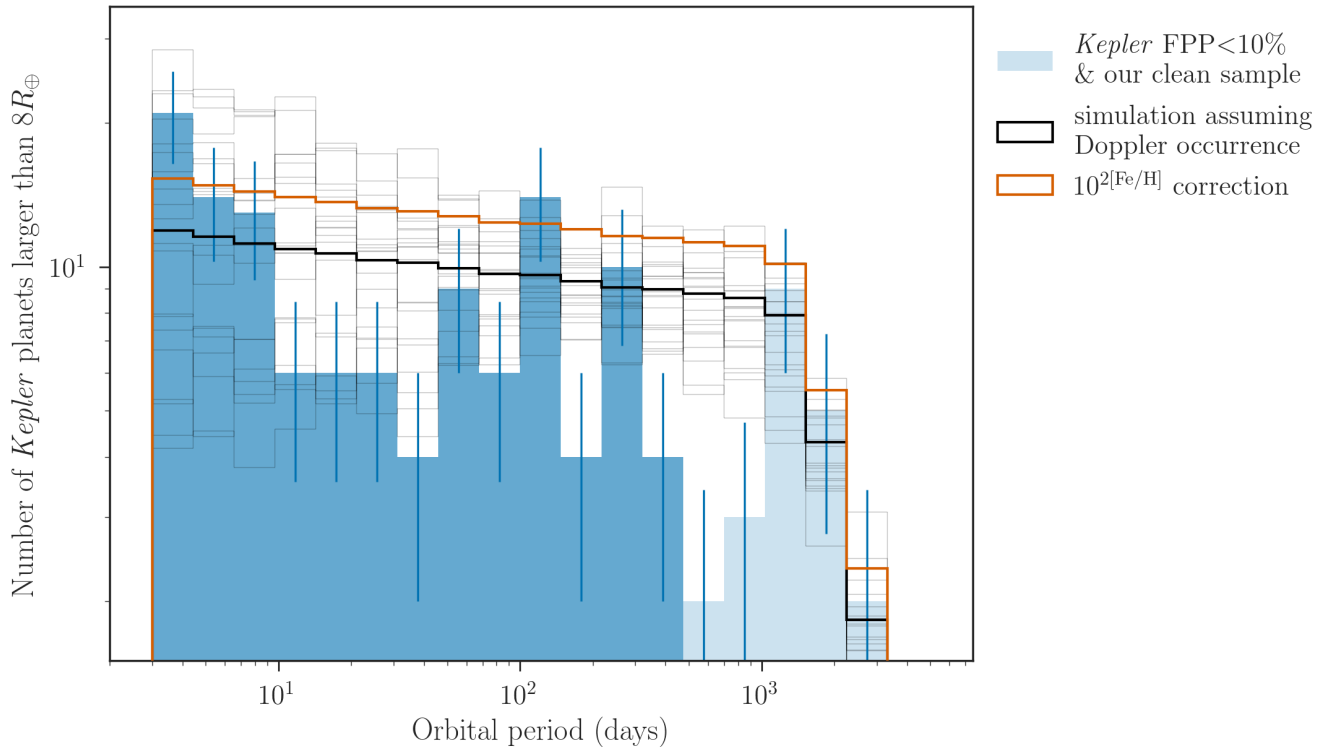


Figure 19. The period distribution of transiting planets larger than $8 R_{\oplus}$ from the *Kepler* prime mission. The histogram shows the distribution of the clean KOI sample defined in Section 6 (thick blue) and our clean sample defined in Section 5.2 (thin blue). The black lines show the simulated distribution based on the Doppler occurrence (thick: mean, thin: random posterior samples). The thick orange line shows the mean of the simulated results corrected for the different mean $[\text{Fe}/\text{H}]$ between the *Kepler* stars and targets in the Doppler survey. See Section 6.1 for details.

One clear outlier in the plot, KIC 9822143, has the radius of $9.9 R_{\oplus}$ and $[\text{Fe}/\text{H}]$ of -0.67 (*SpecMatch-Emp*) or -0.47 (isochrone modeling). This candidate might be a brown dwarf, which occurs around stars with a wider range of $[\text{Fe}/\text{H}]$ (Ma & Ge 2014).

6.4. Occurrence Rate

Although we have not quantified the detection completeness in our search, here we estimate the occurrence of giant planets $> 4 R_{\oplus}$ for reference, assuming that the completeness is high.

Defining the transit signal-to-noise $s_{\text{tra}}(r)$ by $(r/R_{\star})^2/\sigma_{15}$, where σ_{15} is the CDPP for the longest 15 h timescale, we find that our sample has an s_{tra} cutoff at ≈ 10 and the cutoff is independent of the *Kepler* magnitude. Given this observation, we computed $s_{\text{tra}}(4 R_{\oplus})$ for all the *Kepler* stars using the radii from Berger et al. (2018), and found that ≈ 67000 *Kepler* stars with $4700 \text{ K} < T_{\text{eff}} < 6500 \text{ K}$ have $s_{\text{tra}}(r) > 10$; these are the Sun-like stars (which turned out to be mostly on the main sequence) for which Neptune-sized transiting planets, if present, would have been detected. On the other hand, there are 32 planets with $r > 4 R_{\oplus}$ and $P > 2 \text{ yr}$ in our sample.

We follow equations 12 and 13 in Foreman-Mackey et al. (2016) (see also the Appendix of Foreman-Mackey et al. 2014) and assume that the detection completeness is 100% for any relevant r and P and that the rate density per $\ln P$ is constant in our search range. Then we find the occurrence rate density per $\ln P$ for planets with $r = 4\text{--}14 R_{\oplus}$ and $P = 2\text{--}20 \text{ yr}$ to be 0.17 ± 0.03 , or the occurrence rate integrated in this range to be 0.39 ± 0.07 per star with $4700 \text{ K} < T_{\text{eff}} < 6500 \text{ K}$. Here the error bar takes into account the Poisson noise alone. Interestingly, the result agrees with the value 0.29 ± 0.11 derived by Foreman-Mackey et al. (2016) for a similar radius range ($0.4\text{--}1.0 R_{\text{Jup}}$) but after completeness correction (their table 6).⁸

6.5. Systems with Inner Planets

Our clean sample includes 10 planet candidates with confirmed inner transiting planets (Table 3). These planets have higher fidelity to be genuine planets (Lissauer et al. 2012). The fraction of such systems in our

⁸ Here the $\pi^{1/3}$ error in the transit probability is corrected (see Herman et al. 2019).

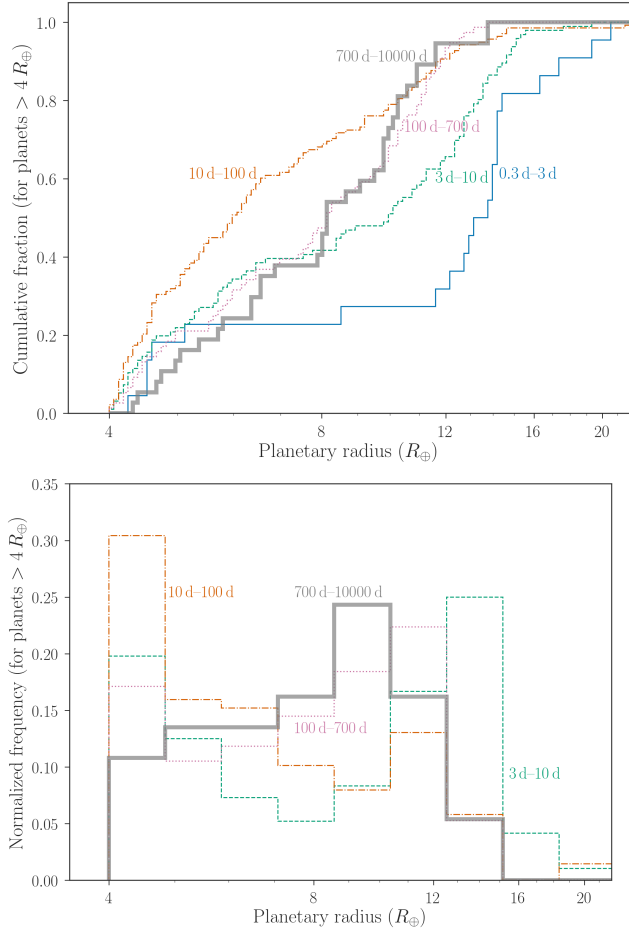


Figure 20. Radius distribution of our samples with $P > 700$ days (thick gray line), compared with the shorter-period planets in the clean KOI sample defined in Section 6. *Upper panel* — normalized cumulative radius distributions for planets with $r > 4 R_{\oplus}$. *Lower panel* — normalized radius histograms for planets with $r > 4 R_{\oplus}$.

sample ($9/67 = 15\%$) is significantly higher than the fraction of confirmed *Kepler* stars among all the *Kepler* stars ($\sim 1\%$). This is likely due to the correlation of planet occurrences and orbital inclinations between inner and outer planets (Uehara et al. 2016; Herman et al. 2019). It may also be the case that the stars with inner, typically smaller transiting planets detected have systematically less noisy light curves and bias for the detection of longer-period transiting planets.

6.6. Mass Distribution

If the empirical mass–radius relation in Chen & Kipping (2017) is adopted, the radius distribution of our planet sample with $P > 700$ days suggests that the occurrence rate density per log planet mass (planet-to-star mass ratio) at $\sim 30 M_{\oplus}$ ($\sim 10^{-4}$) is higher than that around $\sim M_{\text{Jup}}$ ($\sim 10^{-3}$) by almost an order of

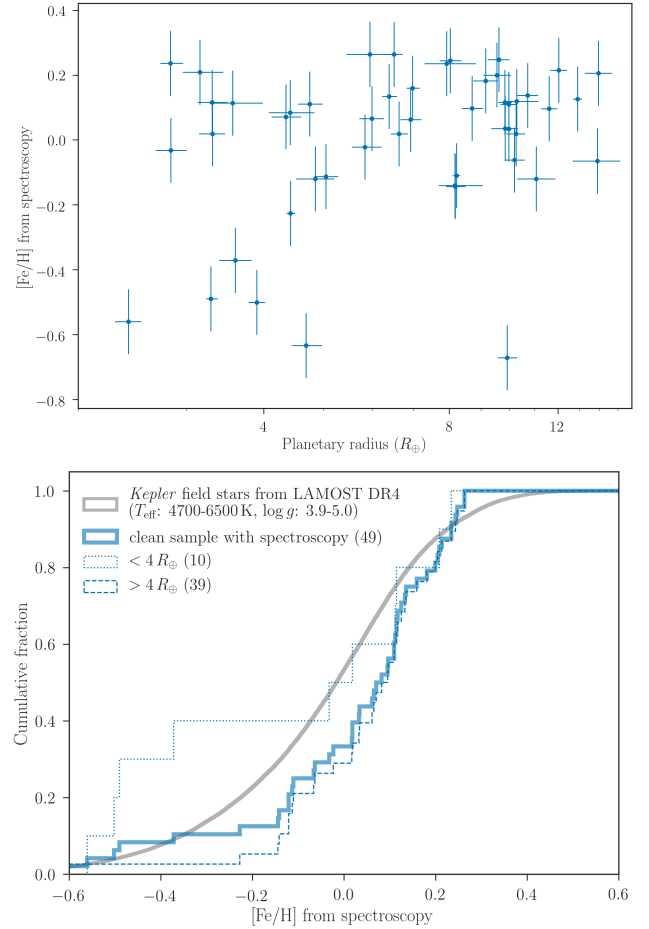


Figure 21. $[\text{Fe}/\text{H}]$ distribution of the host stars in our clean sample with spectroscopic measurements, compared to the *Kepler* field stars. *Upper panel* — $[\text{Fe}/\text{H}]$ against planetary radii. *Lower panel* — Thick blue line is the cumulative $[\text{Fe}/\text{H}]$ distribution of the clean sample; dashed and dotted lines are its subsets with $> 4 R_{\oplus}$ and $< 4 R_{\oplus}$ planets, respectively; the thick gray line is the $[\text{Fe}/\text{H}]$ distribution of FGK dwarf *Kepler* stars from LAMOST DR4.

magnitude. Such a slope is compatible with the value implied from microlensing surveys for planets near the snow line of late dwarfs (Suzuki et al. 2016). Quantifying the completeness for smaller planets is essential for more detailed comparisons.

7. IMPLICATIONS FOR FUTURE DIRECT IMAGING

Abundance and properties of the long-period exoplanets are useful for forecasting the outcome of future direct imaging missions. In Figure 22, we convert planet and stellar properties in the clean sample to star–planet contrast ratios (hereafter contrast) in visible and infrared bands. The contrast C at the wavelength λ was computed as the sum of scattered light and thermal emission

from a planet:

$$C(\lambda) = \frac{2}{3}A\phi(\beta)\frac{r^2}{a^2} + \frac{r^2}{R_\star^2}\frac{e^{\frac{hc}{\lambda k_B T_{\text{eff}}}} - 1}{e^{\frac{hc}{\lambda k_B T_p}} - 1}, \quad (13)$$

where A is the Bond albedo, a is the orbital semi-major axis, h is the Planck constant, c is the speed of light, and k_B is the Boltzmann constant. In the first term (scattered light),

$$\phi(\beta) \equiv [\sin \beta + (\pi - \beta) \cos \beta]/\pi, \quad (14)$$

is the Lambert phase function, where β is an observer–star–planet phase angle and we adopt $\beta = \pi/2$. Given the values of Bond albedo of Jupiter, Saturn, Uranus, and Neptune are 0.50, 0.34, 0.3, and 0.29, respectively, here we adopt $A = 0.4$ for simplicity. In the second term (emission light), we adopt the radiative equilibrium temperature

$$T_{p,\text{eq}} = \left(\frac{1-A}{4}\right)^{1/4} T_{\text{eff}} \sqrt{\frac{R_\star}{a}}, \quad (15)$$

for the planet temperature T_p . For typical T_p for the long-period planets, the scattered light dominates the contrast in the visible band, while the thermal emission is much larger in the infrared band.

The baseline technical goal of the contrast of the WFIRST coronagraph instrument (CGI) in the visible band is 10^{-9} with an inner working angle of 0.2 arcsec, which corresponds to a semi-major axis of 1–2 AU at a distance of 5–10 pc (Spiegel et al. 2015, see also the website of WFIRST)⁹. The left panel of Figure 22 shows that the planets down to $\sim 4 R_\oplus$ in the clean sample have contrasts above the goal of the WFIRST CGI, if those planets are found at 5–10 pc. In addition, those Neptune-sized planets near the snow line around the nearest stars ($\lesssim 5$ pc) can be a potential target for ground-based extreme adaptive optics systems in infrared bands to detect planet’s thermal emission, such as TIKI (Blain et al. 2018), which aims to achieve contrast of 10^{-7} for nearby bright stars (the right panel in Figure 22). Thus, such Neptune-sized planets at a few au,

if found around nearby stars, can be promising targets for direct imaging surveys in the next decade.

This paper includes data collected by the *Kepler* mission. Funding for the *Kepler* mission is provided by the NASA Science Mission directorate. We are grateful to Sho Uehara for his help with visual inspection to find some transit events newly reported in the paper. We also thank Masahiro Ikoma, Masataka Aizawa, Tadahiro Kimura, Kentaro Aoki, Akito Tajitsu, Daisuke Suzuki, Chris Packham, Mitsuhiko Honda, and Makiko Nagasawa for helpful and fruitful conversations. We also thank Akihiko Fukui for the inspiration for the name of this catalog. We thank Samuel Yee and Yuan-Sen Ting for their suggestions on the spectroscopic stellar parameters. H.K. is supported by a Grant-in-Aid from JSPS (Japan Society for the Promotion of Science), Nos. JP17K14246, JP18H01247 and JP18H04577. Work by K.M. was performed under contract with the California Institute of Technology (Caltech)/Jet Propulsion Laboratory (JPL) funded by NASA through the Sagan Fellowship Program executed by the NASA Exoplanet Science Institute. This work was also supported by the JSPS Core-to-Core Program “Planet²”. The authors wish to recognize and acknowledge the very significant cultural role and reverence that the summit of Mauna Kea has always had within the indigenous Hawaiian community. We are most fortunate to have the opportunity to conduct observations from this mountain.

Facilities: *Kepler*, Subaru/HDS

Software: scikit-learn (Pedregosa et al. 2011), matplotlib (Hunter 2007), lightkurve (Vincius et al. 2018), specmatch-emp (Yee et al. 2017), isochrones (Morton 2015), numpy (van der Walt et al. 2011), scipy (Jones et al. 2001), pycuda (Klöckner et al. 2012), python3, celerite (Foreman-Mackey et al. 2017), emcee (Foreman-Mackey et al. 2013), batman (Kreidberg 2015)

REFERENCES

- Bailer-Jones, C. A. L., Rybizki, J., Fouesneau, M., Mantelet, G., & Andrae, R. 2018, *AJ*, 156, 58
- Becker, J. C., & Adams, F. C. 2017, *MNRAS*, 468, 549
- Berger, T. A., Huber, D., Gaidos, E., & van Saders, J. L. 2018, *ApJ*, 866, 99
- Blain, C., Marois, C., Bradley, C., et al. 2018, in Society of Photo-Optical Instrumentation Engineers (SPIE) Conference Series, Vol. 10702, Ground-based and Airborne Instrumentation for Astronomy VII, 107024A

⁹ https://wfirst.gsfc.nasa.gov/exoplanets_direct_imaging.html

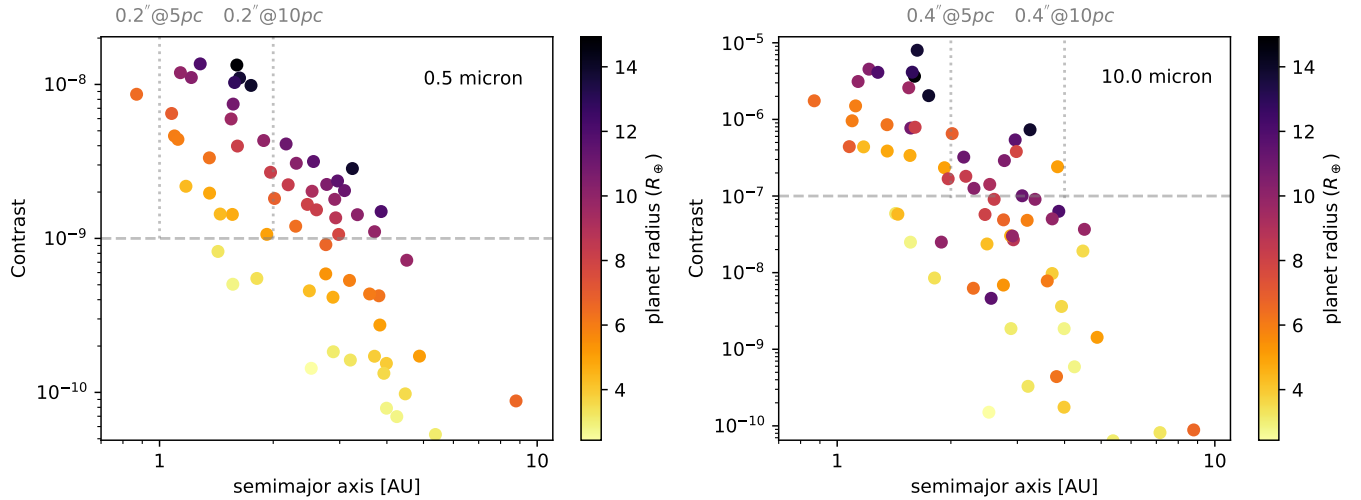


Figure 22. Expected star–planet contrast and semi-major axis of the planets in the clean sample, at $0.5 \mu\text{m}$ (left) and $10 \mu\text{m}$ (right). The Bond albedo of 0.4 is assumed for all the planets. The color bar indicates the planet radius. The horizontal dashed lines indicate the baseline technical goal of the WFIRST CGI (left) and a fiducial goal of a ground-based direct imaging instrument in a thermal band (right). The vertical dotted lines show the semi-major axes corresponding to a fiducial inner working angle (IWA) at distances of 5 pc and 10 pc. The IWA for WFIRST CGI is assumed to be 0.2 arcsec (left) and a fiducial IWA of $2\lambda/D = 0.4$ arcsec is adopted for a high-contrast, infrared ($\lambda = 10 \mu\text{m}$) instrument on a $D = 10$ m telescope (right).

- Borucki, W. J., Koch, D. G., Basri, G., et al. 2011, *ApJ*, 736, 19
- Bouma, L. G., Masuda, K., & Winn, J. N. 2018, *AJ*, 155, 244
- Brewer, J. M., Fischer, D. A., Valenti, J. A., & Piskunov, N. 2016, *ApJS*, 225, 32
- Bryan, M. L., Knutson, H. A., Lee, E. J., et al. 2019, *AJ*, 157, 52
- Bryson, S. T., Jenkins, J. M., Gilliland, R. L., et al. 2013, *PASP*, 125, 889
- Cassan, A., Kubas, D., Beaulieu, J.-P., et al. 2012, *Nature*, 481, 167
- Chen, J., & Kipping, D. 2017, *ApJ*, 834, 17
- Couturier, R. 2013, *Designing scientific applications on gpus* (CRC Press)
- Cui, X.-Q., Zhao, Y.-H., Chu, Y.-Q., et al. 2012, *Research in Astronomy and Astrophysics*, 12, 1197
- Cumming, A., Butler, R. P., Marcy, G. W., et al. 2008, *PASP*, 120, 531
- Dalba, P. A., & Muirhead, P. S. 2016, *ApJ*, 826, L7
- Dalba, P. A., & Tamburo, P. 2019, *ApJ*, 873, L17
- Dong, S., Zheng, Z., Zhu, Z., et al. 2014, *ApJL*, 789, L3
- Dotter, A., Chaboyer, B., Jevremović, D., et al. 2008, *ApJS*, 178, 89
- Fernandes, R. B., Mulders, G. D., Pascucci, I., Mordasini, C., & Emsenhuber, A. 2018, *arXiv e-prints*, arXiv:1812.05569
- Fischer, D. A., & Valenti, J. 2005, *ApJ*, 622, 1102
- Foreman-Mackey, D., Agol, E., Angus, R., & Ambikasaran, S. 2017, *ArXiv*
- Foreman-Mackey, D., Hogg, D. W., Lang, D., & Goodman, J. 2013, *PASP*, 125, 306
- Foreman-Mackey, D., Hogg, D. W., & Morton, T. D. 2014, *ApJ*, 795, 64
- Foreman-Mackey, D., Morton, T. D., Hogg, D. W., Agol, E., & Schölkopf, B. 2016, *AJ*, 152, 206
- Fulton, B. J., & Petigura, E. A. 2018, *AJ*, 156, 264
- Fulton, B. J., Petigura, E. A., Howard, A. W., et al. 2017, *AJ*, 154, 109
- Furlan, E., Ciardi, D. R., Everett, M. E., et al. 2017, *AJ*, 153, 71
- Gaia Collaboration, Brown, A. G. A., Vallenari, A., et al. 2018, *A&A*, 616, A1
- GijsMulders. 2019, *GijsMulders/epos: This version accompanies Fernandes et al. 2019, , , doi:10.5281/zenodo.2552594*
- Giles, H. A. C., Osborn, H. P., Blanco-Cuaresma, S., et al. 2018, *A&A*, 615, L13
- Gould, A., Dong, S., Gaudi, B. S., et al. 2010, *ApJ*, 720, 1073
- Green, G. M., Schlafly, E. F., Finkbeiner, D., et al. 2018, *MNRAS*, 478, 651
- Grether, D., & Lineweaver, C. H. 2006, *ApJ*, 640, 1051
- Guo, X., Johnson, J. A., Mann, A. W., et al. 2017, *ApJ*, 838, 25
- Hadden, S., & Lithwick, Y. 2017, *AJ*, 154, 5
- Hansen, B. M. S. 2017, *MNRAS*, 467, 1531
- Hayashi, C. 1981, *Progress of Theoretical Physics Supplement*, 70, 35

- Herman, M. K., Zhu, W., & Wu, Y. 2019, arXiv e-prints, arXiv:1901.01974
- Howell, S. B., Sobek, C., Haas, M., et al. 2014, *PASP*, 126, 398
- Huang, C. X., Petrovich, C., & Deibert, E. 2017, *AJ*, 153, 210
- Hunter, J. D. 2007, *Computing In Science & Engineering*, 9, 90
- Jones, E., Oliphant, T., Peterson, P., et al. 2001, *SciPy: Open source scientific tools for Python*, ,
- Kawahara, H., Masuda, K., MacLeod, M., et al. 2018, *AJ*, 155, 144
- Kipping, D. 2018, *Research Notes of the American Astronomical Society*, 2, 223
- Kipping, D. M. 2013a, *MNRAS*, 435, 2152
- . 2013b, *MNRAS*, 434, L51
- Kipping, D. M., Torres, G., Henze, C., et al. 2016, *ApJ*, 820, 112
- Kirk, B., Conroy, K., Prša, A., et al. 2016, *AJ*, 151, 68
- Klößner, A., Pinto, N., Lee, Y., et al. 2012, *Parallel Computing*, 38, 157
- Koch, D. G., Borucki, W. J., Basri, G., et al. 2010, *ApJL*, 713, L79
- Kreidberg, L. 2015, *PASP*, 127, 1161
- Lai, D., & Pu, B. 2017, *AJ*, 153, 42
- Lissauer, J. J., Marcy, G. W., Rowe, J. F., et al. 2012, *ApJ*, 750, 112
- Lundkvist, M. S., Kjeldsen, H., Albrecht, S., et al. 2016, *Nature Communications*, 7, 11201
- Luo, A.-L., Zhao, Y.-H., Zhao, G., et al. 2015, *Research in Astronomy and Astrophysics*, 15, 1095
- Ma, B., & Ge, J. 2014, *MNRAS*, 439, 2781
- Majewski, S. R., Schiavon, R. P., Frinchaboy, P. M., et al. 2017, *AJ*, 154, 94
- Mandel, K., & Agol, E. 2002, *ApJL*, 580, L171
- Martin, R. G., & Livio, M. 2012, *MNRAS*, 425, L6
- Mathur, S., Huber, D., Batalha, N. M., et al. 2017, *ApJS*, 229, 30
- Mayor, M., Marmier, M., Lovis, C., et al. 2011, arXiv e-prints, arXiv:1109.2497
- Morton, T. D. 2015, *isochrones: Stellar model grid package, Astrophysics Source Code Library*, , ascl:1503.010
- Morton, T. D., Bryson, S. T., Coughlin, J. L., et al. 2016, *ApJ*, 822, 86
- Mulders, G. D., Ciesla, F. J., Min, M., & Pascucci, I. 2015, *ApJ*, 807, 9
- Mullally, F., Coughlin, J. L., Thompson, S. E., et al. 2015, *ApJS*, 217, 31
- Murphy, S. J. 2018, ArXiv e-prints, arXiv:1811.12659
- Murphy, S. J., Bedding, T. R., Shibahashi, H., Kurtz, D. W., & Kjeldsen, H. 2014, *MNRAS*, 441, 2515
- Murphy, S. J., Moe, M., Kurtz, D. W., et al. 2018, *MNRAS*, 474, 4322
- Murphy, S. J., & Shibahashi, H. 2015, *MNRAS*, 450, 4475
- Mustill, A. J., Davies, M. B., & Johansen, A. 2017, *MNRAS*, 468, 3000
- Noguchi, K., Aoki, W., Kawanomoto, S., et al. 2002, *PASJ*, 54, 855
- Oka, A., Nakamoto, T., & Ida, S. 2011, *ApJ*, 738, 141
- Osborn, H. P., Armstrong, D. J., Brown, D. J. A., et al. 2016, *MNRAS*, 457, 2273
- Pedregosa, F., Varoquaux, G., Gramfort, A., et al. 2011, *Journal of Machine Learning Research*, 12, 2825
- Petigura, E. A., Howard, A. W., Marcy, G. W., et al. 2017, *AJ*, 154, 107
- Petigura, E. A., Marcy, G. W., Winn, J. N., et al. 2018, *AJ*, 155, 89
- Pinsonneault, M. H., An, D., Molenda-Żakowicz, J., et al. 2012, *ApJS*, 199, 30
- Pu, B., & Lai, D. 2018, *MNRAS*, 478, 197
- Raghavan, D., McAlister, H. A., Henry, T. J., et al. 2010, *ApJS*, 190, 1
- Santerne, A., Moutou, C., Tsantaki, M., et al. 2016, *A&A*, 587, A64
- Schmitt, J. R., Jenkins, J. M., & Fischer, D. A. 2017, *AJ*, 153, 180
- Schmitt, J. R., Wang, J., Fischer, D. A., et al. 2014, *AJ*, 148, 28
- Shibahashi, H., & Kurtz, D. W. 2012, *MNRAS*, 422, 738
- Shibahashi, H., Kurtz, D. W., & Murphy, S. J. 2015, *MNRAS*, 450, 3999
- Skrutskie, M. F., Cutri, R. M., Stiening, R., et al. 2006, *AJ*, 131, 1163
- Sousa, S. G., Santos, N. C., Israelian, G., Mayor, M., & Udry, S. 2011, *A&A*, 533, A141
- Sowicka, P., Handler, G., Dębski, B., et al. 2017, *MNRAS*, 467, 4663
- Spergel, D., Gehrels, N., Baltay, C., et al. 2015, arXiv e-prints, arXiv:1503.03757
- Suzuki, D., Bennett, D. P., Sumi, T., et al. 2016, *ApJ*, 833, 145
- Szabó, G. M., & Kiss, L. L. 2011, *ApJL*, 727, L44
- Tajitsu, A., Aoki, W., & Yamamuro, T. 2012, *PASJ*, 64, 77
- Ting, Y.-S., Conroy, C., Rix, H.-W., & Cargile, P. 2018, arXiv e-prints, arXiv:1804.01530
- Twicken, J. D., Jenkins, J. M., Seader, S. E., et al. 2016, *AJ*, 152, 158
- Uehara, S., Kawahara, H., Masuda, K., Yamada, S., & Aizawa, M. 2016, *ApJ*, 822, 2

- van der Walt, S., Colbert, S. C., & Varoquaux, G. 2011, *Computing in Science and Engineering*, 13, 22
- Vincius, Z., Barentsen, G., Hedges, C., Gully-Santiago, M., & Cody, A. M. 2018, *KeplerGO/lightkurve*, , , doi:10.5281/zenodo.1181928
- Wang, J., Fischer, D. A., Barclay, T., et al. 2015, *ApJ*, 815, 127
- Wu, Y., Du, B., Luo, A., Zhao, Y., & Yuan, H. 2014, in *IAU Symposium, Vol. 306, Statistical Challenges in 21st Century Cosmology*, ed. A. Heavens, J.-L. Starck, & A. Krone-Martins, 340–342
- Yee, J. C., & Gaudi, B. S. 2008, *ApJ*, 688, 616
- Yee, S. W., Petigura, E. A., & von Braun, K. 2017, *ApJ*, 836, 77
- Zhu, W., & Wu, Y. 2018, *AJ*, 156, 92

APPENDIX

A. ALGORITHM OF THE GPU-BASED TRAPEZOID LEAST SQUARE

To minimize equation (1), we use the derivative of χ^2 by H ,

$$\begin{aligned} \sigma^2 \frac{\partial \chi^2}{\partial H} = & \frac{H}{2}(n_a - n_c + n_e) + \frac{HW^2}{8L^2}(n_b + n_d) + \sum_{t_i \in a, e, c} x_i - \frac{W}{2L} \sum_{t_i \in b, d} x_i + \frac{2}{L} \left(\sum_{t_i \in d} x_i t_i - \sum_{t_i \in b} x_i t_i \right) \\ & + \frac{HW}{L^2} \left(\sum_{t_i \in b} t_i - \sum_{t_i \in d} t_i \right) + \frac{2H}{L^2} \sum_{t_i \in b, d} t_i^2 = 0. \end{aligned} \quad (\text{A1})$$

where n_a to n_e is the number of the data points in the region of a to e . We obtain the height at the minimum χ^2 for each of the set of $L, W, t = t_0$ as

$$\tilde{H} = -B/A \quad (\text{A2})$$

$$A = 4L^2(n_a - n_c + n_e) + W^2(n_b + n_d) + 8W \left(\sum_{t_i \in b} t_i - \sum_{t_i \in d} t_i \right) + 16 \sum_{t_i \in b, d} t_i^2 \quad (\text{A3})$$

$$B = 8L^2 \sum_{t_i \in a, e, c} x_i - 4WL \sum_{t_i \in b, d} x_i + 16L \left(\sum_{t_i \in d} x_i t_i - \sum_{t_i \in b} x_i t_i \right). \quad (\text{A4})$$

We need to search for the minimum of χ^2 by varying L , W , and t_0 . The left panel in Figure 23 shows the structure of the NVIDIA/CUDA model. There are three types of memory: main memory, global memory, and shared memory. CPU uses main memory, which is located outside the GPU unit. The GPU has global memory and shared memory. The former is a common memory for all blocks and has a large size. Each computing block has shared memory. Threads in a block can transfer data from the corresponding shared memory much faster than from global memory. However, the size of shared memory is usually small.

First, we transfer the light curve from the main memory to the global memory. We allocate t_0 into blocks. The i -th block computes the χ^2 of the trapezoid for $t_0 = t[i]$. Then we transfer a small segment around $t_0 = t[i]$ ("scoop" in the right panel in Figure 23) to the shared memory so that the threads can read the data quickly. In addition, the j -th thread computes values for different widths $W = W[j]$. Finally, each thread has only a loop to search for the optimal L . Each block picks up the maximum value of

$$S/N(t_0) \equiv \frac{\tilde{H}}{\sqrt{\text{res}(n-3)}}, \quad (\text{A5})$$

where res is the residual of the fit, and $n-3$ is the degrees of freedom. We call this time series the TLS series.

B. THE LIST OF FALSE POSITIVES

Table 4 provides a list of eclipsing binaries identified in Sections 2.2 and 2.3, as well as the false positives identified in Section 3.

C. SYSTEM PARAMETESR AND LIGHT CURVES OF THE FLAGGED SYSTEMS

Here we show the light curves of the candidates flagged due to long ingress/egress durations (Figure 24) or radii too large to be planets (Figure 25). Table 5 reports the parameters for these systems.

Table 5. Parameters of the Flagged Systems.

KIC	KOI	K_p	$M_\star (M_\odot)$	$R_\star (R_\odot)$	$r (R_\oplus)$	t_0 (BKJD)	P (days)	b	e
3346436 [†]	...	12.4	$1.23^{+0.16}_{-0.06}$	$2.33^{+0.07}_{-0.07}$	125^{+4}_{-5}	$996.3255^{+0.0001}_{-0.0002}$	$(1.3^{+0.4}_{-0.3}) \times 10^3$	$0.819^{+0.008}_{-0.016}$	$0.69^{+0.04}_{-0.04}$

Table 5 continued

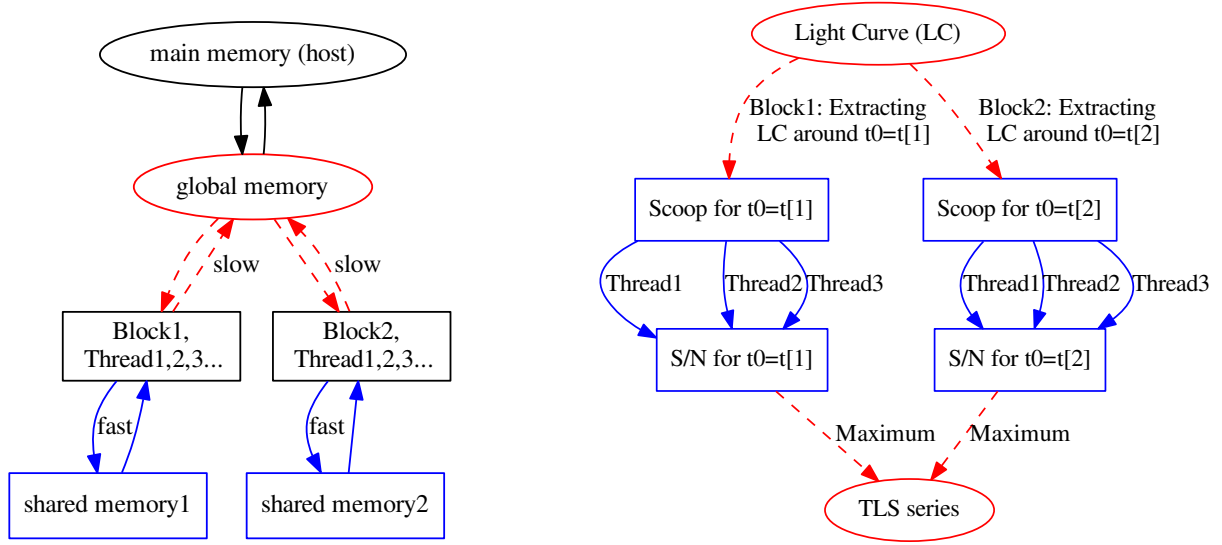


Figure 23. The structure of the CUDA-GPU model (left) and the parallelization of the TLS algorithm (right). In the CUDA-GPU model, transfer from shared memory (blue boxes) is faster than from global memory (red circles), although the shared memory size is much smaller than the global memory size. Each block has its own shared memory and consists of a set of threads. In our GPU-based TLS code, we transfer a segment of the light curve around the central time t_0 from the entire light curve stored in the global memory to the corresponding shared memories. Each thread in a block computes the residual of the data from the trapezoid model for a different width, W .

Table 5 (continued)

KIC	KOI	K_p	M_* (M_\odot)	R_* (R_\odot)	r (R_\oplus)	t_0 (BKJD)	P (days)	b	e
3526901 [†]	...	15.4	$0.98^{+0.04}_{-0.02}$	$2.0^{+0.1}_{-0.1}$	14^{+1}_{-1}	$1447.953^{+0.006}_{-0.006}$	$(1.5^{+1.1}_{-0.3}) \times 10^3$	$0.90^{+0.01}_{-0.02}$	$0.3^{+0.2}_{-0.2}$
4042088 [†]	6378 (FP)	13.4	$1.25^{+0.04}_{-0.05}$	$1.43^{+0.03}_{-0.03}$	$46.1^{+23.0}_{-14.0}$	$617.6551^{+0.0008}_{-0.0008}$	$(1.3^{+0.7}_{-0.3}) \times 10^3$	$1.1^{+0.2}_{-0.1}$	$0.54^{+0.10}_{-0.06}$
4729586 [†]	...	12.3	$2.65^{+0.08}_{-0.04}$	$12.0^{+0.6}_{-0.6}$	$246.4^{+178.2}_{-69.3}$	$1141.71^{+0.04}_{-0.04}$	$(2.0^{+1.3}_{-0.7}) \times 10^3$	$1.0^{+0.2}_{-0.1}$	$0.2^{+0.2}_{-0.1}$
4754460 [†]	...	14.9	$0.87^{+0.03}_{-0.02}$	$1.10^{+0.03}_{-0.03}$	$6.9^{+0.4}_{-0.3}$	$826.837^{+0.004}_{-0.005}$	$(2.1^{+1.6}_{-0.9}) \times 10^3$	$0.89^{+0.02}_{-0.04}$	$0.2^{+0.2}_{-0.1}$
4754691 ^b	...	13.3	$0.88^{+0.02}_{-0.02}$	$0.95^{+0.01}_{-0.01}$	$28.4^{+13.6}_{-9.8}$	$1010.629^{+0.002}_{-0.002}$	$(1.2^{+0.9}_{-0.2}) \times 10^3$	$1.1^{+0.2}_{-0.1}$	$0.3^{+0.2}_{-0.1}$
5359568 [†]	...	13.1	$1.2^{+0.1}_{-0.2}$	$5.9^{+0.2}_{-0.2}$	37^{+1}_{-1}	$404.046^{+0.007}_{-0.007}$	$972.11^{+0.01}_{-0.01}$	$0.3^{+0.1}_{-0.1}$	$0.35^{+0.06}_{-0.05}$
5951458 [†]	...	12.7	$1.20^{+0.05}_{-0.03}$	$1.81^{+0.03}_{-0.04}$	$6.6^{+0.7}_{-0.5}$	$423.464^{+0.006}_{-0.006}$	$(1.6^{+1.1}_{-0.4}) \times 10^3$	$0.94^{+0.01}_{-0.02}$	$0.4^{+0.2}_{-0.2}$
6342758 [†]	...	14.6	$0.81^{+0.03}_{-0.03}$	$0.769^{+0.010}_{-0.009}$	12^{+6}_{-2}	$553.896^{+0.001}_{-0.001}$	$(1.4^{+0.7}_{-0.3}) \times 10^3$	$0.96^{+0.09}_{-0.06}$	$0.2^{+0.2}_{-0.1}$
6387193 [†]	...	14.9	$0.96^{+0.05}_{-0.04}$	$1.03^{+0.02}_{-0.02}$	$10.9^{+0.5}_{-0.5}$	$651.562^{+0.003}_{-0.003}$	$553.990^{+0.004}_{-0.003}$	$0.87^{+0.02}_{-0.03}$	$0.59^{+0.07}_{-0.06}$
7176219	...	13.8	$1.34^{+0.03}_{-0.03}$	$2.70^{+0.05}_{-0.06}$	$11.0^{+1.1}_{-0.7}$	$1100.286^{+0.006}_{-0.006}$	$(1.3^{+0.8}_{-0.2}) \times 10^3$	$0.92^{+0.02}_{-0.05}$	$0.6^{+0.1}_{-0.2}$
7381977 [†]	...	15.0	$0.91^{+0.05}_{-0.04}$	$0.93^{+0.02}_{-0.02}$	$4.4^{+0.3}_{-0.3}$	$1496.095^{+0.007}_{-0.007}$	$(2.0^{+1.7}_{-0.5}) \times 10^3$	$0.6^{+0.2}_{-0.3}$	$0.3^{+0.2}_{-0.2}$
7672940 [†]	1463 (FP)*	12.3	$1.36^{+0.04}_{-0.04}$	$1.67^{+0.06}_{-0.06}$	$26.1^{+1.0}_{-0.9}$	$144.0861^{+0.0002}_{-0.0002}$	$1064.2682^{+0.0003}_{-0.0003}$	$0.483^{+0.007}_{-0.008}$	$0.73^{+0.02}_{-0.02}$
7875441	...	15.6	$1.35^{+0.08}_{-0.14}$	$1.9^{+0.1}_{-0.1}$	$82.6^{+15.8}_{-11.6}$	$702.4502^{+0.0006}_{-0.0006}$	$(1.1^{+0.3}_{-0.2}) \times 10^3$	$0.87^{+0.10}_{-0.08}$	$0.48^{+0.09}_{-0.09}$
7947784	...	15.5	$1.12^{+0.10}_{-0.09}$	$1.35^{+0.08}_{-0.07}$	30^{+2}_{-2}	$905.2548^{+0.0009}_{-0.0009}$	$(1.0^{+0.6}_{-0.2}) \times 10^3$	$0.76^{+0.01}_{-0.01}$	$0.48^{+0.11}_{-0.09}$
8168680 [†]	...	12.3	$1.03^{+0.05}_{-0.05}$	$1.38^{+0.02}_{-0.02}$	$33.8^{+0.6}_{-0.6}$	$1151.6787^{+0.0002}_{-0.0002}$	$(0.9^{+0.2}_{-0.1}) \times 10^3$	$0.776^{+0.003}_{-0.003}$	$0.22^{+0.06}_{-0.06}$
8426957 [†]	...	13.6	$1.33^{+0.06}_{-0.07}$	$2.05^{+0.04}_{-0.04}$	$18.2^{+0.9}_{-0.7}$	$784.677^{+0.005}_{-0.003}$	$(7^{+5}_{-3}) \times 10^3$	$0.900^{+0.009}_{-0.011}$	$0.2^{+0.2}_{-0.1}$
8648356 [†]	...	11.7	$1.70^{+0.05}_{-0.05}$	$1.77^{+0.03}_{-0.03}$	$23.6^{+0.5}_{-0.5}$	$525.6574^{+0.0009}_{-0.0008}$	$(1.4^{+0.7}_{-0.3}) \times 10^3$	$0.28^{+0.04}_{-0.05}$	$0.49^{+0.09}_{-0.06}$

Table 5 continued

Table 4. List of the events removed during the visual inspection of stellar-sized signals (ST), the first screening of the targets (SC), visual inspection of the pixel data (VIP), search for signals with similar epochs (SE), and centroid shift test (CS). T_0 (BKJD) is an approximate position of the dip. ST (flat) is the stellar-sized eclipse with a flat bottom.

KIC	reason	T_0 (BKJD)	KIC	reason	T_0 (BKJD)	KIC	reason	T_0 (BKJD)
5475628	ST	950.5	3736610	VIP	1418.81	9019145	SE	142.16
6234593	ST	1148	3833007	VIP	981.7	9019245	SE	142.60
8463272	ST	641, 1206.7	4744261	VIP	478.82	9019513	SE	141.22
8508736	ST	261.3, 942.2	4932576	VIP	1272.7	9019948	SE	139.95
8570781	ST	1535.8	5480825	VIP	362.7	9086943	SE	142.65
9306307	ST	1191.3	5621767	VIP	839.2	1717717	SE	1439.20
9409599	ST	1324.9	6947459	VIP	1568.8	1717722	CS, SE	1439.20
4585946	ST	878	6962233	VIP	924.5	2162635	CS	176.1
5024447	ST	434.5, 1206.5	7190443	VIP	1200.7	3230491	CS	315.33
6757558	ST	779	7983622	VIP	471.7	3241604	CS	1263.41
9408440	ST	1503.5	8110811	VIP	1512.8	8082126	CS	794.3
7971363	ST (Flat)	675.5	10197310	VIP	1325.6	9970525	CS	139.71
8540376	SC	1520, 1552	10334763	VIP	549.5	10058021	CS	601.1
5522786	SC	283, (1040, 268.5, 872.5)	10668646	VIP	196.2, 1449.1	10602068	CS	830.81
8489948	SC	1578.5	3222471	VIP	673.			
			5480825	VIP	362.5			
			9291458	VIP	286.			
			6681473	VIP	471.2, 867.3, 1263.3			

Table 5 (*continued*)

KIC	KOI	K_p	$M_\star (M_\odot)$	$R_\star (R_\odot)$	$r (R_\oplus)$	t_0 (BKJD)	P (days)	b	e
9388752 [†]	...	11.6	$1.51^{+0.09}_{-0.05}$	$2.75^{+0.04}_{-0.05}$	$7.1^{+1.4}_{-0.7}$	$507.97^{+0.01}_{-0.01}$	$(1.5^{+1.4}_{-0.4}) \times 10^3$	$0.93^{+0.03}_{-0.05}$	$0.3^{+0.2}_{-0.2}$
10190048 ^b	...	15.7	$0.81^{+0.03}_{-0.02}$	$0.81^{+0.02}_{-0.02}$	26^{+9}_{-6}	$1260.586^{+0.001}_{-0.001}$	$(1.6^{+0.8}_{-0.3}) \times 10^3$	$1.0^{+0.1}_{-0.1}$	$0.3^{+0.1}_{-0.1}$
10321319 [†]	...	11.9	$1.00^{+0.03}_{-0.03}$	$1.51^{+0.02}_{-0.03}$	$3.4^{+0.4}_{-0.3}$	$554.352^{+0.008}_{-0.010}$	$(1.6^{+1.7}_{-0.4}) \times 10^3$	$0.83^{+0.08}_{-0.15}$	$0.3^{+0.2}_{-0.2}$
10403228	8007	16.1	$0.59^{+0.01}_{-0.01}$	$0.574^{+0.009}_{-0.010}$	19^{+8}_{-5}	$744.84^{+0.02}_{-0.02}$	$(17^{+9}_{-10}) \times 10^3$	$1.0^{+0.2}_{-0.1}$	$0.5^{+0.2}_{-0.2}$
10724544	...	15.0	$1.21^{+0.11}_{-0.07}$	$1.92^{+0.08}_{-0.08}$	$32.2^{+26.5}_{-10.8}$	$913.571^{+0.004}_{-0.005}$	$(1.1^{+0.8}_{-0.2}) \times 10^3$	$1.03^{+0.15}_{-0.08}$	$0.3^{+0.2}_{-0.2}$

* These stars have KOI numbers because of the STEs/DTEs analyzed here; they are the only transiting planet candidates.

[†] Stars with spectra.

□ Flat-bottomed transits with short ingress/egress; see Section 5.2.

^b Flagged as photometric binary by Berger et al. (2018).

NOTE—The reported values and errors are medians and 15.87th/84.13th percentiles of the marginal posterior.

multi-sine function with these modes,

$$\text{trend}(t) = \sum_{i=1}^N a_i \sin(2\pi f_i t + \phi_i) + C \quad (\text{D6})$$

D. TRANSIT EVENTS IN PULSATING STARS

KIC 6804821 is a delta scuti star, which is one of the typical variable stars. Oscillation of delta scuti stars consists of dozens of coherent modes. Performing the Fourier analysis of the light curve, we pick up $N = 27$ significant Fourier modes ($f_i, i = 1, \dots, N$). Fitting the

to the light curve outside the transit phase (C is the offset) around STE, we derive the trend of the star, as shown in the upper panel of Figure 26 (left). Detrending the light curve, we obtain a clear signal of the STE of KIC 6804821 (bottom panel in Figure 26). KIC

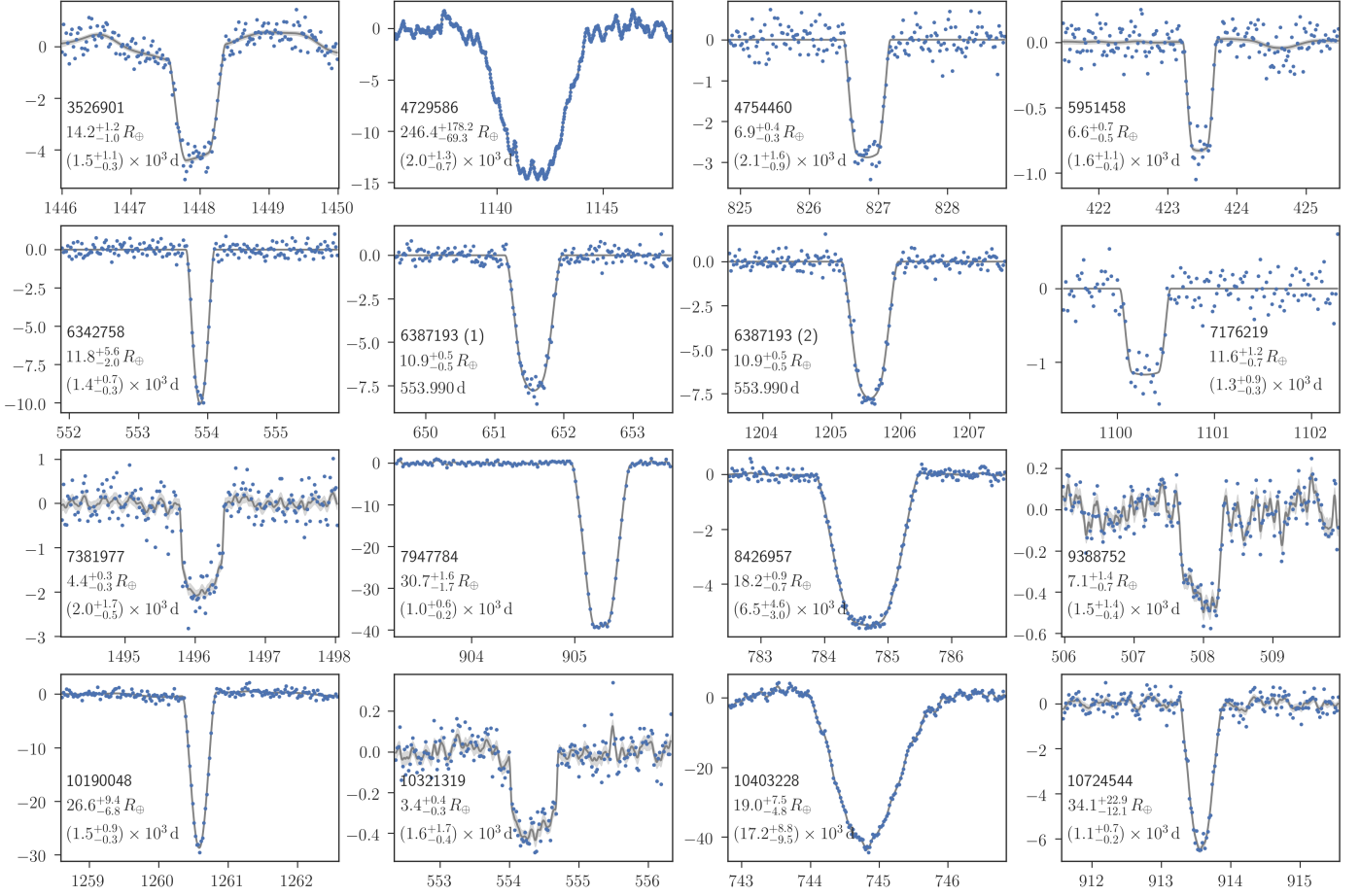


Figure 24. Same as Figure 13, but for potential false positives identified from long ingress/egress duration.

10284575 and KIC 8648356 also exhibit strong peaks in the power spectra. The mode frequencies of KIC 10284575 are lower than those of KIC 6804821. We show the de-trended curve of KIC 10284575 by the multi-sine de-trending in the right panels of Figure 26. The de-trended light curves for these three stars are used in the transit analysis. The coherent oscillation of the host star gives us information about a companion, if one exists, via the Rømer delay of the frequency (Shibahashi & Kurtz 2012). Phase modulation has been widely used to find their companions in delta scuti stars (e.g. Murphy et al. 2014; Shibahashi et al. 2015; Murphy & Shibahashi 2015). A companion in KIC 8648356 was found by Murphy (2018) when analyzing the phase modulation method. Assuming that STE and phase modulation have the same origin, its mass is consistent with a stellar one.

In our paper, the STEs in these pulsating stars were found in the original PDCSAP light curve, then we de-trend the light curve by sinusoidal fits. Sowicka et al. (2017) searched for transit events in pulsating stars after removing pulsation using a short cadence and found

two candidates. The search after de-trending in the pulsating stars of the long cadence data, which increases the sensitivity of detecting the transit events, remains future work.

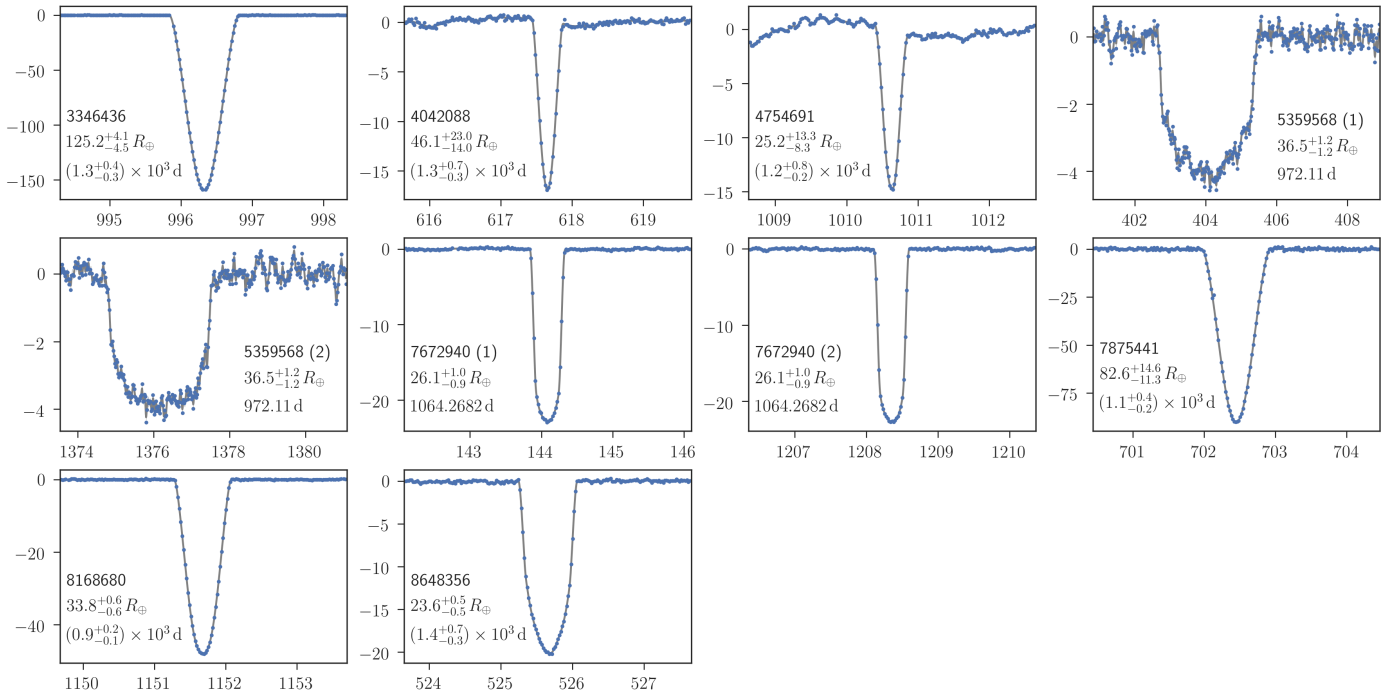


Figure 25. Same as Figure 13, but for stellar-sized candidates.

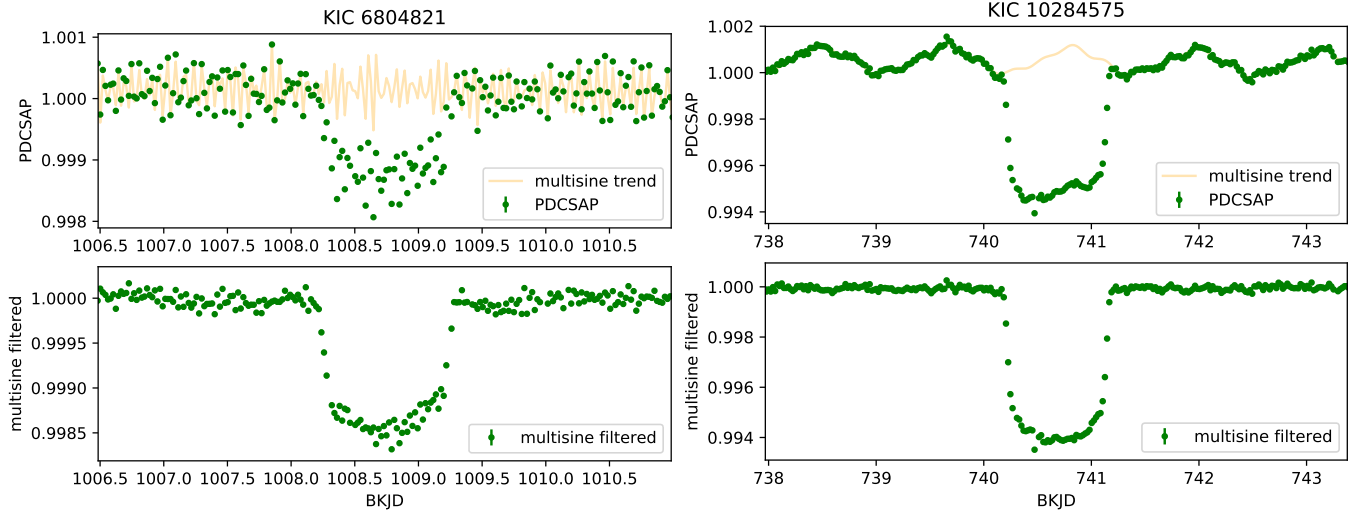


Figure 26. STEs in pulsating stars. The upper panels show the original PDCSAP light curves and the multi-sine trend for KIC 6804821 (left) and KIC 10284575 (right). The lower panels are the de-trended light curves.